

Sl. No.	Title of the paper	Name of the author/s	Department of the teacher	Name of the publisher	Year of publication	ISBN/ISSN number of the proceeding
1	Topology dependent electronic and dielectric properties of free standing alloyed ultrathin nanowires of noble metals	Arun Kumar, Ashok Kumar, P.K. Ahluwalia	Physics	Physica E	2014-15	1386-9477
2	<i>Transport properties of pristine and alloyed free standing ultrathin nanowires of noble metals.</i>	Arun Kumar, P.K. Ahluwalia	Physics	Journal of Alloys and Compounds	2014-15	0925-8388
3	Tuned electronic, optical and mechanical properties of pristine and hetero anotubes of group IV elements (C, Si and Ge)	Surjeet Kumar Chandel, Arun Kumar, Raman Sharma, P.K. Ahluwalia	Physics	Physica E	2015-16	1386-9477
4	A first principle study of encapsulated and functionalized silicon nanotube of chirality (6,6) with monoatomically thin metal wires of Ag, Au and Cu	Surjeet Kumar Chandel, Arun Kumar, P. K. Ahluwalia, Raman Sharma	Physics	Physica E	2015-16	1386-9477
5	.Electronic, Mechanical, and Dielectric Properties of Two-dimensional Atomic Layers of Noble Metals	Pooja Kapoor, Jagdish Kumar, Arun Kumar , Ashok Kumar, P. K. Ahluwalia	Physics	Journal of Electronic Materials	2017-18	0361-5235

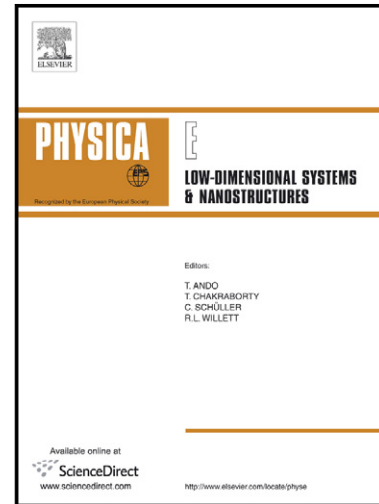
6	Alloyed monolayers of Cu, Ag, Au and Pt in hexagonal phase: A comprehensive first principles study	Pooja Kapoor, Arun Kumar , Munish Sharma, Jagdish Kumar, Ashok Kumar, P K Ahluwalia	Physics	Materials Science and Engineering B	2018-19	0921-5107
---	--	--	---------	-------------------------------------	---------	-----------

It is verified that the research papers mentioned above are included in the Scopus Index Journals list of UGC. These research papers are also attached below for the ready reference.

Author's Accepted Manuscript

Topology Dependent Electronic and Dielectric Properties of Free Standing Alloyed Ultrathin Nanowires of Noble Metals

Arun Kumar, Ashok Kumar, P.K. Ahluwalia



www.elsevier.com/locate/physica

PII: S1386-9477(14)00151-9
DOI: <http://dx.doi.org/10.1016/j.physe.2014.04.024>
Reference: PHYSE11592

To appear in: *Physica E*

Received date: 25 July 2013
Revised date: 4 April 2014
Accepted date: 28 April 2014

Cite this article as: Arun Kumar, Ashok Kumar, P.K. Ahluwalia, Topology Dependent Electronic and Dielectric Properties of Free Standing Alloyed Ultrathin Nanowires of Noble Metals, *Physica E*, <http://dx.doi.org/10.1016/j.physe.2014.04.024>

This is a PDF file of an unedited manuscript that has been accepted for publication. As a service to our customers we are providing this early version of the manuscript. The manuscript will undergo copyediting, typesetting, and review of the resulting galley proof before it is published in its final citable form. Please note that during the production process errors may be discovered which could affect the content, and all legal disclaimers that apply to the journal pertain.

Topology Dependent Electronic and Dielectric Properties of Free Standing Alloyed Ultrathin Nanowires of Noble Metals

Arun Kumar*, Ashok Kumar*, P. K. Ahluwalia*

Department of Physics, Himachal Pradesh University, Shimla, Himachal Pradesh, India 171005

Abstract

Structural, electronic and dielectric properties of free standing ultrathin alloyed nanowires of noble metals (AgAu, AgCu, AgPt, AuCu, AuPt and CuPt) in various topologies (linear, ladder and double zigzag) have been studied by using ab-initio density functional theory. Among the different topologies of alloyed ultrathin nanowires of noble metals, double zigzag (DZZ) topology has been found most stable and the linear topology the least stable. Also the binding energy of alloyed nanowires of AgAu and AuCu for all the studied topologies is found to be larger than the average binding energy of corresponding pristine nanowires, indicating a strong alloying effect for these topologies. Among electronic properties, the alloyed nanowires of different topologies containing Pt (AgPt, AuPt and AuCu) are found to be ferromagnetic in nature, a result of d charge depletion in Ag, Au and Cu sites and d charge gain at Pt sites. On the other hand, all the topologies (except ladder topology) of alloyed nanowires *viz.* AgAu, AgCu and AuCu are found to be semiconducting in nature.

The optical properties of the studied alloyed nanowires have been found to be different from their corresponding pristine nanowires due to change in the band structure on alloying. The linear topology of AgAu, AgCu and AuCu and DZZ topologies (DZZ1, DZZ2 and DZZ3) of Ag, Au, Cu, AgAu, AgCu and AuCu are semiconducting in nature with band gap lying in the infrared region. causing absorption of photons from visible spectrum leading to blackish appearance. Whereas, remaining topologies are found to be metallic in nature, with plasmon frequency lying in the energy range 0.35 eV to 1.62 eV, which is in the infrared region and hence these nanowires shall appear to be transparent to the visible region.

Keywords: Quantum wires, Electronic Structure, Dielectric Properties

PACS: 31.15.-p, 78.67.-n, 78.67.Uh

*Corresponding Author: Arun Kumar, Department of Physics, Himachal Pradesh University, Shimla-171005, India, Ph. No. +91 9418110563
Email addresses: arun242493@yahoo.com (Arun Kumar), ashok.1777@yahoo.com (Ashok Kumar), pk.ahluwalia7@yahoo.com (P. K. Ahluwalia)

1. Introduction

In the last few years, investigations on metallic nanowires [1–10] have increased largely because of various potential applications, such as their usage as interconnects in nanoelectronic systems [11], optical nanometallic communication channels [12] and biological spectroscopic enhancers [13] and as sensors [14–16]. Nanowire sensors have been used to detect many gases like O_2 , NO_2 and NH_3 , at very low concentrations [14]. They also have been used for the detection of ultraviolet (UV) light [15], as well as light sensitive biological and chemical species [16]. The usage of noble metals nanowire is well known as barcode tags [17, 18] for optical read out and lithium ion batteries [19]. These can also be used to create the materials with negative refractive index in the near infrared region [20].

The electronic, magnetic, optical and transport properties of these one dimensional (1D) systems are found to be topology dependent [1, 2]. Increased surface to volume ratio and increased density of states (DOS) of nanowires at Fermi level makes their properties different from corresponding bulk materials. The quantum confinement effects lead to formation of sub bands. As a consequence, there are more transitions near the sub band edges [21], which contribute to band edge emission.

Along with the experiments on pristine noble metal nanowires, many experiments have also been performed to study the properties of the alloyed metal nanowires [22–27]. In the first decade of 2000, point contact studies were made to study random alloys of transition metal and noble metal, namely gold and palladium [22], copper and nickel [23] and gold and platinum [25] for different concentration ratios. T. Pan *et. al.* [10] have studied the optical properties of the Au-Ag alloy nanowire coated with a radially dielectric anisotropic shell on the basis of quasi static theory. It has been observed that surface plasmon resonance (SPR) peak undergo redshift with the increasing component ratio of Au in the alloy, while increasing the component ratio of Ag in the alloy shows increase in the intensity of extinction section at SPR. Also 1D ultrathin nanowires ($Au_{25}Pt_{75}$ and $Au_{48}Pt_{52}$) have been synthesized via a wet chemistry approach at room temperature by X. Teng *et.al.* [28] and they have observed ferromagnetism in $Au_{48}Pt_{52}$ nanowire. In 2011, S. Kundu *et.al.* [29] have synthesized the alloyed nanowire of Au-Ag with diameter 4-12 nm with length few micron long which are found to be semiconducting in nature. The noble metal alloyed nanowires ($Au_{0.5}Ag_{0.5}$, $Au_{0.67}Ag_{0.33}$, $Au_{0.9}Ag_{0.1}$) with diameter below 50 nm have also been synthesized and used in the lithium ion battery [19]. Experimentally, the one dimensional alloyed nanoporous nanotubes of Au-Ag have also been fabricated by W. S. Chae *et. al.* [30] which have been found to possess distinct optical properties, such as tunable absorption in the near infrared region. These alloyed porous nanotubes of Ag-Au show higher molecular sensing activity than solid 1D wire of Au and comparable to that of porous 1D Au nanotube.

Despite many experimental investigations, there is lack of systematic theoretical study of ultrathin alloyed nanowires. However structural and electronic properties of alloyed nanowires of AgPt, AgAu and PdAu also have been studied theoretically. [31–34] In 2010 Fioravante *et. al.* [31] have studied the free standing alloyed nanowires of Ag and

Au with different topologies *viz.* ladder, zigzag and double zigzag (DZZ) using density functional theory (DFT) and reported semiconducting nature of nanowires of DZZ topology and nanowires of other topologies (ladder and zigzag) are found to be metallic in nature. It has also been observed using DFT that linear monoatomic wire of Au also get stabilized by alloying with Zn and Mg [35]. Studies have also been conducted on pristine nanowires of noble metals (Ag, Au, Cu and Pt) with linear, dimer, ladder and zigzag topologies and compared their the electronic and optical properties with the corresponding bulk [36].

In this paper we present a systematic study of structural, electronic and dielectric properties of freely suspended ultrathin alloyed nanowires of noble metal (AgAu, AgCu, AgPt, AuCu, AuPt and CuPt) with different topologies using SIESTA [37, 38] code. Here the word *alloy* has been used merely for the ease of expression and not to be taken in the strict sense. Different topologies selected for study are linear, ladder and double zigzag (DZZ) as shown in figure 1. The equal concentration of constituent atoms have been taken in the modeling of alloyed nanowires. We have taken various possible configurations of DZZ topology for alloyed nanowires *viz.* DZZ1, DZZ2 DZZ3 (corresponds to different spatial arrangement of constituent atoms) as shown in figure 1. Our calculated structural and electronic properties offer an opportunity to compare the results with other experimentally available results of alloyed nanowires. This study also equips one with a better understanding on electronic structure of free standing alloyed nanowires and allows comparison with pristine nanowires. It also gives an idea about changes in electronic properties with topology. The optical properties studied in the paper also helps to predict, how these ultrathin alloyed nanowires respond to infrared and visible spectrum of electromagnetic radiation.

2. Computational Details

We have used Troullier Martin, norm-conserving, relativistic pseudopotentials [39, 40] with valence atomic configuration $3d^{10}4s^1$, $4d^{10}5s^1$, $5d^{10}6s^1$ and $5d^96s^1$ for Cu, Ag, Au and Pt respectively. The non-linear exchange correlation correction [41] was included to improve the description of core valence interactions for Ag, Au, Cu and Pt atoms. The exchange and correlation energies were treated within the generalized gradient approximation (GGA) according to the PBEsol [42] parametrization. Throughout the geometry optimization, numerical atomic orbitals with double zeta polarization (DZP) basis sets with confinement energy of 20 *meV* have been used for all the wires considered in the study. For Brillouin zone integration, $1 \times 1 \times 30$ Monkhorst pack [43] mesh for both alloyed and pristine nanowires of different topologies have been used. The convergence tolerance for the energy was chosen as 10^{-6} eV between two consecutive self-consistent field (SCF) steps. Minimization of the energy was carried out using the standard conjugate-gradients (CG) technique. Structures were relaxed until the forces on each atom were less than 0.01 eV/Å. The mesh cut-off energy used to calculate the Hartree, exchange and correlation contribution to the total energy and Hamiltonian was chosen to be 500 Ry. The nanowires of linear and ladder topologies were modeled by taking two

atoms per unit cell, whereas nanowires of DZZ topology were modeled by taking four atoms per unit cell, with a vacuum of 30 Å along x-axis and y-axis to ensure no interaction between neighboring wires so that system represents free standing ultrathin nanowires. The stable structures (*i.e.* minimum energy configuration) for all topologies were obtained by simultaneously relaxing both lattice vectors and atomic positions in unit cell.

The dielectric properties calculations were performed by using first-order time-dependent perturbation theory [44–46] to find the dipolar transition matrix elements between occupied and unoccupied single-electron eigenstates as implemented in SIESTA code, in which the exchange and correlation effects are taken care of by plugging, the self consistent ground state DFT energies and eigenfunctions into the dipolar transition matrix elements. Thus the imaginary part of the dielectric function ϵ_2 was obtained, which was further used to calculate the real part ϵ_1 of dielectric function, reflectance (R) spectra and absorption coefficient (α) with the help of Kramers-Kronig transformations [47]. The electron energy loss spectra (EELS) has been calculated from real and imaginary parts of dielectric functions as

$$Im \left\{ -\frac{1}{\epsilon(\omega)} \right\} = \frac{\epsilon_2(\omega)}{\epsilon_1^2(\omega) + \epsilon_2^2(\omega)} \quad (1)$$

To study the dielectric properties of nanowires, electric vector was taken along the wire axis (*i.e.* z-axis). An optical mesh of $3 \times 3 \times 90$ for nanowires of different topologies has been used for dielectric calculations. A Gaussian broadening of 0.2 eV was used for the optical spectra of nanowires. Relaxation time (τ) for dielectric calculations were chosen as 0.001 Ha for pristine and alloyed nanowires of various topologies which are metallic in nature.

3. Results and Discussions

3.1. Structural Properties of Freely Suspended Ultrathin Alloyed Nanowires

The structural parameters (a, b and c as shown in figure 1) corresponding to the relaxed structures of different topologies of alloyed nanowires of noble metals are given in table 1. Our calculated structural parameters of alloyed nanowires are in good agreement with available results in literature [31, 32] as shown in table 1 in brackets. From table 2 it has been observed that, the shortest bond length in general increases as we go from linear to ladder topology and then DZZ topology and which may be attributed to the increase in the coordination number on going from linear to ladder and then DZZ topology [48]. However, in case of ladder topology of Cu, the shortest bond length decreases as we move from linear topology to ladder topology. From table 2 it has also been observed that the nearest neighbour distance of AgAu, AgCu, AuCu and CuPt in linear and ladder topologies, DZZ2 topologies of AgAu and DZZ1 and DZZ2 topology of AgCu and AuCu are found to be smaller than the average of the nearest neighbour distance of the the corresponding pristine nanowires and hence favors the alloy formation [49].

To find the stability of nanowires, we have calculated the binding energy per atom (E_b) as shown in table 1, which has been calculated as the difference between wire energy per atom of the unit cell and energy of isolated atom [50]. On careful observation of binding energy it has been found that the binding energy of alloyed nanowires of AgAu and AuCu (all the topologies) is larger than the average binding energy of corresponding pristine nanowires. While for other alloyed nanowires *viz.* AgCu, AgPt, AuPt and CuPt of different topologies, binding energy has been found to be smaller than the average of corresponding pristine nanowires. This indicates the strong alloying effect for alloyed nanowires of AgAu and AuCu for all the topologies. In general, double zigzag (DZZ) topology have been found to be most stable than other topologies (linear and ladder), while linear topology shows least stability. In three different double zigzag topologies (*i.e.* DZZ1, DZZ2 and DZZ3) of ultrathin alloyed nanowires of AgAu and CuPt, DZZ3 is most stable, while DZZ2 is least stable. Whereas for AgCu and AuCu, DZZ1 is most stable and DZZ3 is least stable, and for DZZ topologies of AgPt and AuPt, the decreasing order of stability is as follows: DZZ1>DZZ2>DZZ3.

3.2. Electronic Properties of Freely Suspended Ultrathin Alloyed Nanowires

The electronic band structure of all the considered configuration in this study have been calculated along the $\Gamma - X$ direction of the brillouin zone. The Fermi energy E_F has been set at 0 eV. Figures 2-5 represent the electronic band structure along with corresponding density of states (DOS) of freely suspended alloyed nanowires (AgAu, AgPt, AuPt and CuPt respectively) with different topologies (linear, ladder, DZZ1, DZZ2 and DZZ3). The band structure and DOS of other alloyed nanowires (AgCu and AuCu) have not been shown as these also follow the same trends as AgAu nanowires.

The electronic band structure and DOS of pristine nanowires of noble metals, with linear and ladder topologies have been studied in our earlier paper[36]. We also studied the electronic band structure and DOS of pristine nanowires of DZZ topology but not shown here. From the band structure and DOS we observed another distinguishing property of pristine and alloyed nanowires of noble metals with some topologies (linear and DZZ) showing semi conducting nature. The DZZ topology of pristine nanowires of Ag, Au and Cu are found to be semiconducting in nature with band gap of 0.72, 1.24 and 0.77 eV respectively. Also the linear and DZZ topologies of AgAu, AgCu and AuCu (alloyed nanowires) are found to be semiconducting in nature. The band gap of DZZ1 topologies of Ag, Au and AgAu and DZZ3 topology of AgAu are in agreement with the work done by Fioravante *et.al.* [31]. The semiconducting nature of these topologies are due to ground state band structure effects [31, 51]. Among the studied pristine nanowires of DZZ1 topology, we observed that all are found to be semiconducting in nature, except pristine nanowire of Pt with DZZ topology, which is metallic in nature having conductance $4G_0$, as 4 bands are crossing the Fermi energy E_F .

3.3. Magnetic Properties

The alloyed nanowires of different topologies containing Pt (AgPt, AuPt and CuPt) are found to be magnetic in nature as is clear from DOS (figures 3-5) that spin up and spin down DOS are different in magnitude, except ladder topology of CuPt (figure 5 (b)) and DZZ2 topologies of AgPt (figure 3 (d)). It is clear from the plots of DOS, shown in figures 3-5 with insets for DOS near Fermi level for AgPt, AuPt and CuPt respectively, that the major contribution for the DOS at the Fermi energy is because of Pt. In the figure 6 we have plotted the DOS for non magnetic states and ferromagnetic states (spin up and spin down) in the vicinity of Fermi level. It has been found that DOS at Fermi energy in non magnetic case for linear and DZZ1 topologies of AgPt, AuPt and CuPt and ladder topologies of AgPt and AuPt is larger than the DZZ2 topology of AuPt and CuPt and DZZ3 topology of AgPt, AuPt and CuPt, which favours ferromagnetism according to stoner criterion [52]. We have also calculated the magnetic moment in table 1 ($\mu = Q \uparrow - Q \downarrow$, where $Q \uparrow$ is the Mulliken charge population for the spin up and $Q \downarrow$ is the Mulliken charge population for the spin down charge density) [53] showing clearly the presence of ferromagnetism in some topologies of alloyed nanowires.

We have also calculated the magnetization energy (as shown in table 1), which is the difference between the energy of ferromagnetic state and non magnetic state, at equilibrium distance for various topologies which are magnetic in nature. Various topologies which are magnetic in nature follows the order for magnetization energy as: AgPt(DZZ1) > AgPt(linear) = AuPt(DZZ3) > AuPt(DZZ2) = AgPt(DZZ3) > CuPt(DZZ1) = AuPt(DZZ2) > CuPt(linear) > AuPt(linear) = CuPt(DZZ2) > CuPt(DZZ3) = AuPt(ladder) > AgPt(ladder), as given in table 1.

The DOS at the Fermi energy is affected by the increased coordination number as one goes from linear to ladder topology and then DZZ topology. The DOS at Fermi energy has been found to decrease as the coordination number increases. Therefore, magnetic moment of these nanowires is expected to follow the following order: linear > ladder > DZZ. However, on observing carefully the magnetic moment of various topologies, order followed is: linear > DZZ > ladder. The result of ladder topology is not as we had expected. This is perhaps due to the structure of ladder topology. The alloyed wires arranged in such a manner that two isolated linear chains of different metals are interacting with each other. Due to this reason ladder topology of CuPt may also be non magnetic in nature. Also among various DZZ topologies, the DZZ2 topology is found to be less magnetic than other topologies (DZZ1 and DZZ3). Also the DZZ2 topology of AgPt is found to be non magnetic in nature. On careful observation of structure of DZZ2 topology, it has been observed that two zigzag wires of two different materials are interacting with each other. Also in our earlier paper [36], we have found that the zigzag topology of noble metals (Ag, Au, Cu and Pt) are non magnetic in nature. This accounts for the non magnetic behavior of DZZ2 topology of AgPt nanowire. Also the magnetic moment of DZZ2 topology has been found to be smaller than the DZZ1 and DZZ3 topologies of AuPt and CuPt nanowires, except for DZZ3 topology of CuPt nanowire, whose magnetic moment is almost comparable to that of DZZ2 topology of CuPt

nanowire.

From above discussion, it follows that the alloyed nanowires containing Pt are ferromagnetic in nature. In other words we can say that homogeneous alloying of noble metals (Ag, Au and Cu) with Pt, favours magnetism which can be either ferromagnetism or anti-ferromagnetism both being degenerate states. This is the result of modification of electronic structure of both the metals forming alloy resulting in the d-charge depletion in the noble metals (Ag, Au and Cu) and with corresponding d-charge gain at the Pt site and hence results in an induced ferromagnetic moment. This has been supported by the partial DOS of Pt as shown in figure 3-5 (as shown in inset for the systems which are magnetic in nature). The ferromagnetism in alloyed nanowire of Au, with platinum ($Au_{48}Pt_{52}$) is also reported (experimentally) by X. Teng [28], having width less than 3nm. Hence we can say that our results are in agreement with the experimental result [28].

3.4. Ballistic Conductance of Freely Suspended Ultrathin Alloyed Nanowires

The quantum ballistic conductance of a wire under ideal situation can be determined by the number of conducting channels crossing the Fermi energy (E_F) [54]. For each channel crossing the E_F , the ballistic conductance is G_o which results into a total conductance of nG_o for n number of bands crossing the E_F . These conducting channels arise from the atomic orbitals having a significant contribution to the bands around the E_F . Therefore, on counting the number of channels crossing the E_F in the electronic band structure of the different topologies of all the studied nanowires, it is found that for all the ladder topologies the number of channels crossing Fermi energy ($N(E_F)$) are two, except alloyed nanowires of AgPt, AuPt and CuPt and pristine nanowire of Pt where $N(E_F)$ are 6, 7, 3 and 4 respectively, which corresponds to a conductance of $6G_o$, $7G_o$, $3G_o$ and $4G_o$ respectively. The $N(E_F)$ corresponding to various topologies of nanowires which are metallic in nature, is listed in table 1. The alloyed nanowires (of different topologies) containing Pt (AgPt, AuPt and CuPt) are found to be metallic in nature. From the band structure and DOS of these topologies it has been found that main contribution for the conductance of alloyed nanowires are because of 5d and 6s electrons of Pt and s electrons (valence electrons) of other atoms forming the alloy (Ag, Au and Cu) as these electrons contribute more DOS at E_F . But on the other hand in case of pristine nanowires of Ag, Au and Cu, main contribution for DOS at E_F are because of s electrons (valence electrons) and less contribution for the E_F are due to d valence electrons and hence s electrons contribute more for conductance [28]. But in case of Pt, d valence electrons contribute more for E_F and s valence electrons contribute less for E_F , hence the conductance. It has been also observed that among all the studied topologies, the topologies containing Pt (either pristine or alloyed) are metallic in nature and shows more conductance.

3.5. Dielectric Properties of Freely Suspended Ultrathin Alloyed Nanowires

In this section, we have systematically discussed the dielectric function (real (ϵ_1) and imaginary part (ϵ_2)), EELS, absorption coefficient (α) and reflectance spectra (R) for alloyed nanowires of noble metals (AgAu, AgCu, AgPt, AuCu, AuPt and CuPt) with different topologies (linear, ladder, DZZ1, DZZ2 and DZZ3) and a comparison with the corresponding pristine nanowires of noble metals. We have shown the graphs only for AgAu and AgPt (figures 7-8) as AgCu and AuCu follows the trends of AgAu and AuPt and CuPt follow the trends of AgPt. The structural peaks associated with ϵ_2 are due to the result of interband transition across E_F in the corresponding electronic band structure. It has been also observed that when ϵ_1 approaches zero, a sharp resonance peak has been observed in EELS. The plasmon frequency corresponding to these resonance peaks has been listed in table 3 for the topologies which are metallic in nature.

As discussed in previous section the alloyed nanowires are either semiconducting or metallic in nature. Therefore, first of all we discuss the optical properties of semiconducting nanowires *viz.* linear topology of AgAu, AgCu and AuCu, double zigzag topologies (DZZ1, DZZ2 and DZZ3) of Ag, Au, Cu, AgAu, AgCu and AuCu. The colour of a semiconductor, to a first approximation, is governed by the band separation energy while metals should be transparent for radiations with a frequency greater than plasmon frequency (ω_p) [55]. Band gap energy, table 1, for linear and double zigzag topologies (which are semiconducting in nature) falls in the infrared region (0.00124-1.6531 eV). Therefore, the semiconducting nanowires will absorb all photons with energy greater than the band gap separation and not those with smaller energy. Thus these nanowires will absorb photons from entire visible spectrum and hence their appearance shall look blackish [55].

The pristine nanowires of Ag, Au and Cu with double zigzag topology were found to be semiconducting with absorption edges at 0.72, 1.24 and 0.77 eV respectively. Among alloyed nanowires, the linear topology of AgAu, AgCu and AuCu are semiconducting in nature with absorption edges at 0.50, 0.03 and 0.45 eV respectively as shown in figure 7 (only for AgAu). The absorption edges corresponding to the band gap are listed in table 3. In case of linear topology of AuCu the indirect band gap is 0.04 eV but absorption edge lies at 0.45 eV. This absorption edge corresponds to the direct band gap at high symmetry point X, which is 0.45 eV.

Among the double zigzag topologies alloyed nanowires without Pt (*i.e.* AgAu, AgCu and AuCu) and corresponding pristine nanowires *viz.* Ag, Au and Cu, are found to be semiconducting in nature. In double zigzag topologies of AgCu, we have observed that absorption edge is lower than the average of absorption edge for the corresponding pristine nanowires. This is due to lowering of band gap on alloying. But in case of AgAu, the absorption edge decreases for the DZZ1 and DZZ2 and increases for the DZZ3 topology than the average of corresponding pristine nanowires. In case of AgCu the absorption edge decreases for the DZZ1 and DZZ3 topologies and slightly more than the average of corresponding alloyed nanowires. Also in case of DZZ3 topology of AgAu, the absorption edge lies very close to

the visible spectrum and hence does not absorb most of the infrared radiation.

The plasmon frequencies corresponding to nanowires which are metallic in nature, *viz.* the pristine nanowires of Ag, Au, Cu and Pt and alloyed nanowires containing Pt (AgPt, AuPt and CuPt) of linear topology, both pristine and alloyed nanowires of ladder topology and alloyed nanowires of DZZ topologies containing Pt (AgPt, AuPt, and CuPt) and pristine nanowire of Pt with DZZ topology, are listed in table 3. For these topologies the plasmon frequency lies between 0.35 eV to 1.64 eV, an infrared region (0.00124-1.6531 eV), except for ladder topology of Pt with plasmon frequency at 1.70 eV, which lies in the visible spectrum (1.6531-3.2627 eV). Thus making these transparent to the visible region (1.6531-3.2627 eV), as below the plasmon frequency these nanowires are reflecting in nature and above the plasmon frequency these nanowires are transparent. This is clear from the reflectance spectra as shown in figures 7-8. The smaller value of ω_p is due to small number density of carriers in one dimension. Thus dimensionality has a profound effect on ω_p . Also the plasmon frequency of alloyed nanowires (in ladder topology) have been found to be larger than the average of corresponding pristine nanowire, except CuPt and hence results in blue shift of reflectance edge [36]. Whereas, in case of alloyed nanowires of linear topology containing Pt (AgPt, AuPt and CuPt), the plasmon frequency is found to be smaller than the average of corresponding pristine nanowires and hence results in red shift of the reflectance edge.

4. Summary and Conclusion

In summary, first principle calculations have been performed to study the structural, electronic, magnetic and dielectric properties of free standing alloyed nanowires of noble metals (AgAu, AgCu, AgPt, AuCu, AuPt and CuPt) with different topologies (linear, ladder and DZZ).

- The results show that the bond length increases as we move from linear to ladder and then DZZ topology, which is the consequence of increase in coordination number on moving from linear to ladder and then DZZ topology.
- Also the binding energy of alloyed nanowires of AgAu and AuCu with various topologies is found to be larger than the average binding energy of corresponding pristine nanowires, indicating a strong alloying effect for these topologies.
- Among electronic properties, the alloyed nanowires of different topologies containing Pt (AgPt, AuPt and AuCu) are found to be ferromagnetic in nature, except ladder topology of CuPt and DZZ2 topology of AgPt. This ferromagnetism is the result of d-charge depletion in the noble metals (Ag, Au and Cu) and d-charge gain at the Pt site during alloy formation with the Pt. In other words we can say that the 5d electrons of Pt are responsible for magnetic behavior of these nanowires.

- The alloyed nanowires of AgAu, AgCu and AuCu (different topologies, except ladder) and pristine nanowires of Ag, Au and Cu with DZZ topology have been found to be semiconducting in nature. Whereas the topologies containing Pt (either pristine or alloyed) are metallic in nature shows more conductance as 5d valence electron are contributing more DOS at E_F .
- The linear topology of AgAu, AgCu and AuCu and DZZ topologies (DZZ1, DZZ2 and DZZ3) of Ag, Au, Cu, AgAu, AgCu and AuCu are semiconducting in nature with band gap lying in the infrared region and hence the absorption edge, which results in their appearance as blackish. Whereas, remaining topologies are found to be metallic in nature, with plasmon frequency lying in the energy range 0.35 eV to 1.62 eV, which lies in the infrared region and hence these nanowires seems to be transparent to the visible region, except ladder topology of Pt with plasmon frequency 1.70 eV (lies in the visible region (1.65-3.26 eV)) which corresponds to the red colour of the spectrum.

From the above studies we conclude that dielectric properties of nanowires have been found to change significantly with the topology and alloying, therefore, optical properties can be used as a characterization tool for nanowires. Transparent nature of noble metal nanowires suggests that they can be used as an important component for optoelectronic devices and semiconducting behavior of alloyed nanowires suggests that they can be used as a main component of electronic devices such as diodes, solar cells etc.

Acknowledgments

We gratefully acknowledge, SIESTA team for code.

- [1] B. Bhushan, *Spriger Handbook of Nanotechnology*, Volume 2, second ed., Springer, Heidelberg, 2006.
- [2] M. Springborg, Y. Dong, *Handbook of Metal Physics: Metallic Chains/Chains of Metals*, first ed., Elsevier, Amsterdam, 2007
- [3] P. Sen, M. U. Kahaly, U. V. Waghmare, *Phys Rev. B* 75 (2007) 245437-245443.
- [4] L. Cademartir, G. A. Ozin, *Adv. Mater* 21 (2009) 1013-1020.
- [5] M. S. Borg, P. Sarkar, *Phys. Rev. B* 68 (2003) 045430-045434.
- [6] J. C. Tung, G. Y. Guo, *Phys. Rev. B* 76 (2007) 094413-094424.
- [7] A. Delin, E. Tosatti, *Phys. Rev. B* 68 (2003) 144434-144441.
- [8] D. Sánchez-Portal, E. Artacho, J. Junquera, P. Ordejón, A. Garcia, J. M. Soler, *Phys. Rev. Lett.* 83 (1999) 3884-3887.
- [9] F. J. Ribeiroand, M. L. Cohen, *Phys. Rev. B* 68 (2003) 035423-035427.
- [10] T. Pan, T. Zang, H. Mao, G. Xu, *Appl Phys A* 100 (2010) 159-164.
- [11] E. Braun, Y. Eichen, U. Sivan, G. Ben-Yoseph, *Nature* 391 (1998) 775.
- [12] J. C. Weeber, A. Dereux, C. Girard, J. R. Krenn, J. P. Goudonnet, *Phys. Rev. B* 60 (1999) 9061.
- [13] F. J. García-vidal, J. M. Pitarke, J. B. Pendry, *Phys. Rev. B* 58 (1998) 6783.
- [14] Daihua Zhang, Chao Li, Xiaolei Liu, Song Han, Tao Tang, Chongwu Zhou, *Appl. Phys. Lett.* 83 (2003) 1845-1847.
- [15] H. Kind, *Adv. Materials* 14 (2002) 158-160.
- [16] Y. Cui, Q. Wei, H. Park, C. Lieber, *Science* 293 (2001) 1289-1292.
- [17] S. Nicewarner-Pena, R. G. Freeman, He L. Reis, D. Pena, I. Walton, R. Cromer, C. K. M. Natan, *Science* 294 (2001) 137-141.
- [18] H. He, N. J. Tao, *Encyclopedia of Nanoscience and Nanotechnology*, Vol X, American Scientific Publishers, North Lewis Way, 2004.
- [19] Y. J. Lee, Y. Lee, D. Oh, T. Chen, G. Ceder, A. M. Belcher, *Nano Lett.*, 10 (2010) 2433-2440.
- [20] F. Garwe, C. Rockstuhl, C. Etrich, U. Hübner, U. Bauerschäfer, F. Setzpfandt, M. Augustin, T. Pertsch, A. Tünnermann, F. Lederer, *Appl. Phys. B* 84 (2006) 139-148.
- [21] P. Singh, T. Nautial, S. Auluck, *J. Appl. Phys.* 111 (2012) 093506 (1-9).
- [22] A. Enomoto, S. Kurokawa, and A. Sakai, *Phys. Rev. B* 65 (2002) 125410.
- [23] D.J. Bakker, Y. Noat, A.I. Yanson, and J.M. van Ruitenbeek, *Phys. Rev. B* 65 (2002) 235416.
- [24] N. Agraït, A. L. Yeyatib, J. M. van Ruitenbeek, *Phys. Rep.* 377 (2003) 81-279.
- [25] A. Anaya, A.L. Korotkov, M. Bowman, J. Waddell, D. Davidovic, Nanometer-scale metallic grains connected with atomic-scale conductors, preprint (2002). <http://arXiv.org/abs/cond-mat/0210620>.
- [26] A. Enomoto, S. Kurokawa, A. Sakai, *Phys. Rev. B* 65 (2002) 125410(1-6).
- [27] J.W.T. Heemskerk, Y. Noat, D.J. Bakker, J.M. van Ruitenbeek, B.J. Thijsse, P. Klaver, A current induced transition in atomic-size contacts of metallic alloys, preprint (2002). <http://arXiv.org/abs/cond-mat/0209577>.
- [28] X. Teng, M. Feygenson, Q. Wang, J. He, W. Du, A. I. Frenkel, W. Han, M. Aronson, *Nano Lett.* 9 (2009) 3177-3184.
- [29] S. Kundu, H. Ljang, *Colloids and Surfaces A: Physicochem. Eng. Aspects* 377 (2011) 87-97
- [30] W. S. Chae, H. O. Lee, E. M. Kim, H. Yu, *Bull. Korean Chem. Soc.* 32 (2011) 1346-1348.
- [31] F. Fioravante and R. W. Nunes, *Appl. Phys. Lett.* 91 (2007) 223115 (1-3).
- [32] A. Md. Asaduzzaman, M. Springborg, *Phys. Rev. B* 72 (2005) 165422 (1-7).
- [33] M. Schreiber, S. Gemming, *Computer Physics Communications* 169 (2005) 57-59.
- [34] W. Fa, J. Dong, *J. Chem. Phys.* 128 (2008) 244703 (1-4).
- [35] W. T. Geng, K. S. Kim, *Phys. Rev. B* 67 (2003) 233403 (1-4).
- [36] A. Kumar, A. Kumar, P. K. Ahluwalia, *Physica E*, 46 (2012) 259-269.
- [37] P. Ordejón, D. A. Drabold, R. M. Martin, M. P. Grumbach, *Phys. Rev. B* 51 (1995) 1456-1476.
- [38] D. S. Daniel, P. Ordejón, E. Artacho, J. M. Soler, *Int. J. Quantum Chem.* 65 (1997) 453-461.

- [39] N. Troullier, José L. Martins, Phys. Rev. B 43 (1991) 1993-2006.
- [40] N. Troullier, J. L. Martins, Phys. Rev. B 43 (1991) 8861-8869.
- [41] S. G. Louie, S. Froyen, and M. L. Cohen, Phys. Rev. B 26 (1982) 1738.
- [42] J. P. Perdew, A. Ruzsinszky, G. I. Csonka, O. A. Vydrov, G. E. Scuseria, L. A. Constantin, X. Zhou, K. Burke, Phys. Rev. Lett. 100 (2008) 136406-136409.
- [43] J. Moreno, J. M. Soler, Phys Rev B 45 (1992) 13891-13898.
- [44] J. M. Soler, E. Artacho, J. D. Gale, A. García, J. Junquera, P. Ordejón, D. Sánchez-Portal, J. Phys. Condens. Matter 14 (2002) 2745-2779.
- [45] F. Knider, J. Hugel, A. V. Postnikov, J. Phys.: Condens. Matter 19 (2007) 196105-196116.
- [46] E. G. Maksimov, I. I. Mazin, S. N. Rashkeev, Y. A. Uspenski, J. Phys. F: Met. Phys. 18 (1988) 833-849.
- [47] J. S. Toll, Phys. Rev. 104 (1956) 1760-1770.
- [48] J. Paul, S. Narasimhan, Bulletin of Material Science 31 (2008) 569-572.
- [49] T. Rajasekharan, V. Seshubai, arXiv:0904.0697v1 (2009)
- [50] R. Gaudoin, W. M. C. Foulkes, G. Rajagopal, J. Phys.: Condens. Matter 14 (2002) 8787-8793.
- [51] R. Peierls, *Surprises in Theoretical Physics*, Princeton University Press, 1979.
- [52] J. Grotendorst, S. Blügel, D. Marx, Computational Nanoscience: Do It Yourself, NIC, FZ Jülich, 2006
- [53] www.home.uni-osnabrueck.de/apostnik/Lectures/Juelich-F4.pdf
- [54] B. K. Agrawal, V. Singh, R. Srivastava, S. Agrawal, Phys. Rev. B 74 (2006) 245405-245416.
- [55] R. Tilley, *Colour and the Optical Properties of Materials*, 2nd ed., Wiley, 2011.

Figures Caption

- Figure 1: Optimized structures of different topologies of ultrathin alloyed nanowires, (i) Linear, (ii) Ladder, (iii) DZZ1, (iv) DZZ2 and (v) DZZ3. For alloyed nanowires light (yellow coloured) and dark (brown coloured) circles represents the different atoms. Various structural parameters are represented by a, b and c.
- Figure 2: Electronic band structure and corresponding total and partial DOS for both spin up and spin down for (a) linear (b) ladder (c) DZZ1 (d) DZZ2 and (e) DZZ3 topologies of ultrathin alloyed nanowires of AgAu. The Fermi energy has been set at 0 eV. The linear, DZZ1, DZZ2 and DZZ3 topologies show semiconducting behavior with direct band gap 0.50, 0.83, 0.95 and 1.64 respectively.
- Figure 3: Electronic band structure and corresponding total and partial DOS for both spin up and spin down for (a) linear (b) ladder (c) DZZ1 (d) DZZ2 and (e) DZZ3 topologies of ultrathin alloyed nanowires of AgPt. The Fermi energy has been set at 0 eV. In inset we have shown the PDOS in the vicinity of Fermi level for the systems which are magnetic in nature. From these we conclude that Pt is contributing for magnetism with more DOS at Fermi energy for Pt than Ag.
- Figure 4: Electronic band structure and corresponding total and partial DOS for both spin up and spin down for (a) linear (b) ladder (c) DZZ1 (d) DZZ2 and (e) DZZ3 topologies of ultrathin alloyed nanowires of AuPt. The Fermi energy has been set at 0 eV. In inset we have shown the PDOS in the vicinity of Fermi level for the systems which are magnetic in nature. From these we conclude that Pt is contributing for magnetism with more DOS at Fermi energy for Pt than Au.
- Figure 5: Electronic band structure and corresponding total and partial DOS for both spin up and spin down for (a) linear (b) ladder (c) DZZ1 (d) DZZ2 and (e) DZZ3 topologies of ultrathin alloyed nanowires of CuPt. The Fermi energy has been set at 0 eV. In inset we have shown the PDOS in the vicinity of Fermi level for the systems which are magnetic in nature. From these we conclude that Pt is contributing for magnetism with more DOS at Fermi energy for Pt than Cu.
- Figure 6: DOS near Fermi energy for the alloyed nanowire of various topologies, which are magnetic in nature. Here we have shown the DOS for non magnetic and magnetic (spin up and spin down) case, near the Fermi level.
- Figure 7: Dielectric properties (Real part of dielectric function (ϵ_1), imaginary part of dielectric function (ϵ_2), EELS spectra, reflection spectra and absorption coefficient) for different topologies (linear, ladder, DZZ1, DZZ2 and DZZ3) of ultrathin alloyed nanowires of AgAu. The dielectric properties for the corresponding pristine nanowires (Ag and Au) are also shown. In the inset real part of dielectric function for linear topology of AgAu has been shown. The absorption coefficient has been taken in arbitrary units (a.u.). properties for the corresponding pristine nanowires (Ag and Pt) are also shown. The absorption coefficient has been taken in arbitrary units (a.u.). The region enclosed between dotted red lines (for reflection spectra and absorption coefficient) represents

the visible region (VR) of the electromagnetic spectrum

Figure 8: Dielectric properties (Real part of dielectric function (ϵ_1), imaginary part of dielectric function (ϵ_2), EELS spectra, reflection spectra and absorption coefficient) for different topologies (linear, ladder, DZZ1, DZZ2 and DZZ3) of ultrathin alloyed nanowires of AgPt. The dielectric properties for the corresponding pristine nanowires (Ag and Pt) are also shown. The absorption coefficient has been taken in arbitrary units (a.u.). The region enclosed between dotted red lines (for reflection spectra and absorption coefficient) represents the visible region (VR) of the electromagnetic spectrum.

Accepted manuscript

Table 1: The structural, electronic and magnetic parameters of freely suspended ultrathin alloyed nanowires of noble metals with different topologies. Here a, b and c are the nanowire parameters. Other available theoretical values are also listed for comparison taken from references [31, 32].

Topology	Property	AgAu	AgCu	AgPt	AuCu	AuPt	CuPt
Linear	a (Å)	2.625	2.47	2.59	2.45	2.51 (2.60) ^b	2.35
	E_b (eV/atom)	1.96	1.67	2.03	2.15	2.52	2.43
	$N(E_f)$	0	0	4	0	4	4
	E_g (eV)	0.50	0.03	–	0.04	–	–
	μ (μ_B /atom)	–	–	0.50	–	0.73	0.61
	ΔE_{mag} (eV)	–	–	0.12	–	0.05	0.07
Ladder	a (Å)	2.67	2.57	2.55	2.58	2.55	2.45
	b (Å)	2.65	2.49	2.66	2.45	2.59	2.40
	E_b (eV/atom)	2.31	2.05	2.92	2.54	3.34	3.30
	$N(E_f)$	2	2	6	2	7	3
	E_g (eV)	–	–	–	–	–	–
	μ (μ_B /atom)	–	–	0.06	–	0.13	–
DZZ1	a (Å)	2.89	2.77	2.75	2.82	2.77	2.51
	b (Å)	2.88	2.58	2.56	2.69	2.61	2.56
	c (Å)	2.26 (2.24) ^a	2.16	2.35	2.09	2.29	2.16
	E_b (eV/atom)	2.54 (1.77) ^a	2.32	2.98	2.86	3.41	3.41
	$N(E_f)$	0	0	3	0	2	5
	E_g (eV)	0.83 (0.93) ^a	0.67	–	0.82	–	–
DZZ2	a (Å)	2.85	2.99	2.99	2.87	3.00	2.53
	b (Å)	2.83	2.59	2.65	2.54	2.70	2.53
	c (Å)	2.29	2.10	2.27	2.12	2.22	2.20
	E_b (eV/atom)	2.52	2.31	3.11	2.81	3.49	3.46
	$N(E_f)$	0	0	3	0	4	3
	E_g (eV)	0.95	0.66	–	1.02	–	–
DZZ3	a (Å)	2.81	2.67	2.73	2.67	2.76 (2.72) ^b	2.47
	b (Å)	2.81	2.68	2.72	2.67	2.76 (2.67) ^b	2.55
	c (Å)	2.32 (2.28) ^a	2.25	2.34	2.25	2.28	2.19
	E_b (eV/atom)	2.57 (1.88) ^a	2.26	2.77	2.79	3.24	3.47
	$N(E_f)$	0	0	2	0	3	5
	E_g (eV)	1.64 (1.85) ^a	0.69	–	0.20	–	–
	μ (μ_B /atom)	–	–	0.50	–	0.50	0.32
	ΔE_{mag} (eV)	–	–	0.11	–	0.12	0.01

^a Ref. [31].

^b Ref. [32].

Table 2: The shortest bond lengths between two different atoms (in Å) of alloyed nanowires of noble metals with different topologies.

Topology	AgAu	AgCu	AgPt	AuCu	AuPt	CuPt
Linear	2.625	2.47	2.59	2.45	2.51	2.35
Ladder	2.65	2.49	2.66	2.45	2.59	2.40
DZZ1	2.67	2.51	2.63	2.48	2.61	2.45
DZZ2	2.67	2.51	2.65	2.48	2.70	2.47
DZZ3	2.70	2.55	2.64	2.49	2.62	2.51

Accepted manuscript

Table 3: Position of absorption edge for semiconducting nanowires and plasmon frequency for metallic nanowires.

Topology	Property	AgAu	AgCu	AgPt	AuCu	AuPt	CuPt
Linear	Absorption edge	0.50	0.03	–	0.45	–	–
	$\omega_p(eV)$	–	–	0.62	–	0.56	0.80
Ladder	Absorption edge	–	–	–	–	–	–
	$\omega_p(eV)$	1.17	1.06	1.44	1.14	1.52	1.35
DZZ1	Absorption edge	0.83	0.67	–	0.68	–	–
	$\omega_p(eV)$	–	–	0.46	–	0.35	0.42
DZZ2	Absorption edge	0.95	0.66	–	1.02	–	–
	$\omega_p(eV)$	–	–	0.36	–	0.65	0.25
DZZ3	Absorption edge	1.64	0.69	–	0.20	–	–
	$\omega_p(eV)$	–	–	0.62	–	0.50	0.72

^a Ref. [36].

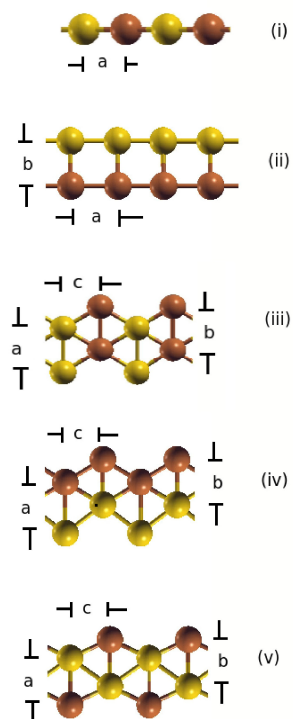


Figure 1: Optimized structures of different topologies of ultrathin alloyed nanowires, (i) Linear, (ii) Ladder, (iii) DZZ1, (iv) DZZ2 and (v) DZZ3. For alloyed nanowires light (yellow coloured) and dark (brown coloured) circles represents the different atoms. Various structural parameters are represented by a, b and c.

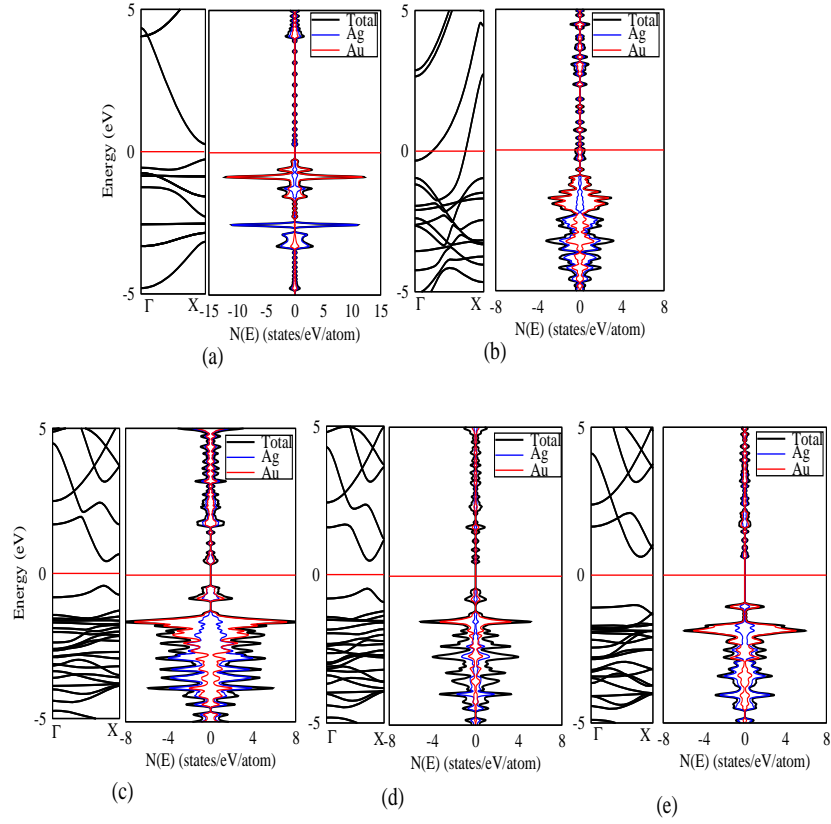


Figure 2: Electronic band structure and corresponding total and partial DOS for both spin up and spin down for (a) linear (b) ladder (c) DZZ1 (d) DZZ2 and (e) DZZ3 topologies of ultrathin alloyed nanowires of AgAu. The Fermi energy has been set at 0 eV. The linear, DZZ1, DZZ2 and DZZ3 topologies show semiconducting behavior with direct band gap 0.50, 0.83, 0.95 and 1.64 respectively.

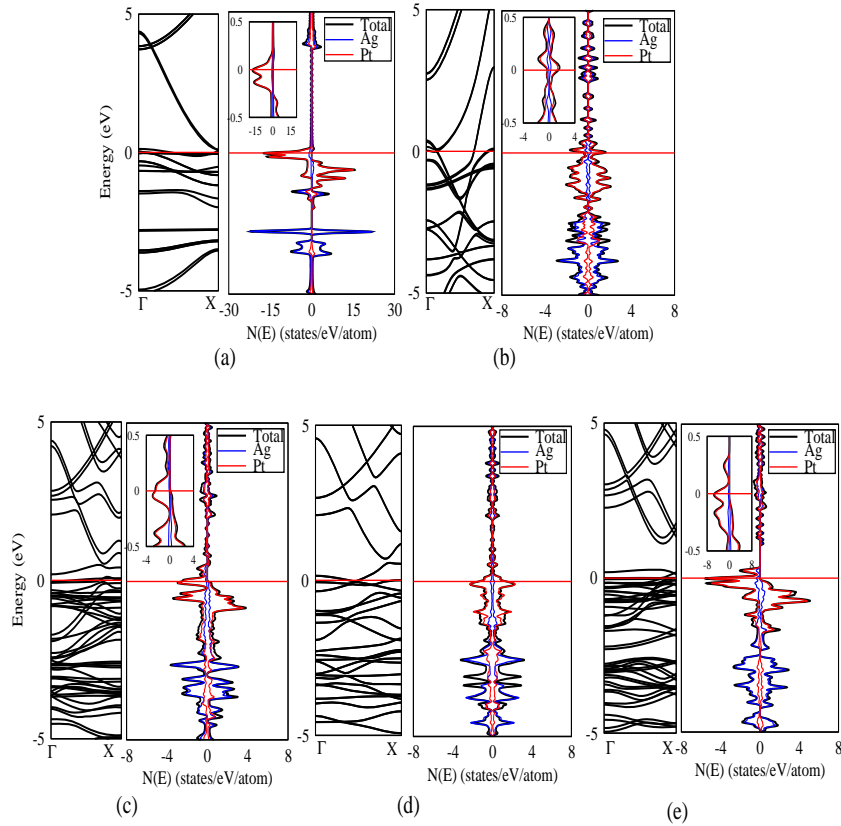


Figure 3: Electronic band structure and corresponding total and partial DOS for both spin up and spin down for (a) linear (b) ladder (c) DZZ1 (d) DZZ2 and (e) DZZ3 topologies of ultrathin alloyed nanowires of AgPt. The Fermi energy has been set at 0 eV. In inset we have shown the PDOS in the vicinity of Fermi level for the systems which are magnetic in nature. From these we conclude that Pt is contributing for magnetism with more DOS at Fermi energy for Pt than Ag.

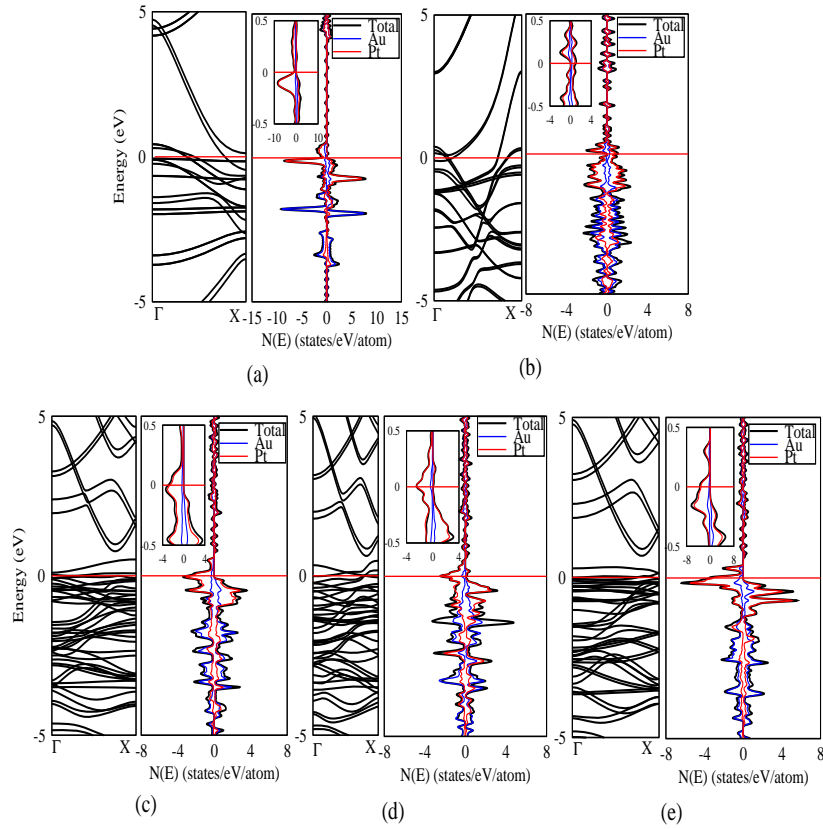


Figure 4: Electronic band structure and corresponding total and partial DOS for both spin up and spin down for (a) linear (b) ladder (c) DZZ1 (d) DZZ2 and (e) DZZ3 topologies of ultrathin alloyed nanowires of AuPt. The Fermi energy has been set at 0 eV. In inset we have shown the PDOS in the vicinity of Fermi level for the systems which are magnetic in nature. From these we conclude that Pt is contributing for magnetism with more DOS at Fermi energy for Pt than Au.

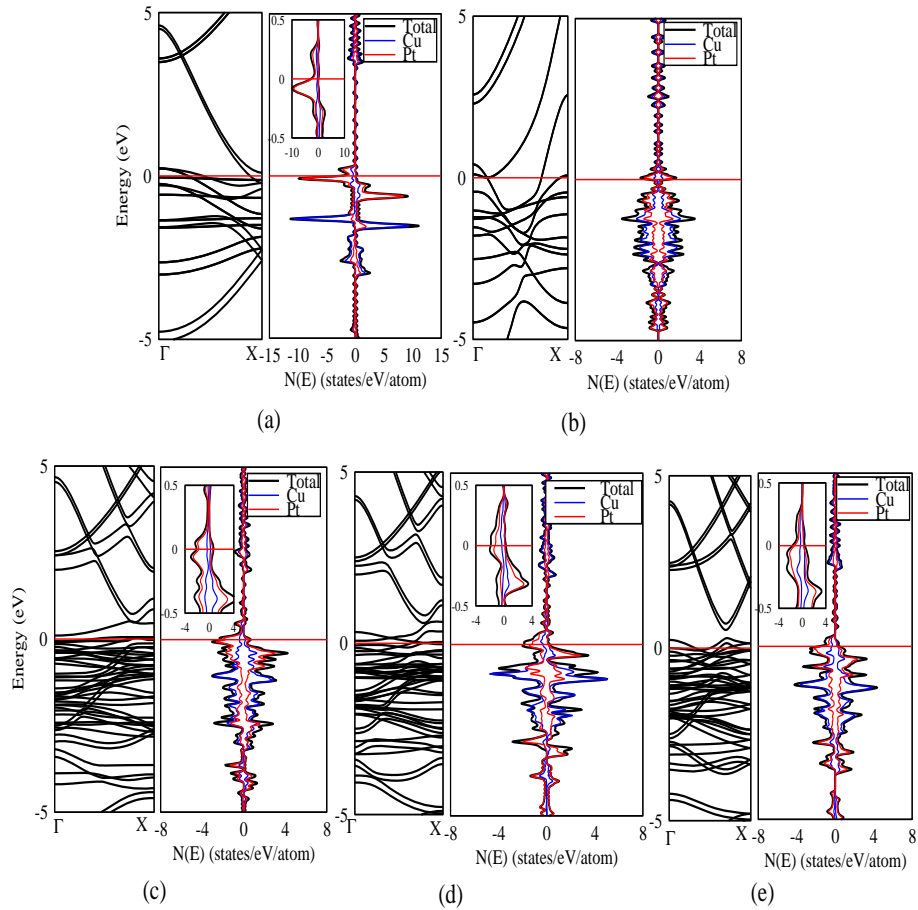


Figure 5: Electronic band structure and corresponding total and partial DOS for both spin up and spin down for (a) linear (b) ladder (c) DZZ1 (d) DZZ2 and (e) DZZ3 topologies of ultrathin alloyed nanowires of CuPt. The Fermi energy has been set at 0 eV. In inset we have shown the PDOS in the vicinity of Fermi level for the systems which are magnetic in nature. From these we conclude that Pt is contributing for magnetism with more DOS at Fermi energy for Pt than Cu.

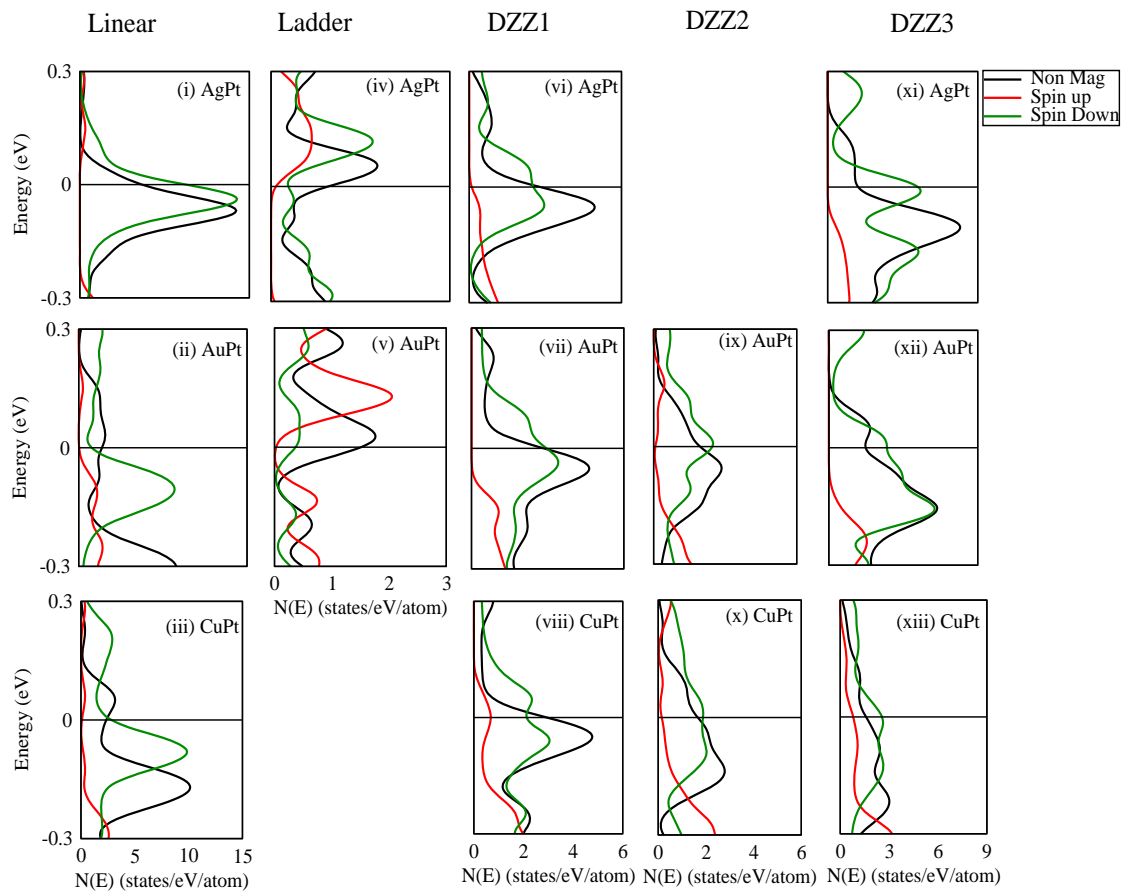


Figure 6: DOS near Fermi energy for the alloyed nanowire of various topologies, which are magnetic in nature. Here we have shown the DOS for non magnetic and magnetic (spin up and spin down) case, near the Fermi level.

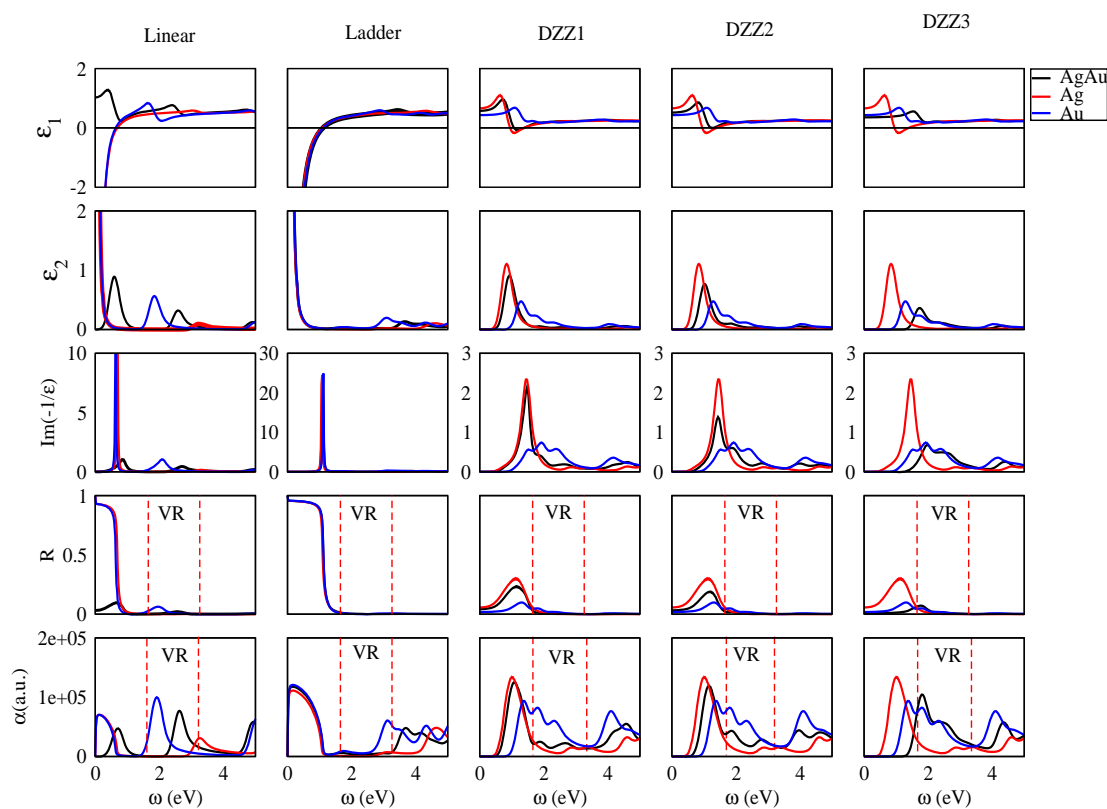


Figure 7: Dielectric properties (Real part of dielectric function (ϵ_1), imaginary part of dielectric function (ϵ_2), EELS spectra, reflection spectra and absorption coefficient) for different topologies (linear, ladder, DZZ1, DZZ2 and DZZ3) of ultrathin alloyed nanowires of AgAu. The dielectric properties for the corresponding pristine nanowires (Ag and Au) are also shown. The absorption coefficient has been taken in arbitrary units (a.u.). The region enclosed between dotted red lines (for reflection spectra and absorption coefficient) represents the visible region (VR) of the electromagnetic spectrum.

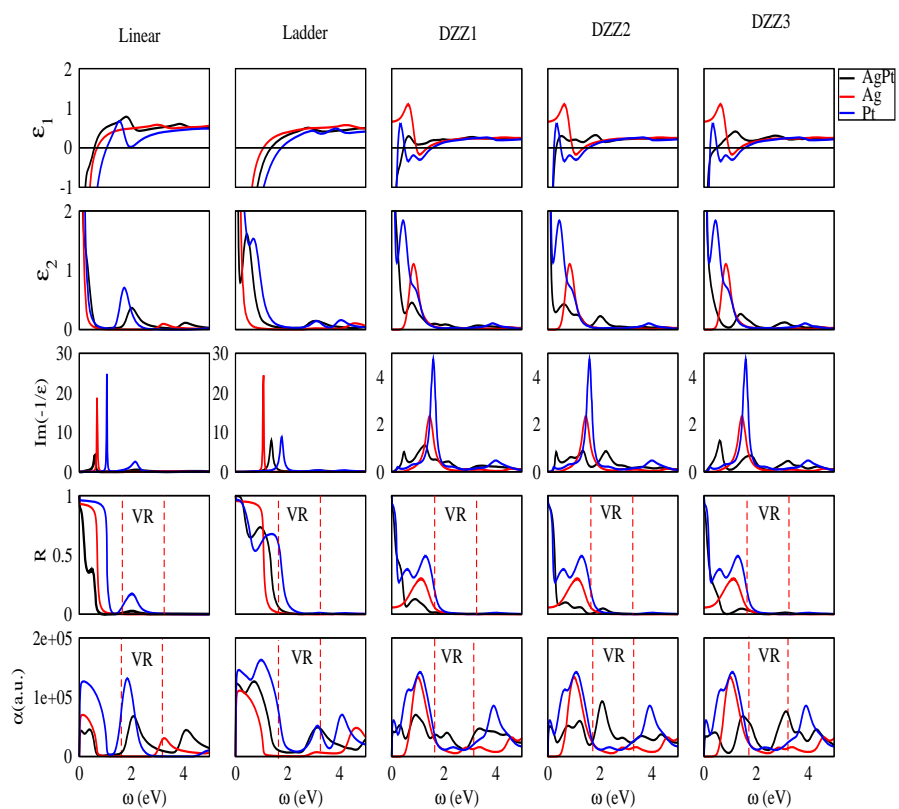


Figure 8: Dielectric properties (Real part of dielectric function (ϵ_1), imaginary part of dielectric function (ϵ_2), EELS spectra, reflection spectra and absorption coefficient) for different topologies (linear, ladder, DZZ1, DZZ2 and DZZ3) of ultrathin alloyed nanowires of AgPt. The dielectric properties for the corresponding pristine nanowires (Ag and Pt) are also shown. The absorption coefficient has been taken in arbitrary units (a.u.). The region enclosed between dotted red lines (for reflection spectra and absorption coefficient) represents the visible region (VR) of the electromagnetic spectrum



Transport properties of pristine and alloyed free standing ultrathin nanowires of noble metals



Arun Kumar*, P.K. Ahluwalia

Department of Physics, Himachal Pradesh University, Shimla 171005, Himachal Pradesh, India

ARTICLE INFO

Article history:

Received 18 December 2013
Received in revised form 29 May 2014
Accepted 29 May 2014
Available online 19 June 2014

Keywords:

Nanowires
Electronic transport
Transport processes in metals and alloys

ABSTRACT

Transport properties of free-standing ultrathin pristine and alloyed nanowires of noble metals (Ag, Au, Cu, Pt, AgAu, AgCu, AgPt, AuCu, AuPt and CuPt) with various topologies (linear, ladder and double zigzag (DZZ)) have been studied using non-equilibrium Green's function (NEGF) technique, based on density functional theory (DFT) as implemented in TranSIESTA. Compared to pristine nanowires of linear topology (Ag, Au, Cu and Pt), corresponding alloyed nanowires show diffusive/non-ballistic conductance, a result of decrease in mean free path on alloying. However, pristine and alloyed nanowires of ladder and DZZ (DZZ1, DZZ2 and DZZ3) topologies are found to show ballistic behaviour, a consequence of increase in coordination number as one moves from linear to ladder and finally DZZ topology, leading to increased mean free path and hence ballistic transport. For all the studied topologies of pristine metallic nanowires the current generally increases linearly with the V_{bias} . However, the possibility of NDC (negative differential conductance) effect of alloyed nanowires has been observed. The I - V characteristics of the AgPt nanowires with linear and DZZ1 topologies; CuPt nanowires of all the topologies; AuPt nanowires with DZZ1 and DZZ2 topologies and AgPt nanowire with DZZ1 topology are found to show tunnel diode like characteristic.

© 2014 Elsevier B.V. All rights reserved.

1. Introduction

The quantum-confined nanowires have a wide range of applications in electronics [1–10], optoelectronics [11–15], thermoelectrics [16,17], optics [3,18,19], chemo and bio-sensing [20–27], magnetic media [28–35], photocatalysis [36–38] and piezoelectronics [39–45], etc. As a result of the rapid progression of modern nanoelectronics, nanowires have begun to draw the attention of researchers in cross disciplinary areas of physics, chemistry and engineering. In nanoelectronics, nanowires can function as interconnects in the fabrication of integrated circuits [5,6], resonators [7–10], diodes [1,11–15], light emitting diodes (LED) [2], multifunctional devices [4], logic gates [23,24,46–49] using nanowire field-effect transistors [3] and single electron transistors [50]. Their small size and high electrical conductivity makes them very attractive for applications in nanoelectronics [51].

In recent years, long metallic nanowires with well defined structures and a diameter of several nanometers have been fabricated using different methods [52–55]. For example, stable gold nanobridge with 0.8–3 nm in thickness and 5–10 nm in length

has been produced by electron beam irradiation of gold (001) oriented thin film [52]. The suspended gold nanowires of 6 nm long and 0.6 nm in diameter have also been realized with novel multishell structure [55]. In 1998, Ohnishi et al. [56] using scanning tunnelling microscope and Yanson et al. [57] through mechanically break-junction experiments produced atomically thin bridge of gold atoms and found the conductance equal to $G_0 = 2e^2/h$ with interatomic distance reported as 2.6 Å [58]. The break-junction experiments have also been performed for Ag [59], Cu [60] and Pt [60] chains, with conductance nearly $1G_0$ for Cu, Ag and Au and $1.5G_0$ to $2.5G_0$ for Pt chains.

Many innovative experimental studies on one-dimensional systems [56,57,61,62], revealing their fascinating properties, have boosted related theoretical research. Depending upon the type of structure, the electronic, magnetic, optical and transport properties of these systems show interesting variations [63,69,70]. Various fabrication techniques, such as ion irradiation [52], carbon nanotube capillary growth [64–66], template-aid synthesis [67] have been introduced to synthesize much longer nanowires with well defined structures. In 2001 Kim et al. [68] have synthesized an array of ultrathin single-crystalline nanowires of silver.

However, very few studies have been made on the properties of metal alloys at the atomic scale (alloyed metal nanowires) [71–76]. In 2002 and 2003, point contact studies were made of random

* Corresponding author. Tel.: +91 9418110563.

E-mail addresses: arun242493@yahoo.com (A. Kumar), pk_ahluwalia7@yahoo.com (P.K. Ahluwalia).

alloys of a transition metal and a noble metal, namely gold and palladium [71], copper and nickel [72] and gold and platinum [74] for different concentration ratios. Lee et al. [77,78] have synthesized the alloyed nanowires of AgAu, AuPt, AuPtPd, with diameter less than 50 nm and length of few micron. These nanowires are found to be helpful in medical diagnosis, energy devices and catalysis [77–79]. In 2011 Kundu et al. [80] synthesized the AgAu alloyed nanowires, few microns long with diameters ranging from 4 to 12 nm. These nanowires are found to be semiconducting in nature. In 2006 Bettini et al. [81] experimentally realized monotonically thin alloyed nanowires of AgAu from AgAu alloy.

Besides these experimental investigations, Zhao et al. [82] have studied theoretically, the crystalline silver nanowire with four atoms per cross section and obtained three conducting channels. In 2008 Oetzel et al. [83] studied an infinite monatomic wire of Au using plane waves and conductance was found to be $1G_0$. However, there is a lack of systematic theoretical study of ultrathin alloyed freestanding nanowires.

In this paper we present a systematic study of transport properties of freely suspended ultrathin pristine and alloyed nanowires of noble metals (Ag, Au, Cu, Pt, AgAu, AgCu, AgPt, AuCu, AuPt and CuPt) in various topologies using TranSIESTA [84], a module of SIESTA code [85,86]. Different topologies selected for study are linear, ladder and double zigzag (DZZ) as shown in Fig. 1. We have chosen electrodes/leads of the same wire/topologies as that of the scattering region, since the noble metal nanowires can be used as transparent conducting electrodes [87,88]. An equal concentration of the constituent atoms has been taken in the modelling of alloyed nanowires. This study equips one with a better understanding of transport properties of alloyed nanowires, allows a comparison with the pristine nanowires and how their

conductance and I - V characteristics change with topology. The I - V characteristics of these nanowires help us to understand how 1D nanowires can be used as diodes. The understanding of the transport properties of these nanowires are important for their future applications in nanoelectronics.

2. Computational details

We have used Troullier–Martins, norm-conserving, relativistic pseudopotentials [89,90] with valence atomic configuration $3d^{10}4s^1$, $4d^{10}5s^1$, $5d^{10}6s^1$ and $5d^96s^1$ for Cu, Ag, Au and Pt respectively as reported in paper [63]. The non linear exchange correlation correction [91] was included to improve the description of core valence interactions for Ag, Au, Cu and Pt atoms. The generated pseudopotentials were tested to reproduce the results for the corresponding bulk [63]. The exchange and correlation energies were treated within the generalized gradient approximation (GGA) according to the PBEsol [92] parametrization. Throughout the geometry optimization, numerical atomic orbitals with double zeta polarization (DZP) basis sets with confinement energy of 20 MeV have been used for all the wires considered in the study. For Brillouin zone integration, $1 \times 1 \times 30$ Monkhorst–Pack cite-monkhrost mesh for both alloyed and pristine nanowires of different topologies has been chosen. We have taken 0.05 gaussian peak width and 5000 energy points in the energy window (-20 V to 10 V) for calculating DOS (density of states). The convergence tolerance for the energy was chosen as 10^{-6} eV between two consecutive self-consistent field (SCF) steps. Minimization of the energy was carried out using the standard conjugate-gradients technique. Structures were relaxed until the forces on each atom

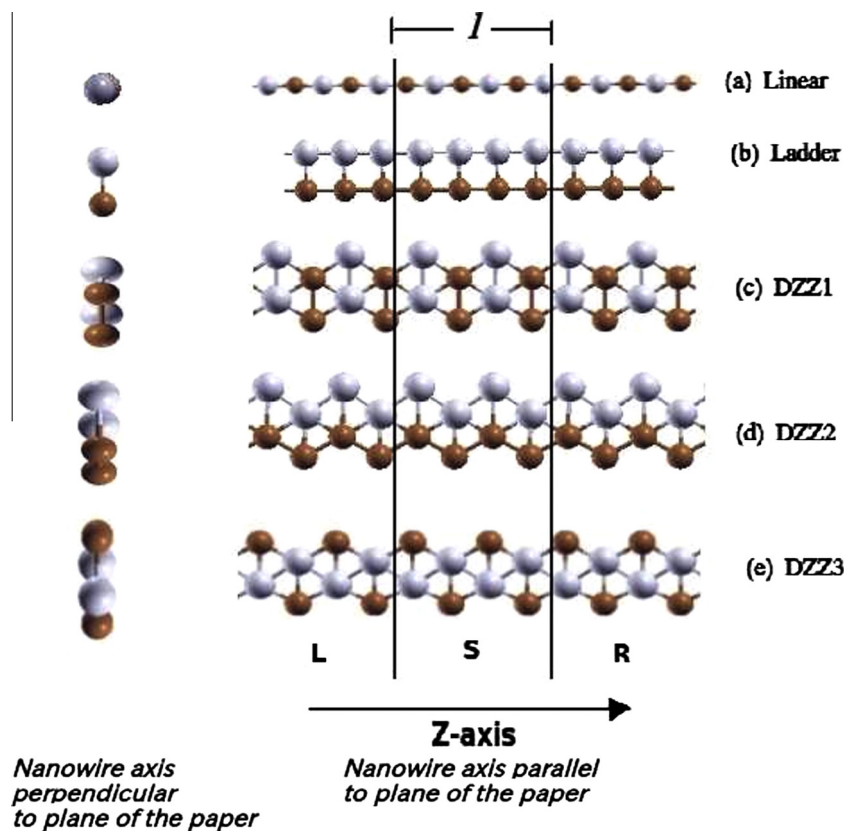


Fig. 1. Optimized structures of different topologies of ultrathin alloyed nanowires for transport calculations namely (a) linear, (b) ladder, (c) DZZ1, (d) DZZ2 and (e) DZZ3, consisting of three different regions left lead (L), scattering region (S) and right lead (R). l represents the length of scattering region. For alloyed nanowires light (gray coloured) and dark (brown coloured) circles represent different atoms.

were less than 0.01 eV/Å. The mesh cut-off energy used to calculate the Hartree, exchange and correlation contribution to the total energy and Hamiltonian was chosen to be 300 Ry. The nanowires of linear, ladder and DZZ topologies were modelled by taking 16, 20 and 24 atoms per unit cell with 6, 8 and 8 atoms taken in scattering region respectively to ensure that no interaction takes place between the atoms of left and right leads. A vacuum of 30 Å along x -axis and y -axis has been taken to ensure no interaction between neighbouring wires so that system represents free-standing ultrathin nanowires. The stable structures (*i.e.* minimum energy configuration) for all topologies were obtained by simultaneously relaxing both lattice vectors and atomic positions in unit cell.

The electronic transport properties of the optimized structures have been calculated using non-equilibrium Green's function (NEGF) technique, within Keldysh formalism, based on density functional theory (DFT) as implemented in Transiesta module with in the SIESTA package. The current through the contact region was calculated using Landauer–Buttiker formula [93–98]

$$I(V_b) = G_0 \int_{\mu_R}^{\mu_L} T(E, V_b) dE,$$

where $G_0 = 2(e^2/h)$ is the unit of quantum conductance and $T(E, V_b)$ is the transmission probability of electron incident with an energy E through the device under the potential bias V_b . The electrochemical potential difference between the left and right electrode is $eV_b = \mu_L - \mu_R$. All the calculations reported in this paper are nonspin-polarized.

3. Results and discussion

To understand the electron transport in free-standing pristine and alloyed nanowires of noble metals, electronic band structure and corresponding transmission function at zero bias *i.e.* $V_{bias} = 0$ V, PDOS and total DOS as a function of energy for the pristine and alloyed nanowires, I - V characteristic curves in between 0 and 1 V and transmission function within the bias window (-0.5 V to $+0.5$ V) at various bias voltages V_{bias} have been plotted and are shown in Figs. 2–5. In these figures we have shown plots only for Au, Pt, AgCu and AgPt nanowires with various studied topologies and the plots for Ag, Cu, AgAu, AuCu, AuPt and CuPt have been

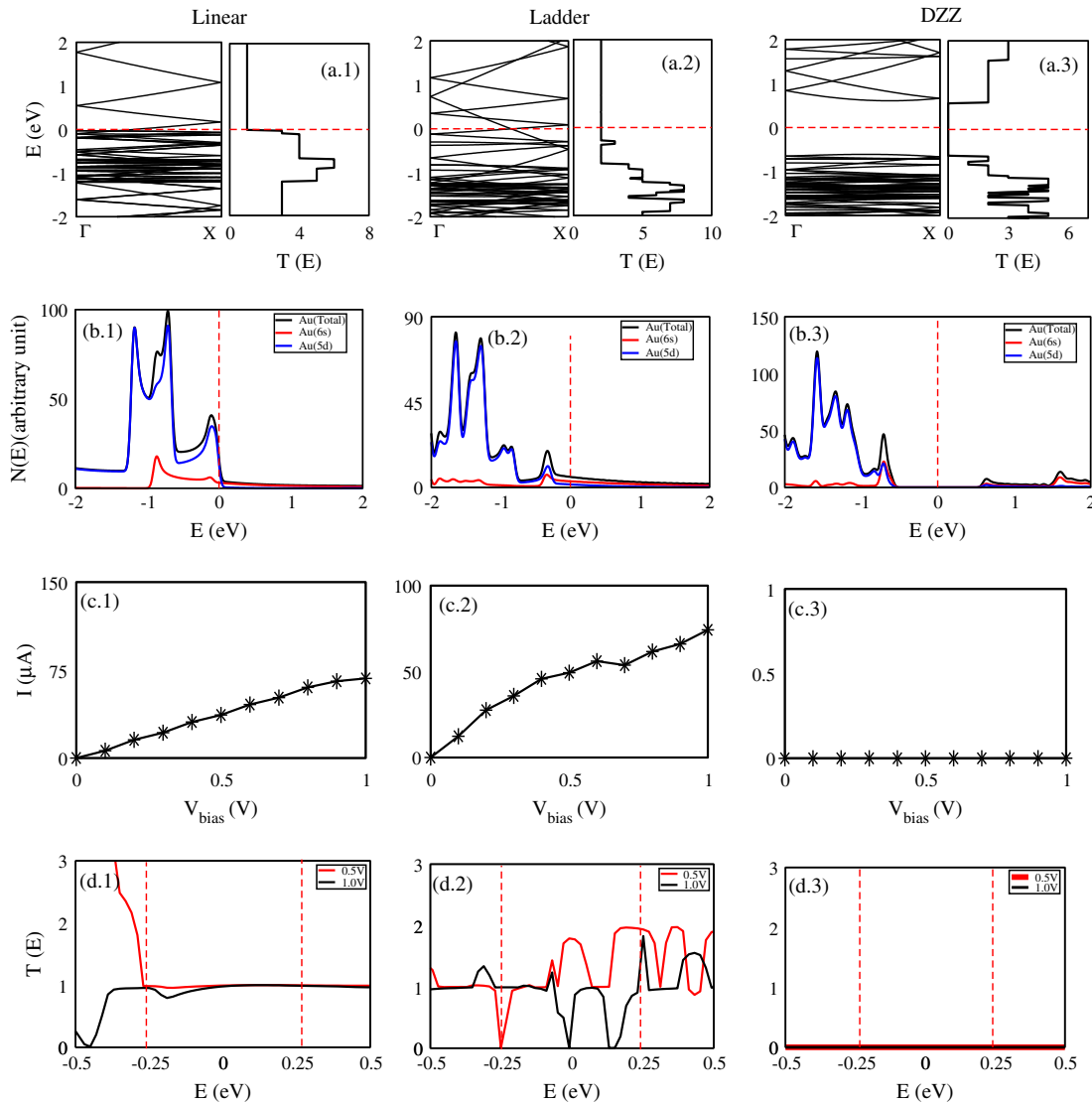


Fig. 2. (a) Electronic band structure and corresponding transmission function at zero bias voltage V_{bias} , (b) PDOS, (c) I - V characteristics and (d) transmission function $T(E)$ at different V_{bias} for free-standing pristine nanowire of Au with linear, ladder and DZZ topologies respectively. $T(E)$ plots represents the bias window from -0.25 eV to 0.25 V for $V_{bias} = 0.5$ V.

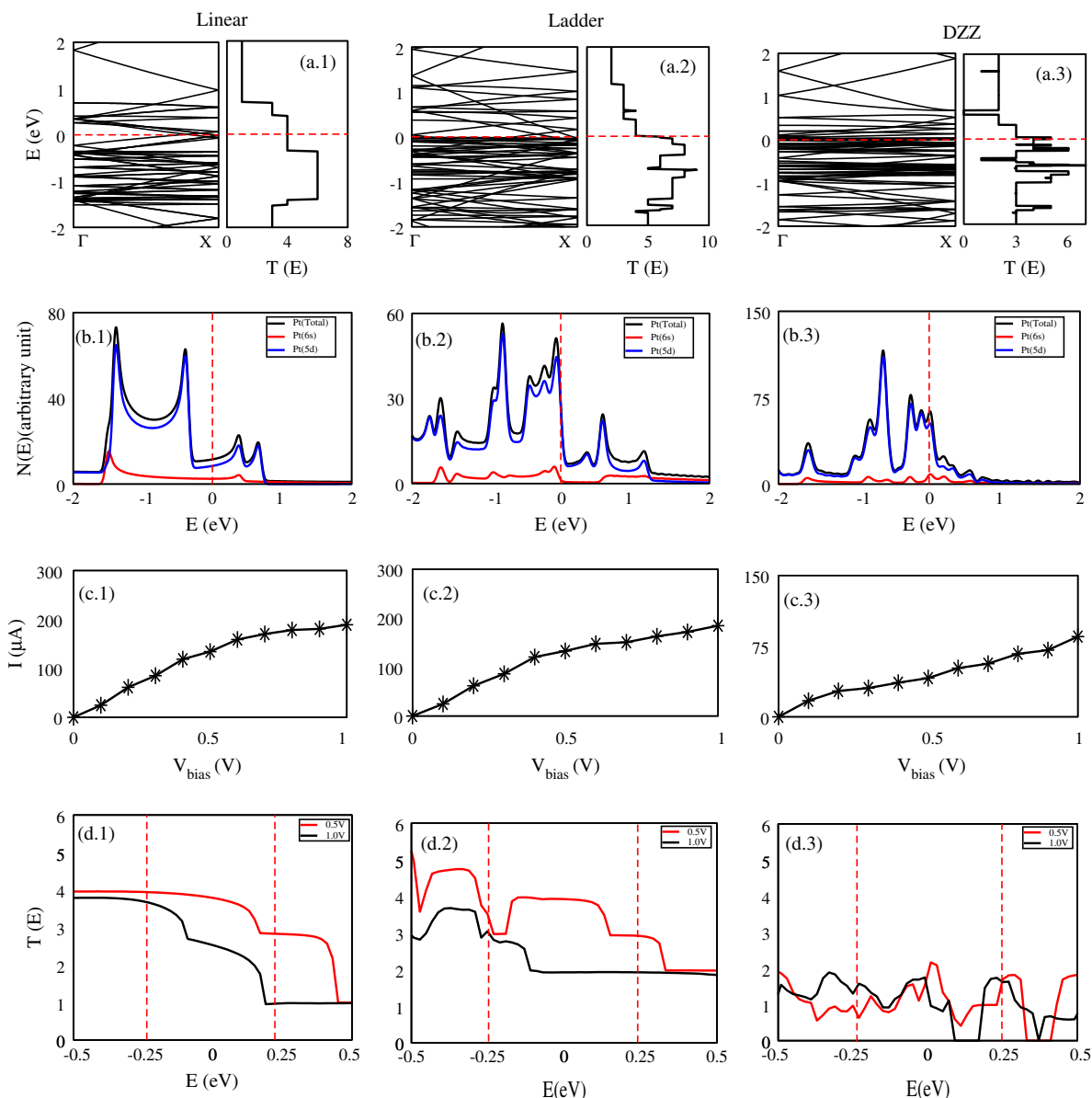


Fig. 3. Similar to Fig. 2 for free-standing pristine nanowire of Pt with linear, ladder and DZZ topologies respectively.

shown in Supplementary information (Figs. S1–S6) as these follows the same trends as that of Ag and AgPt nanowires.

3.1. Zero-bias conductance

From the electronic band structure plots (Figs. 2 and 3(a.1–a.3), 4 and 5(a.1–a.5), S1 and S2(a.1–a.3) and S3–S6(a.1–a.5)) the pristine nanowires of linear and ladder topology; alloyed nanowires of ladder topology; Pt nanowires of DZZ topology and alloyed nanowires containing Pt having linear, DZZ1, DZZ2 and DZZ3 topologies have been found to show metallic nature. The rest of the nanowires are semiconducting in nature. The number of times bands crossing the Fermi energy $N(E_F)$ corresponding to metallic nanowires have been listed in Table 1. From the plots of transmission function at zero bias as shown in Figs. 2 and 3(a.1–a.3), 4 and 5(a.1–a.5), S1 and S2(a.1–a.3) and S3–S6(a.1–a.5), the conductance G has been calculated using relation $G = G_0 T(E_F)$, where $T(E_F)$ is the value of the electron transmission probability at E_F at zero bias listed in Table 1. The energy band gaps of

nanowires with semiconducting behaviour have been listed in Table 1. The pristine nanowires of Ag, Au and Cu with DZZ topology and alloyed nanowires of AgAu, AgCu and AuCu with linear and DZZ topologies have been found to be semiconducting in nature.

3.1.1. Linear topology

In linear topology the pristine nanowires of Ag, Au and Cu have been found to show $1G_0$ conductance whereas Pt shows $4G_0$ conductance which is consistent with the number of bands crossing the Fermi energy E_F , thus suggesting the ballistic transport for these nanowires. The band structure of these nanowires have also been shown in Fig. 6(a.1–a.4) in the vicinity of Fermi energy. The coloured curves represents the bands crossing the Fermi energy E_F . From the plot of PDOS as shown in Figs. 2(b.1) and S1 and S2(b.1) for linear topology, the 5s, 5d and 3d orbitals of Ag, Au and Cu respectively are contributing for the $1G_0$ conductance, whereas in case of Pt nanowires with linear topology (Fig. 3(b.1)) 5d orbitals are contributing more DOS at E_F than the 6s orbital and hence the 5d orbitals are mainly responsible for four

conductance channels as is clear from Figs. 3(a.1) and 6(a.4). The alloyed nanowires of linear topology containing Pt viz. AgPt, AuPt and CuPt are found to be metallic in nature with conductance $0.75G_0$, $0.80G_0$ and $0.98G_0$ respectively with 3, 4, 4 times respectively bands crossing the Fermi energy (Fig. 6(a5–a.7)) as listed in Table 1. In these alloyed nanowires, 5d orbitals of Pt are contributing more DOS at the E_F and hence responsible for the number of bands crossing the Fermi energy and conductance. The fractional conductance for these alloyed nanowires of linear topology containing Pt is the result of diffusive/non-ballistic transport. The plots of transmission probability as shown in Figs. 4(a.1) and S5 and S6(a.1) for alloyed nanowires of linear topology also suggests the diffusive/non-ballistic transport.

The transport is said to be ballistic [99] if length (l) of the conducting channel is nearly equal to the mean free path (λ_e) of the electrons of the conduction channel (i.e. $l \approx \lambda_e$) and is said to be diffusive/non-ballistic if length of the conducting channel is larger than the mean free path of the electrons in the conduction channel (i.e. $l \geq \lambda_e$).

In case of alloyed nanowires of linear topology the length of the mean free path decreases with alloying [100] and the length of the

scattering channel remains almost same as listed in Table 1. Thus alloying leads to decreases in the mean free path of electrons [100] and hence accounts for diffusive/non-ballistic transport.

3.1.2. Ladder topology

In ladder topology all the studied nanowires (both pristine as well as alloyed nanowires) show ballistic transport. In comparison to linear topology shortest interatomic distance increases [63] as we move from linear to ladder topology which is a consequence of increase in coordination number and which further results in increase in mean free path. This increase in mean free path supports the ballistic transport. But channel width (W) is another parameter which affects the mean free path of the electron. The necessary condition for ballistic transport is $\lambda_e \geq W$, l [101]. Also as argued by White and Todorov [102], mean free path of the electrons in case of 1D carbon nanotubes increases with the increase in nanotube diameter. In ladder topology, the length of the conduction channel decreases whereas the width of the conduction channel gets increased, in comparison to linear topology. The decrease in channel length; increase in channel width and increase in shortest interatomic distance support the

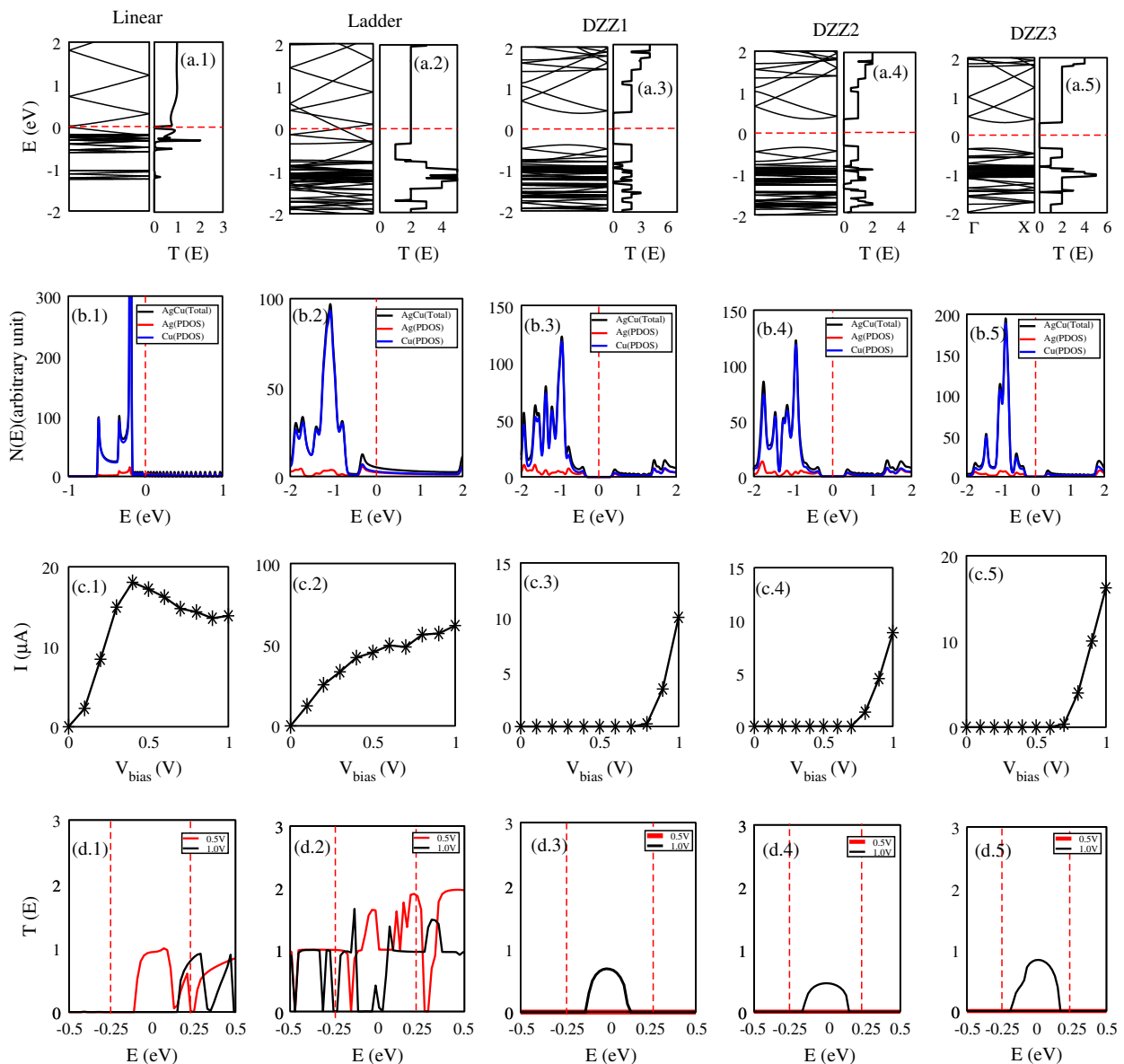


Fig. 4. Similar to Fig. 2 for free-standing alloyed nanowire of AgCu with linear, ladder and DZZ topologies respectively.

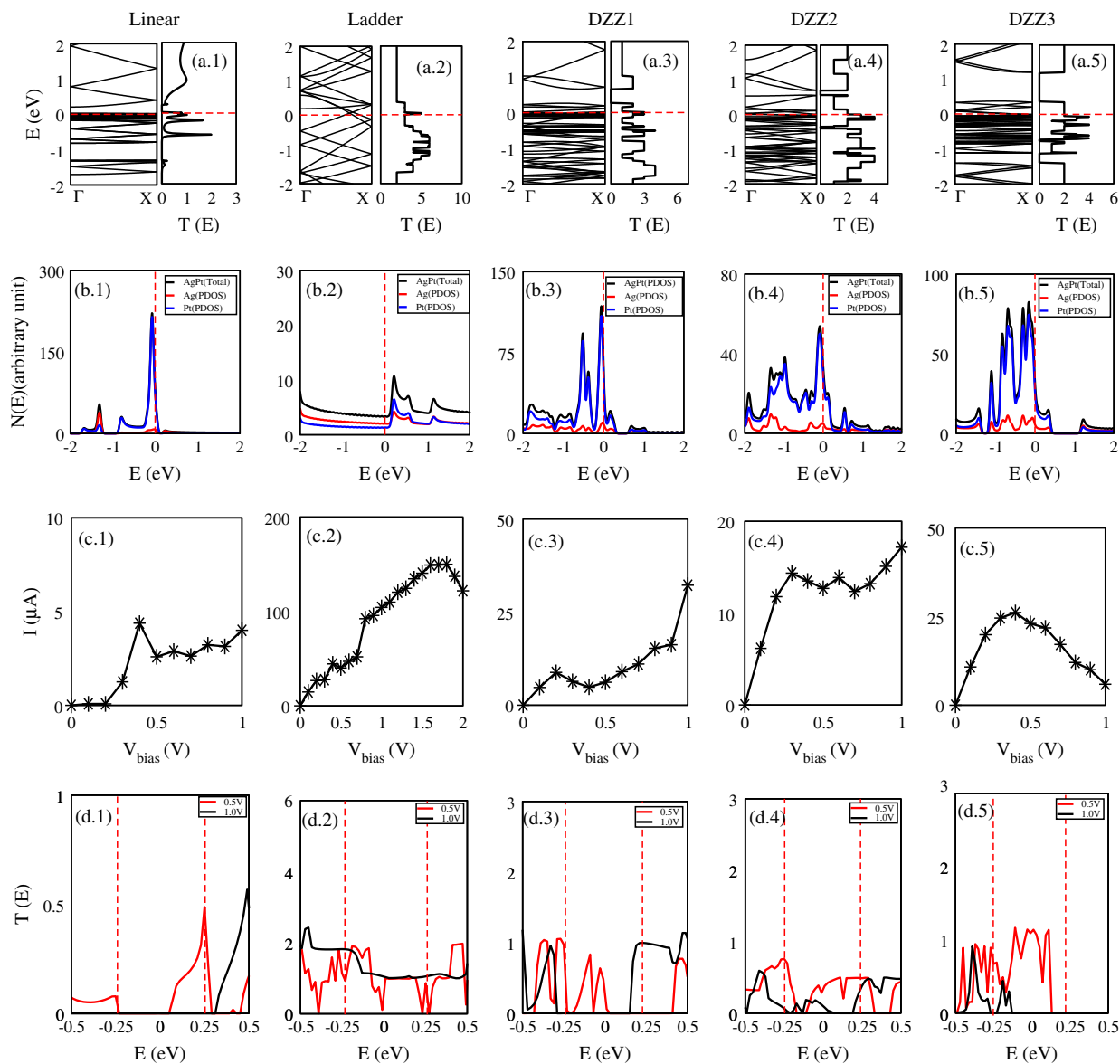


Fig. 5. Similar to Fig. 2 for free-standing alloyed nanowire of AgPt with linear, ladder and DZZ topologies respectively.

ballistic transport for ladder topology. The number of channels crossing the Fermi energy and the value of transmission probability at Fermi energy corresponding to ladder topology are shown in Table 1. From the plots of PDOS for Au, both *s* and *d* valence orbitals are contributing almost equally for DOS at E_F as is clear from Fig. 2(b.2). Similar features have been found for Ag and Cu wire (Figs. S1 and S2 of Supplementary information). Hence both are accounting for the 2 bands crossing the Fermi energy. In case of Pt nanowire both 6*s* and 5*d* (more contribution at E_F) are found to be contributing for the 4 channels as shown in Figs. 3(b.2) and 6(b.4). In case of AgCu, the *s* and *d* orbitals are contributing for the PDOS at E_F , with *s* orbital of the constituents showing maximum contribution as is clear from Fig. 4(b.2). Similar features can be seen for AgAu and AuCu (Figs. S3 and S4 in Supplementary information). On the other hand, for AgPt nanowire, the *s* and *d* orbitals are contributing for the PDOS at E_F , with *d* orbitals of Pt contributing maximum as is clear from Fig. 5(b.2). Similar

features can be found for AuPt and CuPt nanowires (Figs. S5 and S6 in Supplementary information).

3.1.3. DZZ topologies

From the plots of transmission probability, for both pristine and alloyed nanowires of DZZ topologies (DZZ1, DZZ2 and DZZ3), the ballistic behaviour has been observed. This behaviour is supported by the increase, respectively, in mean free path, shortest interatomic distance, coordination number and channel width as we move from ladder to DZZ topology. In Figs. 3(b.3) and 5(b.3–b.5) we have shown the plots of PDOS for DZZ topologies of Pt and AgPt (for AuPt and CuPt plots are shown Figs. S5 and S6(b.3–b.5) in Supplementary information) which are conducting in nature. In DZZ1 topology of Pt, both 6*s* and 5*d* orbitals are contributing for the PDOS at E_F and are collectively responsible for 5 channels *i.e.* $N(E_F)$, as clear from Figs. 3(b.3) and 6(c.1). For nanowires of AgPt, AuPt and CuPt with topologies DZZ1, DZZ2 and DZZ3 all *s* and *d*

Table 1
List of number of channels crossing the Fermi energy ($N(E_F)$), the value of transmission function at Fermi energy ($T(E_F)$) at zero V_{bias} and length of the scattering region l corresponding to various topologies of pristine and alloyed nanowires of noble metals. Other available theoretical value for linear topology of Au is also given for comparison in brackets.

Topology	Property	Ag	Au	Cu	Pt	AgAu	AgCu	AgPt	AuCu	AuPt	CuPt
Linear	$N(E_F)$	1	1	1	4	–	–	3	–	4	4
	$T(E_F)$	1	1 (1) ^a	1	4	–	–	0.44	–	0.74	0.92
	E_g (eV)	–	–	–	–	0.50	0.03	–	0.04	–	–
	l (Å)	15.90	15.60	13.80	14.40	15.75	14.85	15.52	14.70	15.07	14.10
Ladder	$N(E_F)$	2	2	2	4	2	2	3	2	5	3
	$T(E_F)$	2	2	2	4	2	2	3	2	5	3
	l (Å)	10.57	10.62	9.45	9.87	10.65	10.26	10.19	10.27	10.20	9.80
DZZ1	$N(E_F)$	–	–	–	5	–	–	3	–	2	3
	$T(E_F)$	–	–	–	5	–	–	3	–	2	3
	E_g (eV)	0.72	1.24	0.77	–	0.83	0.67	–	0.82	–	–
	l (Å)	9.22	8.95	8.04	9.06	9.06	8.43	9.39	8.36	9.15	8.64
DZZ2	$N(E_F)$	–	–	–	–	–	–	3	–	2	1
	$T(E_F)$	–	–	–	–	–	–	3	–	2	1
	E_g (eV)	–	–	–	–	0.95	0.66	–	1.02	–	–
	l (Å)	–	–	–	–	9.14	8.42	9.07	8.51	8.90	8.76
DZZ3	$N(E_F)$	–	–	–	–	–	–	2	–	1	3
	$T(E_F)$	–	–	–	–	–	–	2	–	1	3
	E_g (eV)	–	–	–	–	1.64	0.69	–	0.20	–	–
	l (Å)	–	–	–	–	9.28	9.02	9.35	9.01	9.11	8.80

^a Ref. [83].

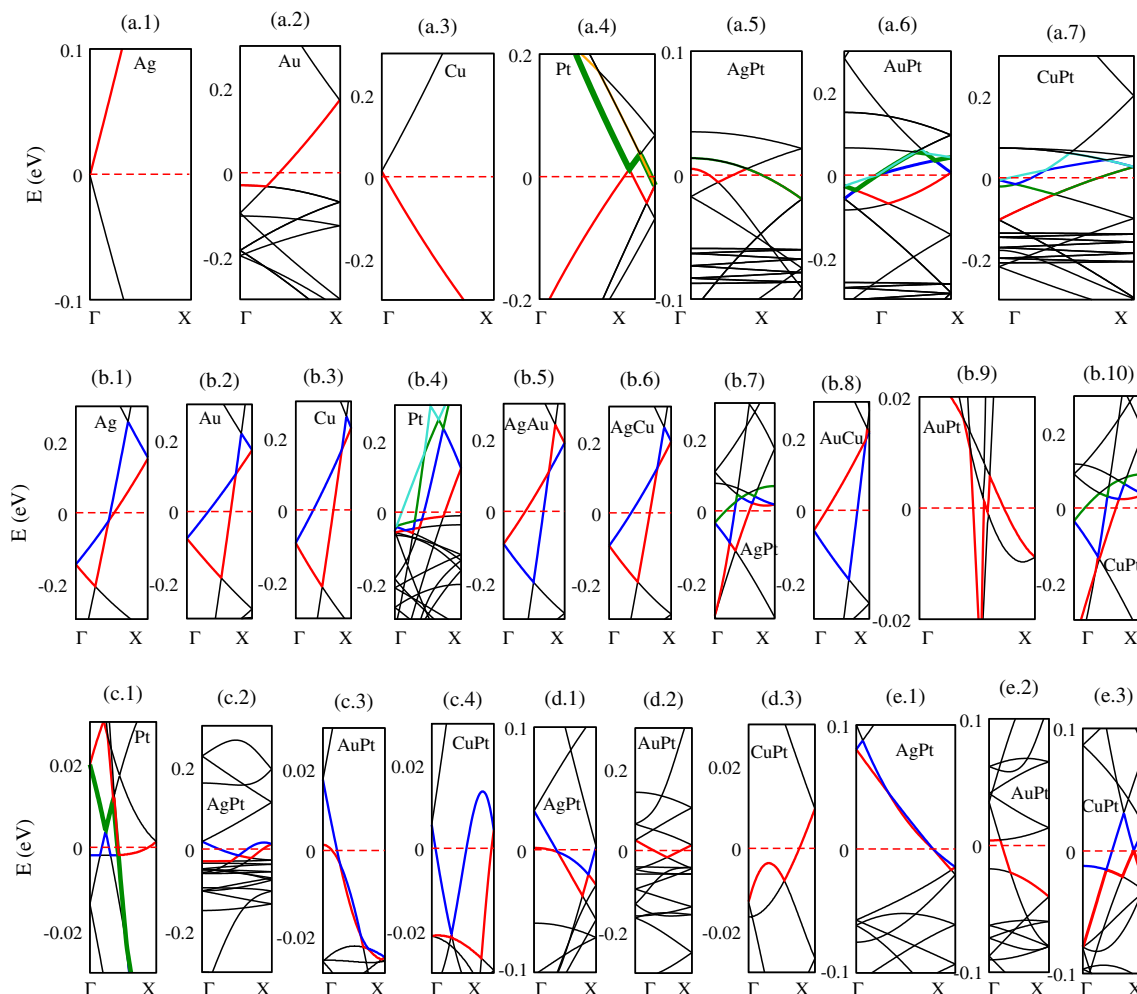


Fig. 6. Band structure of various studied topologies linear (a.1–a.7), ladder (b.1–b.10), DZZ1 (c.1–c.4), DZZ2 (d.1–d.3) and DZZ3 (e.1–e.2) of pristine and alloyed nanowires with conducting behaviour in the vicinity of Fermi energy. The Fermi energy has been set at 0 eV and the Fermi level is represented as dotted red line. The coloured curves represents the bands which are crossing the E_F . (For interpretation of the references to colour in this figure legend, the reader is referred to the web version of this article.)

orbitals of the constituents are contributing for the PDOS at E_F , but 5d orbitals of Pt show maximum contribution for DOS at E_F .

3.2. Current–voltage characteristics

The I – V characteristics of the considered topologies of pristine and alloyed nanowires of noble metals as shown in Figs. 2 and 3(c.1–c.3), 4 and 5(c.1–c.5), S1 and S2(c.1–c.3) and S3–S6(C.1–C.5) have been obtained by increasing the bias voltage, V_{bias} in the steps of 0.1 V and using the converged density of the previous state as an initial guess for the next step. The current through the scattering region has been expressed as the integration of transmission probability over the potential as given by equation in Section 2.

3.2.1. Linear topology

The I – V characteristics of all studied pristine nanowires (Figs. 2 and 3(c.1) and S1 and S2(c.1)) (only for Au and Pt nanowires have been shown) show linear variation in current with bias voltage and transmission probability with energy at different bias voltages, namely 0.5 V and 1.0 V have also been shown in Figs. 2 and 3(d.1) and S1 and S2(d.1).

The nanowires AgCu and AuCu which are semimetallic in nature have negligible energy gap of 0.03 eV and 0.04 eV respectively. AgCu nanowires show linear variation with V_{bias} upto 0.4 V for AgCu beyond this value it shows decrease in the current with the V_{bias} leading to negative differential conductance (NDC) as shown in Fig. 4(c.1). This NDC behaviour is due to decrease in $T(E)$ in the bias window as shown in Fig. 4(d.1). On the other hand, AuCu nanowire shows almost linear variation in current with V_{bias} , whereas AgAu nanowire shows I – V characteristics like forward biased PN junction diode as it is semiconducting in nature with band gap of 0.5 eV.

The nanowires of AgPt, AuPt and CuPt show almost linear variation at smaller V_{bias} , with some NDC regions at higher V_{bias} as shown in Figs. 5(c.1) (shown for the AgPt nanowires only) and S4 and S5(c.1). The NDC regions lies in the range 0.4–0.7 V for AgPt; 0.6–0.7 V for AuPt and 0.4–0.7 V for CuPt nanowires. Again, the observed NDC regions in these nanowires are due to less contribution of $T(E)$ in these bias windows at these voltages as supported from Figs. 5(d.1) and S4 and S5(d.1). Here we have shown two bias windows viz. -0.25 eV to $+0.25$ eV for 0.5 V V_{bias} and -0.5 eV to $+0.5$ eV for 1V V_{bias} . Another marked difference which has been observed is that the current in the alloyed nanowire has been found to be smaller than that in the corresponding pristine nanowire. In other words one can say that alloying decreases the conductivity of pristine nanowires which is supported by the Nordheim's Rule as cited by Pfeiler [103]. Also the alloyed nanowires containing Pt (viz. AgPt, AuPt and CuPt) and AgCu show NDC behaviour.

3.2.2. Ladder topology

In Figs. 2–5(c.2) and S1–S6(c.2), the I – V characteristics of pristine and alloyed nanowires of noble metals with ladder topology have been shown. The almost linear variation of current with the V_{bias} have been observed for the studied pristine nanowires, AgAu and AgCu nanowires. In rest of the nanowires the NDC regions have been observed. These NDC regions are due to a very small value of $T(E)$ in the bias window at the respective bias voltage.

3.2.3. DZZ topologies

The I – V characteristics for pristine and alloyed nanowires of DZZ topologies (DZZ1, DZZ2 and DZZ3) have been shown in Figs. 2–5(c.3–c.5) and S4–S6(c.3–c.4). The pristine nanowires (Ag, Au and Cu) and alloyed nanowires (AgAu, AgCu and AuCu) show almost linear variation of current with V_{bias} beyond $V_{bias} > E_g$ (where E_g

is the band gap), whereas Pt nanowire shows almost linear variation of current with V_{bias} . On the other hand, the alloyed nanowires of DZZ topologies containing Pt show multiple NDC regions. These observed NDC regions are due to small contribution for $T(E_F)$ at these bias voltages in their respective bias windows Figs. 5(d.3–d.5) (shown for the AgPt nanowires only) and S5 and S6(d.3–d.5).

From the I – V characteristics of the studied pristine and alloyed nanowires of noble metals with different topologies as discussed above, multiple NDC regions have been observed. These NDC regions are due to various reasons. The reason for these NDC regions is negligible or very small value of $T(E)$ in the vicinity of E_F at these bias voltages and is clear from the plots of $T(E)$ at different bias voltages as shown in Figs. 3–5(d.1–d.5). Another reason for the observed NDC behaviour is possibly due to non-parabolicity in the band structure of pristine and alloyed nanowires which leads to high effective masses and reduced momentum relaxation times [104–106]. This reason has been also used to explain NDC region in CNTs [107]. Another possible reason, such as inter-sub-band scattering, may also be important in 1D nanostructures and lead to NDC [106]. Another interesting point observed is that alloyed nanowires are found to show NDC regions in comparison to pristine nanowires. Thus alloying supports this behaviour. Also as the inter-sub-band energy separation in a quantum wire match the optical phonon energy, this causes enhancement of charge carriers [108], and hence support the NDC behaviour.

From the I – V characteristics of all the topologies, it is found that some of the topologies show NDC behaviour leading to tunnel diode like characteristics. The AgPt nanowire with linear and DZZ1 topologies; all the topologies of CuPt nanowire; AuPt with DZZ1 and DZZ2 topologies and AgPt nanowire with DZZ1 topology are found to show the I – V characteristics as found in tunnel diode. The observed multiple negative differential conductance (NDC) has been reported for resonant tunnelling-diode devices [109]. The multiple NDC effect has been utilized in functional electronic devices to realize multiple value logic, ultra-high speed analog-to-digital converters, frequency multipliers, and other circuit elements [109–111].

4. Summary and conclusion

In summary, the electronic transport properties of free-standing pristine and alloyed nanowires of noble metals (AgAu, AgCu, AgPt, AuCu, AuPt and CuPt) with different topologies (linear, ladder, DZZ1, DZZ2 and DZZ3) have been calculated using non-equilibrium Green's function (NEGF) technique, based on density functional theory (DFT) as implemented in TranSIESTA and following conclusions have emerged:

- The pristine nanowires of Ag, Au, Cu and Pt with linear topology show ballistic conductance, but the corresponding alloyed nanowires of linear topology show diffusive/non-ballistic conductance, which is the result of decrease in mean free path on alloying. In ladder topology all the studied nanowires are found to show ballistic conductance. The ballistic conductance is supported by the decrease in the channel length as one move from linear to ladder topology; increase in the channel width and increase in the coordination number.
- Both pristine and alloyed nanowires of DZZ topologies (DZZ1, DZZ2 and DZZ3) are found to show ballistic behaviour. This behaviour is supported by the increase in coordination number and increase in the channel width. Both of these factors support the ballistic transport.
- The value of the ballistic conductance has been found to be the largest for either pristine nanowires of Pt or alloyed nanowires containing Pt of the studied topologies. From the PDOS we have

concluded that the main contribution for the DOS at E_F is from 5d orbitals of Pt and hence Pt contributes for the large value of conductance for the studied topologies of pristine and alloyed nanowires containing Pt.

- For all the studied topologies the current generally increases linearly with the V_{bias} , but the nanowires which show NDC regions is a result of negligible or very small value of $T(E_F)$ at these bias voltages. Multiple NDC regions as stated above are due to decrease in the transmission function in the respective bias window at that V_{bias} .
- The AgPt nanowire with linear and DZZ1 topologies; CuPt nanowire of all the topologies; AuPt with DZZ1 and DZZ2 topologies and AgPt nanowire with DZZ1 topology are found to show the $I-V$ characteristic like that of a tunnel diode.

From the above study of alloyed noble metal nanowires we found that the ballistic conductance of nanowires changes significantly with topology and alloying. The conducting and semiconducting behaviour of pristine and alloyed nanowires suggests that they can be potentially used as electronic devices such as diodes and tunnel diodes.

Acknowledgment

We gratefully acknowledge SIESTA team for providing the code.

Appendix A. Supplementary material

Supplementary data associated with this article can be found, in the online version, at <http://dx.doi.org/10.1016/j.jallcom.2014.05.210>.

References

- [1] Y. Huang, X. Duan, Y. Cui, L.J. Lauhon, K.H. Kim, C.M. Lieber, *Science* 294 (2001) 1313.
- [2] X. Duan, Y. Huang, Y. Cui, J. Wang, C.M. Lieber, *Nature* 409 (2001) 66.
- [3] M.S. Gudixsen, L.J. Lauhon, J. Wang, D. Smith, C.M. Lieber, *Nature* 415 (2002) 617.
- [4] M. Mongillo, P. Spathis, G. Katsaros, P. Gentik, S. De Franceschi, *Nano Lett.* 12 (2012) 3074.
- [5] N. Kharche, S.R. Manjari, Y. Zhou, R.E. Gear, S.K. Nayak, *J. Phys. Condens. Matter* 23 (2011) 085501.
- [6] J. Song, W. Dongmok, M.C. McAlpine, R.S. Friedman, W. Yue, C.M. Lieber, *Nano Lett.* 4 (2004) 915.
- [7] S. Perisanu, P. Vincent, A. Ayari, M. Choueib, S.T. Purcell, M. Bechelany, D. Cornu, *Appl. Phys. Lett.* 90 (2007).
- [8] Z.L. Wang, G.R. Ping, P.Z. Wei, D.Z. Rong, *Adv. Eng. Mater.* 3 (2001) 657.
- [9] A. Shik, H.E. Ruda, I.G. Currie, *J. Appl. Phys.* 98 (2005) 94306.
- [10] A. Husain, J. Hone, H.W.C. Postma, X.M.H. Huang, T. Drake, M. Barbic, A. Scherer, M.L. Roukes, *Appl. Phys. Lett.* 83 (2003).
- [11] F. Qian, S. Gratecak, Y. Li, C.Y. Wen, C.M. Lieber, *Nano Lett.* 5 (2005) 2287.
- [12] K. Tomioka, J. Motohisa, S. Hara, K. Hiruma, T. Fukui, *Nano Lett.* 10 (2010) 1639.
- [13] S.K. Lee, T.H. Kim, S.Y. Lee, K.C. Choi, P. Yang, *Philos. Mag.* 87 (2007) 2105.
- [14] C. Mazuir, W.V. Schoenfeld, *J. Nanophoton.* 1 (2007) 013503.
- [15] S. Xu, C. Xu, Y. Liu, Y.F. Hu, R.S. Yang, Q. Yang, J.H. Ryou, H.J. Kim, Z. Lochner, S. Choi, R. Dupuis, Z.L. Wang, *Adv. Mater.* 22 (2010) 4749.
- [16] J.P. Heremans, C.M. Thrush, *Phys. Rev. B* 59 (1999) 12579.
- [17] J.P. Heremans, C.M. Thrush, D.T. Morelli, M.C. Wu, *Phys. Rev. Lett.* 88 (2002) 216801.
- [18] X. Duan, Y. Huang, Y. Cui, J. Wang, C.M. Lieber, *Nature* 409 (2001) 66.
- [19] M.H. Huang, S. Mao, H. Feick, H. Yan, Y. Wu, H. Kind, E. Weber, R. Russo, P. Yang, *Science* 292 (2001) 1897.
- [20] Daihua Zhang, Chao Li, Xiaolei Liu, Song Han, Tao Tang, Chongwu Zhou, *Appl. Phys. Lett.* 83 (2003) 1845.
- [21] H. Kind, *Adv. Mater.* 14 (2002) 158.
- [22] Y. Cui, Q. Wei, H. Park, C. Lieber, *Science* 293 (2001) 1289.
- [23] G.H. Yu, C.M. Lieber, *Pure Appl. Chem.* 82 (2010) 2295.
- [24] H. Yan, H.S. Choe, S.W. Nam, Y.J. Hu, S. Das, J.F. Klemic, J.C. Ellenbogen, C.M. Lieber, *Nature* 470 (2011) 240.
- [25] X.D. Wang, C.J. Summers, Z.L. Wang, *Nano Lett.* 4 (2004) 423.
- [26] J. Zhou, Y. Ding, S.Z. Deng, L. Gong, N.S. Xu, Z.L. Wang, *Adv. Mater.* 17 (2005) 2107.
- [27] A. Ponzoni, E. Comini, G. Sberveglieri, J. Zhou, S.Z. Deng, N.S. Xu, Y. Ding, Z.L. Wang, *Appl. Phys. Lett.* 88 (2006) 203101.
- [28] H. Zeng, M. Zheng, R. Skomski, D.J. Sellmyer, Y. Liu, L. Menon, S. Bandyopadhyay, *J. Appl. Phys.* 87 (2000) 4718.
- [29] A. Bala, T. Nautiyal, S. Auluck, *J. Magn. Magn. Mater.* 321 (2009) 1856.
- [30] T. Thurn-Albrecht, J. Schotter, G.A. Kästle, N. Emley, T. Shibauchi, L. Krusin-Elbaum, K. Guarini, C.T. Black, M.T. Tuominen, T.P. Russell, *Science* 290 (2000) 2126.
- [31] R. Moradian, A. Fathalian, *Nanotechnology* 17 (2006) 1835.
- [32] X. Ma, Y. Cai, N. Lun, S. Wen, *Nanotube-based Dev.* 772 (2003) 87.
- [33] E. Borowiak-Palen, E. Mendoza, A. Bachmatiuk, M.H. Rummeli, T. Gemming, J. Noguees, V. Skumryev, R.J. Kalenczuk, T. Pichler, S.R.P. Silva, *Chem. Phys. Lett.* 421 (2006) 129.
- [34] Y.-L. Mao, X.-H. Yan, Y. Xiao, *Nanotechnology* 16 (2005) 3092.
- [35] M. Weissmann, G. Garcia, M. Kiwi, R. Ramirez, *Phys. Rev. B* 70 (2004) 201401.
- [36] J. Shi, Y. Hara, C.L. Sun, M. Anderson, X.D. Wang, *Nano Lett.* 11 (2011) 3413.
- [37] S.W. Boettcher, J.M. Spurgeon, M.C. Putnam, E.L. Warren, D.B. Turner-Evans, M.D. Kelzenberg, J.R. Maiolo, H.A. Atwater, N.S. Lewis, *Science* 327 (2010) 185.
- [38] M.D. Kelzenberg, S.W. Boettcher, J.A. Petykiewicz, D.B. Turner Evans, M.C. Putnam, E.L. Warren, J.M. Spurgeon, R.M. Briggs, N.S. Lewis, H.A. Atwater, *Nat. Mater.* 9 (2010) 239.
- [39] X.D. Wang, J.H. Song, J. Liu, Z.L. Wang, *Science* 316 (2007) 102.
- [40] C.T. Huang, J.H. Song, W.F. Lee, Y. Ding, Z.Y. Gao, Y. Hao, L.J. Chen, Z.L. Wang, *J. Am. Chem. Soc.* 132 (2010) 4766.
- [41] Y. Qin, X.D. Wang, Z.L. Wang, *Nature* 451 (2008) 809.
- [42] Z.L. Wang, *Nano Today* 5 (2010) 540.
- [43] Z.L. Wang, *J. Phys. Chem. Lett.* 1 (2010) 1388.
- [44] C.T. Huang, J.H. Song, C.M. Tsai, W.F. Lee, D.H. Lien, Z.Y. Gao, Y. Hao, L.J. Chen, Z.L. Wang, *Adv. Mater.* 22 (2010) 4008.
- [45] G.C. Yi, C.R. Wang, W.I. Park, *Semicond. Sci. Technol.* 20 (2005) S22.
- [46] N.A. Kotov, J.O. Winter, I.P. Clements, E. Jan, B.P. Timko, S. Campidelli, S. Pathak, A. Mazzatenta, C.M. Lieber, M. Prato, R.V. Bellamkonda, G.A. Silva, N.W.S. Kam, F. Patolsky, L. Ballerini, *Adv. Mater.* 21 (2009) 3970.
- [47] X.C. Jiang, J.S. Hu, L.A. Fitzgerald, J.C. Biffinger, P. Xie, B.R. Ringeisen, C.M. Lieber, *Proc. Natl. Acad. Sci. USA* 107 (2010) 16806.
- [48] B.Z. Tian, T. Cohen-Karni, Q.A. Qing, X.J. Duan, P. Xie, C.M. Lieber, *Science* 329 (2010) 830.
- [49] S. Nam, X.C. Jiang, Q.H. Xiong, D. Ham, C.M. Lieber, *Proc. Natl. Acad. Sci. USA* 106 (2009) 21035.
- [50] C. Thelander, T. Martensson, M.T. Bjork, B.J. Ohlsson, M.W. Larsson, L.R. Wallenberg, L. Samuelson, *Appl. Phys. Lett.* 83 (2003) 2052.
- [51] Y. Cui, C. Lieber, *Science* 291 (2001) 851.
- [52] Y. Kondo, K. Takayanagi, *Phys. Rev. Lett.* 79 (1997) 3455.
- [53] I. Lisiecki et al., *Phys. Rev. B* 61 (2000) 4968.
- [54] W.S. Yun et al., *J. Vac. Sci. Technol. A* 18 (2000) 1329.
- [55] Y. Kondo, K. Takayanagi, *Science* 289 (2000) 606.
- [56] H. Ohnishi, Y. Kondo, K. Takayanagi, *Nature* 395 (1998) 780.
- [57] A.I. Yanson, G.R. Bollinger, H.E. van den Brom, N. Agrait, J.M. van Ruitenbeek, *Nature* 395 (1998) 783.
- [58] G. Untiedt, A.I. Yanson, R. Grande, G. Rubio-Bollinger, N. Agrait, S. Vieira, J.M. van Ruitenbeek, *Phys. Rev. B* 66 (2002) 085418.
- [59] N. Agrait, A.L. Yeyati, J.M. van Ruitenbeek, *Phys. Rep.* 377 (2003) 81.
- [60] R.H.M. Smit, C. Untiedt, A.I. Yanson, J.M. van Ruitenbeek, *Phys. Rev. Lett.* 87 (2001) 266102.
- [61] V. Rodrigues, T. Fuhrer, D. Ugarte, *Phys. Rev. Lett.* 85 (2000) 4124.
- [62] P. Gambardella, A. Dallmeyer, K. Maiti, M.C. Malagoli, W. Eberhardt, K. Kern, C. Carbone, *Nature (London)* 416 (2002) 301.
- [63] A. Kumar, A. Kumar, P.K. Ahluwalia, *Physica E* 46 (2012) 259.
- [64] J. Sloan, D.M. Wright, H.G. Woo, S. Bailey, G. Brown, A.P.E. York, K.S. Coleman, J.L. Hutchison, M.L. Green, *Chem. Commun.* 8 (1999) 699.
- [65] C.H. Kiang, J.S. Choi, T.T. Tran, A.D. Bacher, *J. Phys. Chem. B* 103 (1999) 7449.
- [66] A. Govindaraj, B.C. Satishkumar, M. Nath, C.N.R. Rao, *Chem. Mater.* 12 (2000) 202.
- [67] T. David, D. Buttard, M.D. Hertog, P. Gentile, T. Baron, P. ferret, J.L. Rouvière, *Superlattices Microstruct.* 44 (2008) 354.
- [68] B.H. Hong, S.C. Bae, Chi-Wan Lee, S. Jeong, K.S. Kim, *Science* 294 (2001) 348.
- [69] P. Sen, S. Ciraci, A. Buldum, I.P. Batra, *Phys. Rev. B* 64 (2001) 195420.
- [70] A. Kumar, P.K. Ahluwalia, *J. Alloys Comp.* 587 (2014) 459.
- [71] A. Enomoto, S. Kurokawa, A. Sakai, *Phys. Rev. B* 65 (2002) 125410.
- [72] D.J. Bakker, Y. Noat, A.I. Yanson, J.M. van Ruitenbeek, *Phys. Rev. B* 65 (2002) 235416.
- [73] N. Agrait, A.L. Yeyati, J.M. van Ruitenbeek, *Phys. Rep.* 377 (2003) 81.
- [74] A. Anaya, A.L. Korotkov, M. Bowman, J. Waddell, D. Davidovic, *Nanometer-scale metallic grains connected with atomic-scale conductors*, 2002. <<http://arXiv.org/abs/cond-mat/0210620>> (in press).
- [75] A. Enomoto, S. Kurokawa, A. Sakai, *Phys. Rev. B* 65 (2002) 125410.
- [76] J.W.T. Heemskerk, Y. Noat, D.J. Bakker, J.M. van Ruitenbeek, B.J. Thijsse, P. Klaver, *A current induced transition in atomic-size contacts of metallic alloys*, 2002. <<http://arXiv.org/abs/cond-mat/0209577>> (in press).
- [77] Y. Lee, *Fabrication of 1-Dimensional Nanowires from Genetically Modified M13 Phage through Surfactant-mediated Hybridization and the Application in Medical Diagnosis, Energy Devices and Catalysis*, Ph.D. Thesis, B.S. & M.S. Seoul National University, Korea, 2010.
- [78] Y.J. Lee, Y. Lee, D. Oh, T. Chen, G. Ceder, A.M. Belcher, *Nano Lett.* 10 (2010) 2433.

- [79] Y. Lee, J. Kim, D.S. Yun, Y. S Nam, Y. Shao-Horn, A.M. Belcher, *Energy Environ. Sci.* 5 (2012) 8328.
- [80] S. Kundu, D. Huitink, K. Wang, S. Lau, H. Liang, *Colloids Surf. A: Physicochem. Eng. Aspects* 377 (2011) 87.
- [81] J. Bettini, F. Sato, P.Z. Coura, S.O. Dantas, D.S. Galvao, D. Ugarte, *Nat. Nanotechnol.* 1 (2006) 182.
- [82] J. Zhao, C. Buia, J. Han, J.P. Lu, *Nanotechnology* 14 (2003) 501.
- [83] B. Oetzel, M. Preuss, F. Ortman, K. Hannewald, F. Bechstedt, *Phys. Stat. Sol. B* 245 (2008) 854.
- [84] M. Brandbyge, J.L. Mozos, P. Ordejón, J. Taylor, K. Stokbro, *Phys. Rev. B* 65 (2002) 165401.
- [85] P. Ordejón, E. Artacho, J.M. Soler, *Phys. Rev. B* 53 (1996) R10441.
- [86] J.M. Soler, E. Artacho, J.D. Gale, A. Garcia, J. Junquera, P. Ordejón, D. Sánchez-Portal, *J. Phys.: Condens. Matter* 14 (2002) 2745.
- [87] H. Guo, N. Lin, Y. Chen, Z. Wang, Q. Xie, T. Zheng, N. Gao, S. Li, J. Kang, D. Cai, D. Peng, *Sci. Rep.* 3 (2013) 2323.
- [88] J. Groep, P. Spinelli, A. Polman, *Nano Lett.* 12 (2012) 3138.
- [89] N. Troullier, J.L. Martins, *Phys. Rev. B* 43 (1991) 1993.
- [90] N. Troullier, J.L. Martins, *Phys. Rev. B* 43 (1991) 8861.
- [91] S.G. Louie, S. Froyen, M.L. Cohen, *Phys. Rev. B* 26 (1982) 1738.
- [92] J.P. Perdew, A. Ruzsinszky, G.I. Csonka, O.A. Vydrov, G.E. Scuseria, L.A. Constantin, X. Zhou, K. Burke, *Phys. Rev. Lett.* 100 (2008) 136406.
- [93] R. Landauer, *Philos. Mag.* 21 (1970) 863.
- [94] M. Büttiker, Y. Imry, R. Landauer, S. Pinhas, *Phys. Rev. B* 31 (1985) 6207.
- [95] M. Büttiker, *Phys. Rev. Lett.* 57 (1986) 1761.
- [96] K. Stokbro, J. Taylor, M. Brandbyge, P. Ordejón, *Ann. N.Y. Acad. Sci.* 1006 (2003) 212.
- [97] S. Datta, *Electronic Transport in Mesoscopic Systems*, Cambridge Univ. Press, 1997.
- [98] S. Datta, *Quantum Transport: Atom to Transistor*, second ed., Cambridge University Press, 2005.
- [99] G.W. Hanson, *Fundamentals of Nanoelectronics*, first ed., Pearson Education, 2009, pp. 328–341 (Chapter 10).
- [100] M. Krawczyk, L. Zommer, J.W. Sobczak, A. Jablonski, *Appl. Surf. Sci.* 235 (2004) 15.
- [101] H. Heinrich, G. Bauer, F. Kuchar, *Springer series in solid-state sciences, Physics and Technology of Submicron Structures*, vol. 83, Springer-Verlag, Berlin, Heidelberg, 1988, pp. 230–240.
- [102] C.T. White, T.N. Todorov, *Nature* 393 (1998) 240.
- [103] W. Pfeiler, *Alloy Physics: A Comprehensive Reference*, Wiley-VCH Verlag, Weinheim, 2007, pp. 913.
- [104] Z. Dobrovolskis, K. Grigoras, A. Krotkus, *Appl. Phys. A* 48 (1989) 245.
- [105] B.R. Nag, *Electron Transport in Compound Semiconductors*, Springer, Berlin, 1980.
- [106] S.A. Dayeh, *Semicond. Sci. Technol.* 24 (2010) 024004.
- [107] V. Perebeinos, J. Tersoff, P. Avouris, *Nano Lett.* 6 (2006) 205.
- [108] D. Jovanovic, J.P. Leburton, K. Ismail, *Semicond. Sci. Technol.* 9 (1994) 882.
- [109] Y. Bekenstein, K. Vinokurov, T.J. Levi, E. Rabani, U. Banin, O. Millo, *Phys. Rev. B* 86 (2012) 085431.
- [110] S. Sen, F. Capasso, A.Y. Cho, D. Sivco, *IEEE Trans. Electron Dev.* 34 (1987) 2185.
- [111] S. Sen, F. Capasso, A.Y. Cho, D.L. Sivco, *IEEE Electron Dev. Lett.* 9 (1988) 533.



Tuned electronic, optical and mechanical properties of pristine and hetero nanotubes of group IV elements (C, Si and Ge)



Surjeet Kumar Chandel^{a,*}, Arun Kumar^b, Raman Sharma^a, P.K. Ahluwalia^a

^a Department of Physics, Himachal Pradesh University, Shimla, Himachal Pradesh 171005, India

^b Department of Physics, Government College Banjar, District Kullu, Himachal Pradesh 175123, India

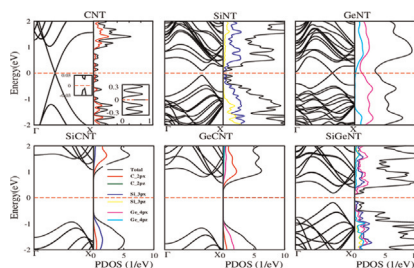
HIGHLIGHTS

- We studied Electronic and Optical properties of Pristine and Hetero Nanotubes.
- The cohesive energy per atom is more for CNT and SiCNT in our study.
- Only GeNT is found to be metallic in nature with a conductance of $2G_0$.
- Hetero nanotubes have wide band gap spectrum, hence suitable for electronic devices.
- The decreasing order of tensile strength is $CNT > SiCNT > GeCNT > SiNT > GeNT > SiGeNT$.

GRAPHICAL ABSTRACT

We present electronic band structure of pristine and hetero systems under study.

Electronic band structure and corresponding total and partial DOS for pristine and heteronanotubes. In the inset we have shown the band structure and density of states for CNT in the vicinity of Fermi energy which shows semi-metallic behaviour.



ARTICLE INFO

Article history:

Received 7 April 2015

Accepted 4 May 2015

Available online 16 May 2015

Keywords:

Pristine nanotubes

Heteronanotubes

Electronic

Optical and mechanical properties

ABSTRACT

Density functional theory has been used to investigate the structural, electronic, optical and mechanical properties of pristine nanotubes of carbon, silicon, germanium and their hetero nanotubes having armchair conformation with chirality (6,6). In the pristine nanotubes it is found that the cohesive energy per atom is more for CNT as compared to other nanotubes under investigation. However, in hetero systems under study its value is highest for SiCNT system and least for GeCNT. GeNT and SiGeNT have been observed to be more puckered in comparison to other systems. All the pristine and hetero-nanotubes in our study are found to be semiconducting in nature, except GeNT, which is found to be metallic in nature with a conductance of $2G_0$, indicating GeNT to be an ideal material for ballistic transport. Three different types of hetero nanotubes have wide band gap spectrum which opens up an arena for band gap selective engineered devices. The band gap for SiCNT and GeCNT lie in the visible region, while the band gap for other systems lie in the infrared region. The tuning of electronic band structure by means of compression, tensile strain and external electric field indicates that the band gap can be altered considerably. There is a band gap closure under both compression and expansion at a certain value in all the cases except SiCNT, revealing that its band gap can be varied considerably. The decreasing order of tensile strength is $CNT > SiCNT > GeCNT > SiNT > GeNT > SiGeNT$. The effective mass of holes decreases for pristine systems on the application of compression. Under no strain the effective mass of electrons is generally found to be larger than holes in hetero systems, while it is reverse in

* Corresponding author.

E-mail addresses: skchandel2@yahoo.in (S.K. Chandel), arun242493@yahoo.com (A. Kumar), bramans70@yahoo.co.in (R. Sharma), pk_ahluwalia7@yahoo.com (P.K. Ahluwalia).

pristine systems. In case of unstrained systems, we generally observed that the more the effective mass of electron, the more is the band gap in the corresponding system.

© 2015 Elsevier B.V. All rights reserved.

1. Introduction

The discovery and the consequent scientific and technological applications of carbon nanotubes have initiated an increasing interest in the field of novel low dimensional materials [1]. Besides carbon nanotubes there are other materials belonging to the same group such as Si and Ge whose nanotubes are also strong contenders for technological applications. Their low dimensionality and the quantum confinement effect can result in fascinating electronic and optical properties [2–5,7,6,8,9]. These nanostructures show potential applications in electronics [3,4], photonics [10], chemical sensors [5], field emission devices [11,7], solar cells [12], electrochemical performances [13], lithium ion battery [14], hydrogen storages [6] and drug delivery [8]. Researchers have put in a lot of efforts to investigate the nanoscale forms of silicon, for miniaturizing the microelectronic devices and to understand new properties that result at the nanoscale [15,16]. In addition to carbon and silicon, germanium (Ge) nanostructure is particularly interesting for future nanotechnology not only because of its similar structural and electronic properties to those of Si but also for many superior properties over Si in device applications [17]. For instance the higher intrinsic carrier mobility of Ge makes it a better channel material for high-performance field-effect logic transistors [18]. The larger excitonic Bohr radius of Ge yields a more pronounced quantum confinement effect than Si [19]. Furthermore, it is a potential anode material in lithium ion batteries, as the diffusivity of lithium in Ge is 400 times faster than in silicon at room temperature [20]. As Ge nanowires and nanotubes based on their properties are well suited as an anode in lithium ion batteries [20,14] compared to thin films, a further option to develop such Ge nanostructures would be of great interest. Germanium nanotubes as long as 2 μm have been grown using template assisted electrodeposition from a room temperature ionic liquid [21]. Preliminary evidence for nanotube compounds suggests that by virtue of introducing another element, the electronic properties and stability of these tubes can be significantly modified: specifically, band gaps get opened up, as other elements might trap the extra electrons from the tubes [22]. Schmidt and Eberl [23] fabricated SiGe nanotubes experimentally by using the method of the thin-film bending mechanism and found that SiGe nanotubes show excellent mechanical properties, indicating that they could be used as nanodrillers and microscopy tips. The calculations based on density functional theory have reported that SiC nanotubes are semiconducting in nature irrespective of chirality, which is not the case in carbon nanotubes [24,25]. SiC nanotubes are also being successfully synthesized in various laboratories using various methods [26,27] and it has also been suggested that SiC nanotubes can be a potential candidate for hydrogen storage [28]. Rathi and Ray [29] studied the electronic and geometric structures of hydrogenated GeC nanotubes and found the nanotubes to be semiconducting.

Many attempts have been made to explore the ground state geometric and electronic properties of CNTs, SiNTs, GeNTs [30,31,33,32,34–36]. There is a need to systematically study the optical and mechanical properties of these pristine and hetero nanotubes which have only been explored for pristine SiNT [37]. In this study our aim is to compare, the pristine nanotubes of group IV elements (C, Si and Ge) and their heterostructures and their relative stabilities in terms of their characteristic electronic

structures. We have looked at the structural, electronic (density of states and band structure), optical and mechanical properties of armchair (6,6) pristine and hetero nanotubes of group IV elements C, Si and Ge. As Compared to other nanotubes, armchair nanotubes have been found to have more stable structures due to the sufficient overlap of p_z orbitals and delocalization of π bonds [38]. Moreover, armchairs with (6,6) chirality have been found to be more stable in comparison to (4,0) and (5,5) configurations [39,40]. Due to this reason we have chosen (6,6) chirality in the present study. For simplicity, the pristine nanotube system is denoted by carbon nanotube (CNT), silicon nanotube (SiNT), germanium nanotube (GeNT) and hetero nanotube systems of silicon–carbon nanotube (SiCNT), germanium–carbon nanotube (GeCNT) and silicon–germanium nanotube (SiGeNT) respectively throughout the paper. The paper is organized as follows: in Section 2, brief computational details are presented. In Section 3, we present the calculated results and discuss these in the light of other available studies. Conclusions are presented in Section 4.

2. Computational details

In our study we have used well tested [37,41,42] Troullier Martin, norm-conserving, relativistic pseudopotentials [43,44] with valence atomic configuration $2s^2 2p^2$, $3s^2 3p^2$ and $4s^2 4p^2$ for C, Si and Ge respectively. The exchange and correlation energies were treated within the generalized gradient approximation (GGA) according to the PBEsol [45] parametrization. Throughout geometry optimization we have used numerical atomic orbitals with double zeta polarization (DZP) basis sets with confinement energy of 20 meV. For Brillouin zone integration, $1 \times 1 \times 30$ Monkhorst-Pack [46] mesh for both pristine and hetero nanotubes has been chosen. The convergence tolerance for the energy was chosen as 10^{-6} eV between two consecutive self-consistent field (SCF) steps. Minimization of the energy was carried out using the standard conjugate-gradients (CG) technique. Structures were relaxed until the forces on each atom were less than 0.01 eV/Å. The mesh cut-off energy used to calculate the Hartree, exchange and correlation contribution to the total energy and Hamiltonian was chosen to be 300 Ry. Also, a vacuum of 30 Å along the x -axis and the y -axis has been taken to ensure that there is no interaction between neighbouring nanotubes. The fully relaxed structures (*i.e.* minimum energy configuration) for all the systems *viz* CNT, SiNT, GeNT, SiCNT, GeCNT and SiGeNT were obtained by simultaneously relaxing both lattice vectors and atomic positions in unit cell. Pristine nanotubes were modelled by taking 24 atoms per unit cell whereas in the case of heterostructures 12 atoms per corresponding species were taken. In hetero systems the ratio of the corresponding two species is 1:1 at alternate positions.

3. Results and discussions

3.1. Structural properties

Fig. 1 shows a generic tube structure in different views *i.e.* cross-sectional, side and inner views for the systems under study, if atoms are of same type it is pristine and of two types it becomes a heterostructure. Heterogeneity is in the ratio 1:1.

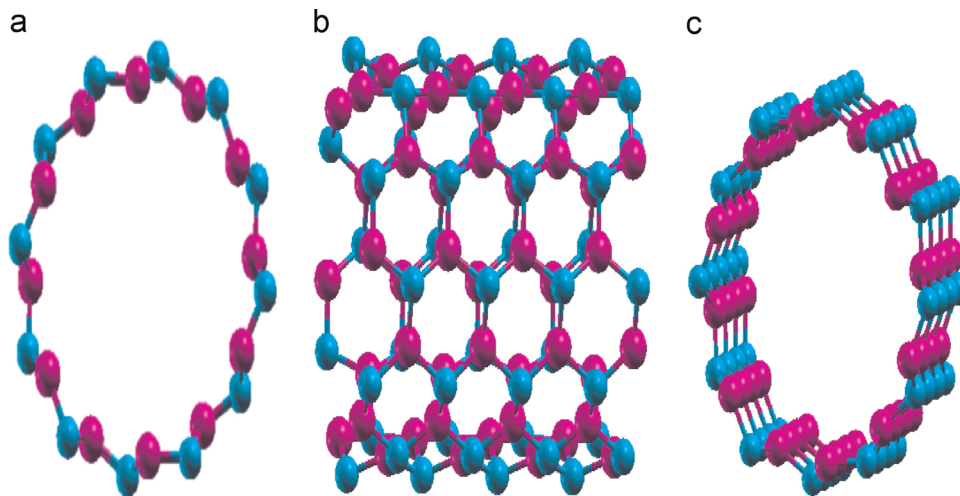


Fig. 1. Generic structural views of optimized hetero system SiGeNT; (a) cross-sectional view, (b) side view and (c) inner view respectively. Different colours represent different atoms forming the hetero structure of the tube. Other systems have similar structure with more or less buckling and have not been shown in the figure. (For interpretation of the references to colour in this figure caption, the reader is referred to the web version of this paper.)

To compare the stability of the systems under study, we have calculated the cohesive energy per atom (E_c), for each system using the following formula [33,47]:

$$E_c = \frac{E_{nA,nB} - n(E_A + E_B)}{2n} \quad (1)$$

where $n = 12$ atoms each for A and B types of species. E_A and E_B are the atomic ground state energies of corresponding two atomic species of heteronanotubes respectively. $E_{nA,nB}$ is the total energy of the optimized system. In case of pristine nanotube we have only one type of species, therefore, the above equation modifies to

$$E_c = \frac{E_T - 2nE_{atom}}{2n} \quad (2)$$

where E_T is the total energy of the pristine systems under study and E_{atom} the energy of the isolated atom of corresponding pristine system.

Table 1 shows the calculated physical parameters of nanotube systems. From the table it follows that interatomic distance in the optimized structures is found to be largest in GeNT in comparison to other pristine systems, while among the hetero nanotubes Si-GeNT system is found to have a highest bond length of 2.38 Å. The buckling parameters along x and y directions have been found to possess large values for GeNT (Table 1) out of pristine nanotubes,

Table 1
Lattice constant, bond length, diameter, buckling parameter and cohesive energy per atom for the systems under study.

System	Lattice constant (Å)	Bond length (Å)	Diameter (Å)	Buckling parameter $\Delta x, \Delta y$ (Å)	Cohesive energy (eV/atom)
CNT	2.48, 2.46 ^a	1.46, 1.43 ^b	8.30, 8.25 ^b	–	8.05
SiNT	3.87	2.31	13.10	0.39, 0.23	4.45
GeNT	4.21	2.40	13.43	0.56, 0.29	3.52
SiCNT	3.12	1.80, 1.87 ^c	10.22	0.06, 0.03	6.08, 6.16 ^d
GeCNT	3.28	1.89	10.50	0.03, 0.22	1.03
SiGeNT	4.00, 3.96 ^e	2.38, 2.36 ^e	12.80, 13.00 ^e	0.24, 0.20	2.30, 2.73 ^e

^a Ref. [48].

^b Ref. [49].

^c Ref. [50].

^d Ref. [52].

^e Ref. [53].

while SiGeNT appears to be more puckered in comparison to the other heteronanotubes under study, which may be attributed to large size of Ge atoms. The cohesive energy per atom is highest for CNT out of all the systems under study. However, out of hetero systems under study cohesive energy is largest for SiCNT system and least for GeCNT. The least value for cohesive energy of GeCNT may be attributed to large mismatch/difference between the sizes of C and Ge atoms. The calculated values match with other calculations where ever available for such systems [48–50,52,53] as listed in Table 1.

3.2. Electronic properties

To understand the electronic properties of the pristine and hetero nanotubes, electronic band structure and corresponding total and partial DOS as a function of energy have been plotted and are shown in Fig. 2. The electronic band structures for various systems under study have been calculated along the Γ -X direction of the Brillouin zone. The Fermi energy (E_f) has been set at 0 eV. On analysing the electronic band structure and corresponding DOS at the Fermi energy ($N(E_f)$), we find that all the pristine and hetero systems of nanotubes are semiconducting in nature except GeNT, which is metallic in nature. The main contribution towards the bands near the Fermi energy for all pristine systems is coming from its p_x -orbitals. However, for hetero systems contribution towards VB/CB is coming from p_x -orbitals of different species *i.e.* VB and CB are localized on different species. Out of semiconducting systems, SiCNT and GeCNT have been found to be indirect band semiconductors with a band gap of 2.05 eV and 1.71 eV respectively, while SiNT and SiGeNT are observed to have direct band gap of 0.18 eV and 0.37 eV respectively as listed in Table 2. In comparison to these systems under study, the pristine CNT has been found to be semimetallic (Dirac cone) with a extremely small band gap of 0.03 eV [49]. Out of the available results for SiCNT our value for the band gap is consistent with the results of Jiuxu et al. [51], however, they studied armchair (4,4) SiCNT using LDA functional.

3.3. Conductance

The quantum ballistic conductance of a system under ideal situation can be determined by the number of bands crossing the Fermi energy (E_f) [56]. For each band crossing the Fermi energy E_f , the ballistic conductance is G_0 which results into a conductance of nG_0 for n number of bands crossing the E_f . Therefore, on counting

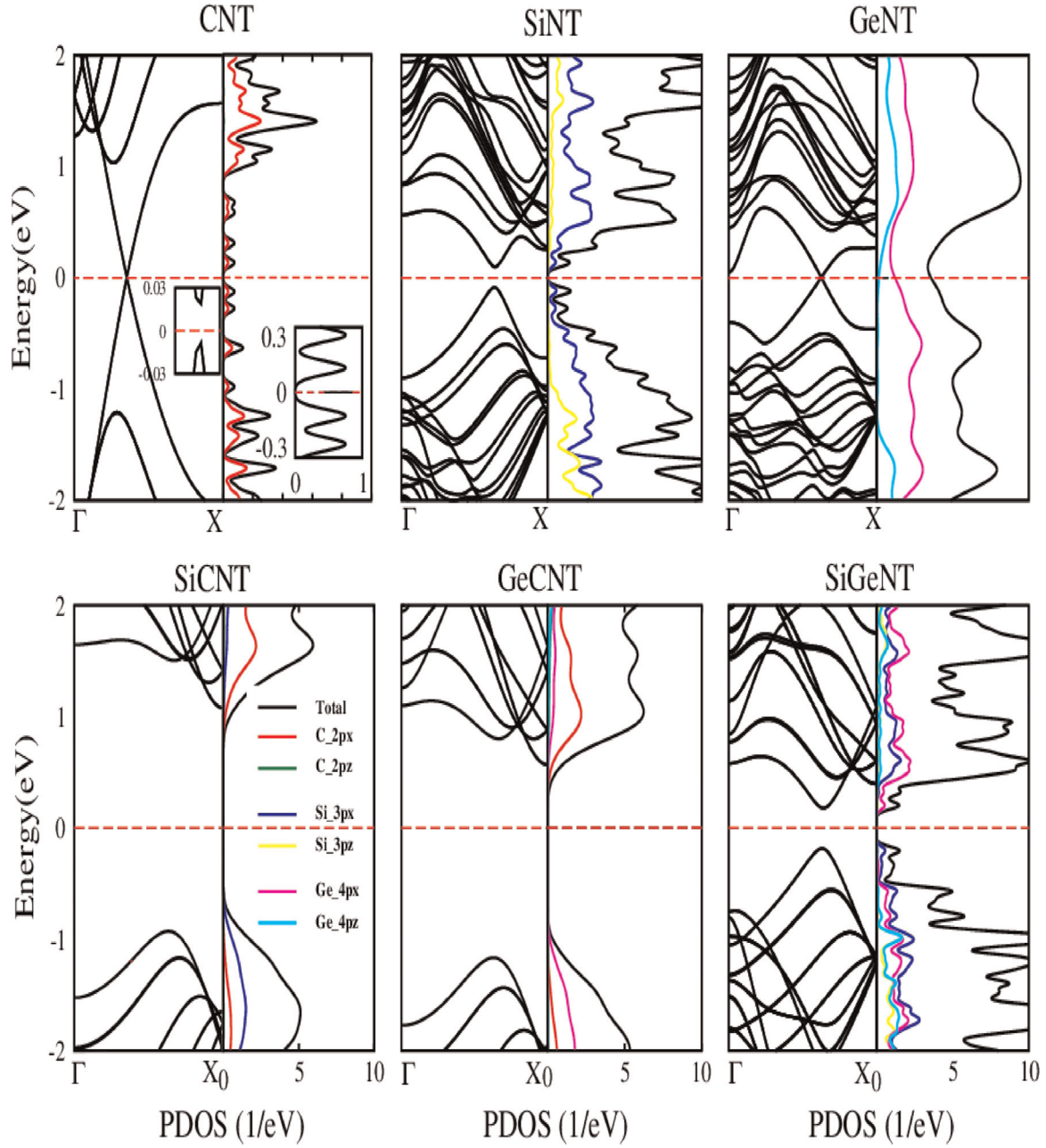


Fig. 2. Electronic band structure and corresponding total and partial DOS for pristine and heteronanotubes. In the inset we have shown the band structure and density of states for CNT in the vicinity of Fermi energy which shows semi-metallic behaviour.

Table 2

A list of number of channels crossing the Fermi energy ($N(E_f)$) and the value of band gap (E_g) for pristine and hetero systems.

System	$N(E_f)$	E_g (eV)	Tensile strength (GPa)
CNT	–	0.03 (Dirac cone), 0.003 (Dirac cone) ^a	10.56, 9.60 ^b
SiNT	–	0.18 (direct), 0.28 (direct) ^c	1.84
GeNT	2	– (metallic)	1.63
SiCNT	–	2.05 (indirect), 2.12 (indirect) ^d	3.56
GeCNT	–	1.71 (indirect)	2.51
SiGeNT	–	0.37 (direct)	1.44

^a Ref. [49].

^b Ref. [54].

^c Ref. [55].

^d Ref. [51].

the number of bands (Fig. 2) crossing the E_f in the electronic band structure of different nanosystems we find that the conductance is $2G_0$ for GeNT system (Table 2). In comparison, the conductance is zero for all other systems as these systems are found to be semi-conducting in nature with no band crossing the Fermi energy.

3.4. Charge density analysis

In order to gain insight into the interaction between different atoms of heteronanotubes, we have calculated the Mulliken charge associated with the corresponding atoms (Table 3). It is a method to accurately model partial charge magnitude on different species and locations within a molecule. From Table 3 it is clear that out of all the chosen systems Si atoms have been found to take partial

Table 3

The calculated Mulliken charge for the various species of heteronanotubes. The +ive (–ive) sign in Mulliken charge indicate the deficiency (excess) of electrons.

System	Mulliken charge associated with first species	Mulliken charge associated with second species
SiCNT	–5.60	+5.60
GeCNT	+0.84	–0.84
SiGeNT	–2.40	+2.40

charge from the other corresponding species which may be attributed to its vacant d-orbitals. In case of GeCNT, the screening effect is less pronounced in case of C as compared to Ge, since it lies at the top of the group. This effect lessens the attractive electrostatic charge as we move down the group. As a result of its effective nuclear charge, C has more tendency to gain the electrons as compared to Ge atoms. Moreover, C is more electronegative in comparison to Ge. Also, accumulation and depletion of charge in our Mulliken charge analysis is least in case of GeCNT in comparison to other systems which may be attributed to large size of Ge in comparison to C atom. Here, we conclude that more the charge redistribution within the hetero species, more is the cohesive energy *i.e.* it is highest for SiCNT and least for GeCNT (Tables 1 and 3).

Furthermore, we have also calculated the charge density difference to investigate interaction of atoms in heteronanotubes as shown in Fig. 3. It is calculated by taking the difference between the total charge density of the hetero system ($\rho_{\text{heteronanotube}}$) and the sum of the charge density of the individual systems A and B (ρ_A, ρ_B). *i.e.*

$$\Delta\rho = \rho_{\text{heteronanotube}} - (\rho_A + \rho_B) \quad (3)$$

The red regions show charge accumulation, while the green

Table 4

The calculated electronic band gap in eV for the various systems under study on the application of electric field at 0.5 V and 1 V.

Electric field	CNT	SiNT	GeNT	SiCNT	GeCNT	SiGeNT
0 V	0.03	0.18	0	2.05	1.71	0.37
0.5 V	0	0.08	0	0.96	0.46	0.13
1.0 V	0	0	0	0.04	0.02	0

regions represent charge depletion. The charge density distribution on different species of atoms of the nanotubes under study is consistent with the Mulliken charge analysis also. The redistribution of charges is more pronounced for SiCNT and SiGeNT as compared to GeNT. The inference drawn here is consistent with our Mulliken charge analysis.

3.5. Effect of external electric field on the electronic properties

It is well known that band gap engineering is a powerful technique and is an essential part of nanoelectronics and nanophotonics. Recent advances in engineering the band gap [57] motivated us to investigate the tuning of the band gap of the systems under study. Under the influence of external electric field electronic structure of the nanotubes can be effectively altered by applying it perpendicular to the tube axis [59]. The electronic band structure of the structures under study was calculated along the Γ -X direction of the Brillouin zone. The effect of the electronic band structures by means of the application of external electric field was studied in the steps of 0.1 V/Å up to a maximum of 1.0 V/Å. We observed a significant change in the band gap at 0.5 V and 1 V in comparison to the unbiased system as shown in Table 4. It is found that the band gap reduces to 47% for SiCNT in comparison to GeCNT (27%) and SiGeNT (35%) at 0.5 V, while at 1 V almost all the systems tend to be metallic. Thus, it is found that band gap

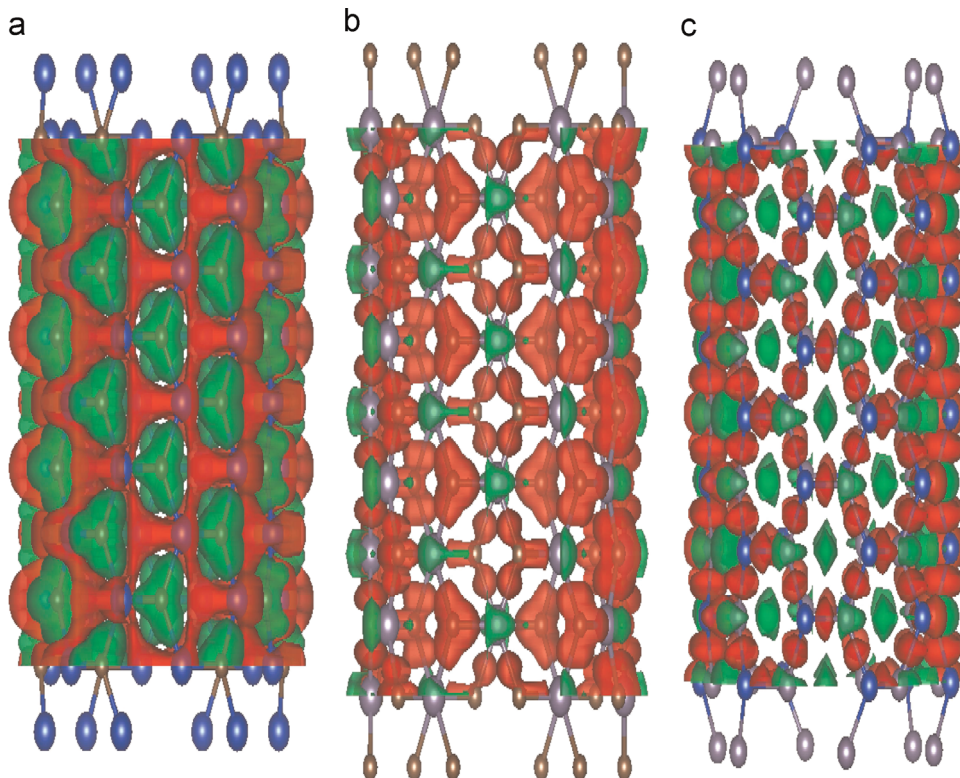


Fig. 3. Side view of charge density difference profiles for hetero systems of (a) SiCNT, (b) GeCNT and (c) SiGeNT. Here red/green regions show charge accumulation/depletion with largest accumulation and depletion in case of SiCNT system. The isosurface value is set at $0.006 \text{ e}/\text{\AA}^3$. (For interpretation of the references to colour in this figure caption, the reader is referred to the web version of this paper.)

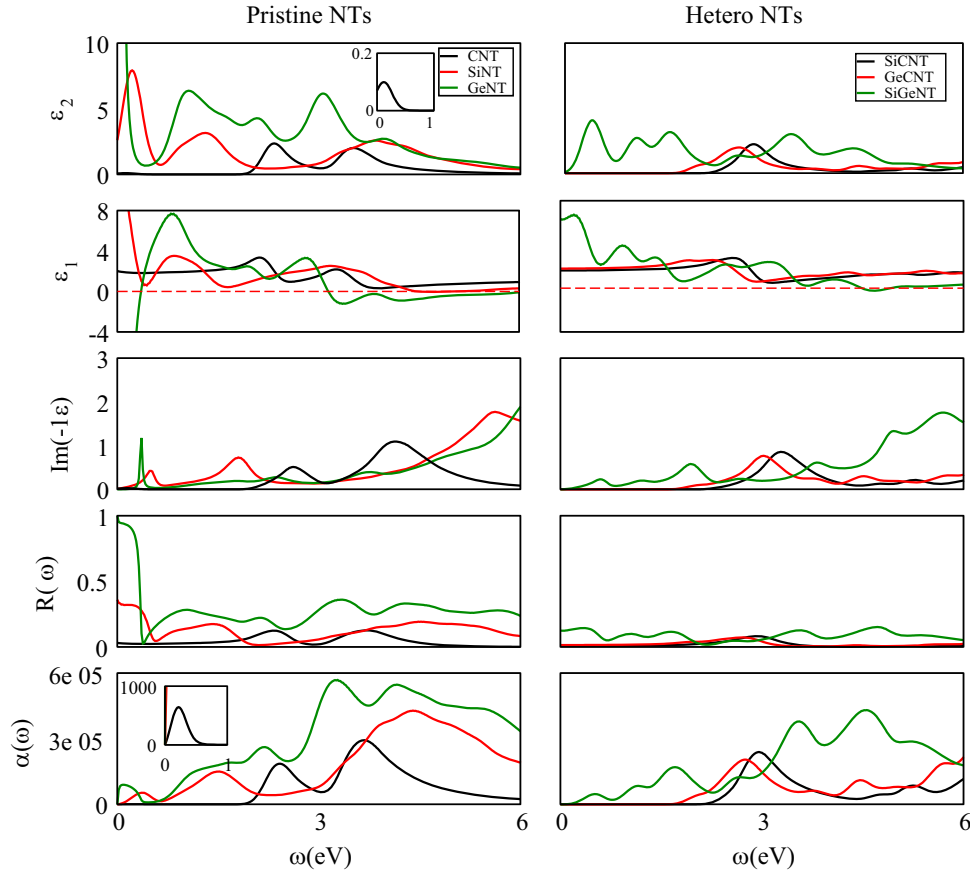


Fig. 4. Imaginary part of the dielectric function (ϵ_2), real part of the dielectric function (ϵ_1), EELS spectra, reflection $R(\omega)$ and absorption spectra $\alpha(\omega)$ for the systems under study have been shown. Insets show the first peak of (ϵ_2) and absorption edge corresponding to CNT.

generally decreases with an increase in biasing for all the systems under study, followed by semiconductor to metal transition at critical value of electric field.

3.6. Optical properties

The dielectric functions (ϵ_1 and ϵ_2), electron energy loss spectra (EELS), reflectance and absorptance spectra for the systems under study have been shown in Fig. 4. Here, we intend to discuss the results related to the dielectric function (real (ϵ_1) and imaginary part (ϵ_2)), EELS, reflectance (R) and absorption spectra for pristine and hetero nanotubes and a comparison across them. When ϵ_1 approaches zero, we observe a sharp resonance peak in EELS. The structural peaks associated with ϵ_2 are on account of interband transitions across E_f in the corresponding electronic band structure. CNT and SiNT pristine systems were observed to have three peaks each associated with (ϵ_2), whereas the heteronanotubes of SiCNT and GeCNT were found to have one peak each in comparison to three intense peaks for SiGeNT system. From Table 5, it was found that the ϵ_2 peaks for pristine systems are generally red shifted in comparison to hetero systems.

Electron energy loss spectra (EELS): EELS show sharp resonance peaks for the various systems under study. The pristine GeNT is found to have pronounced peak at 0.33 eV, which lies in the infrared region (0.00124–1.6531 eV). This peak corresponds to the loss of electron energy due to probability of inelastic scattering of light with the electrons. From Fig. 4 it follows that real part of the dielectric function ϵ_1 approaches zero value at the EELS peak positions. These peaks represent the collective excitation of electrons (plasmons) at these energies.

Table 5

A comparison of positions of the peaks of (ϵ_2) for the systems under study.

System	Position of the peak (ϵ_2)
CNT	0.05, 2.35, 3.52
SiNT	0.20, 1.33, 3.85
GeNT	–
SiCNT	2.80
GeCNT	2.55
SiGeNT	0.39, 1.59, 3.43

Reflection and absorption spectra: The reflection and absorption spectra for the systems under study have been shown in Fig. 4. It is found that reflectance spectra show sharp dip corresponding to the point at which ϵ_1 cuts the zero axis and EELS shows a resonance peak. These strong minima in the reflectance spectra correspond to the collective excitation of electrons and this sudden change reveals reflectance edge. The reflectance edge for GeNT system is found to be 0.33 eV which lies in infrared region (0.00124–1.6532 eV). Hence, GeNT is found to be transparent to the visible radiations. The hetero systems have wide band gap spectrum and hence will absorb the radiations corresponding to this energy. All other systems except pristine GeNT show semiconducting nature, and hence have no reflecting properties. The band gap for CNT, SiNT, SiGeNT lie in the infrared region and these semiconducting systems absorb all the radiations larger than the band gap and hence should appear blackish in colour, while the band gap for SiCNT and GeCNT lie in the visible region (1.6531–3.2627 eV). The rising edge in the absorption spectra indicates that

Table 6
A comparison of the position of observed reflectance and absorbance edges (in eV) for pristine and hetero nanotubes.

System	Reflection edge	Absorption edge
CNT	–	0.05
SiNT	–	0.17, 0.14 ^a
GeNT	0.33	–
SiCNT	–	2.20
GeCNT	–	1.84
SiGeNT	–	0.34

^a Ref. [55].

the systems absorb the radiations corresponding to their band gaps. The corresponding values of the absorption edge have been listed in Table 6.

3.7. Mechanical properties

Strain plays an important role when a crystal is compressed or stretched from its equilibrium position. It can affect the device performance and can be applied intentionally to improve the effective mass and hence the mobility [58]. Here we have applied compression and tensile strain (expansion) along the axis of the nanotubes to study the mechanical properties of the systems of interest.

Stress–strain relationship: In the present study, we investigate the strain–stress curves for considered nanotube structures by calculating the response of stress tensor components for the applied tensile strain. The stress tensor is defined as the positive derivative of total energy with respect to strain tensor [59]. The maximum stress that is achieved in response to tensile strain can be calculated from the highest value of stress at which the slope becomes zero in the stress–strain relationship. We calculated the stress tensor component for different values of tensile strain by studying variation of stress component with strain and hence calculated tensile strength for the nanotubes. We observed that there is a direct relationship between stress component and strain up to a certain value and after that it saturates. The point of saturation gives us the ultimate tensile strength. The variation of stress component as a function of applied strain is given in Fig. 5. It is evident from the figure that the strain at which the slope of strain–stress curve becomes zero is nearly 20% for all types of systems under study. The tensile strength is found to decrease in the following order: CNT > SiCNT > GeCNT > SiNT > GeNT > SiGeNT. Here, we can infer that the tensile strength of CNT is highest (10.56 GPa) in comparison to other systems. However, Li et al. [60] measured the tensile strength of carbon nanotubes to be as high as 22.2 ± 2.2 GPa in their experimental study with an average value of 11.5 GPa, while Zhou et al. calculated it to be 6.25 GPa [61]. Our result for tensile strength for (10.56 GPa) is consistent with the reported value of 9.26 GPa by Yao et al. [54].

Carriers effective mass: Since the heterostructuring and applied strain can change the curvature of valence band maximum (VBM) as well as conduction band minimum (CBM) [62], that can lead to the modification in carriers effective masses. Therefore, it is interesting to note the modification in the carrier effective mass of pristine and hetero structuring with the application of strain. A knowledge of the carrier effective mass is essential to account for the conduction process in realization of devices. In the present study, the effective mass of electron m_e^* and effective mass of hole m_h^* were calculated from the curvature of the energy band at CBM and VBM, respectively [62,63], as follows: $m^* = \hbar^2 / (\partial^2 E / \partial k^2)$.

It is worth mentioning here that our aim is to provide a general insight about the change in effective mass values on pristine and heterostructuring of the considered systems which is important

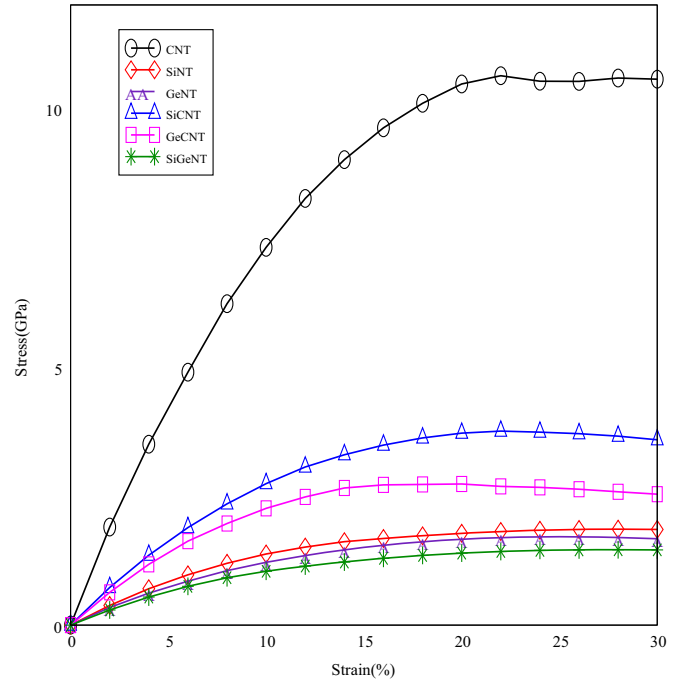


Fig. 5. Variation of stress component as a function of tensile strain.

Table 7

The calculated values of effective masses of electrons m_e^* and holes m_h^* in linear regime ($e=2\%$) for uniaxial tensile strain (a) and compression strains ($-a$) applied to pristine and heterostructures at VBM and CBM, in the units of mass of electron m_e .

System	Unstrained		Strained			
			+a		-a	
	m_e^*	m_h^*	m_e^*	m_h^*	m_e^*	m_h^*
CNT	0.006	0.007	0.013	0.127	0.013	0.007
SiNT	0.03	0.07	0.059	0.052	0.050	0.056
GeNT	0.015	0.012	0.06	0.014	0.009	0.012
SiCNT	0.67	0.67	0.037	0.43	0.032	0.35
GeCNT	0.61	0.35	0.05	0.47	0.84	0.42
SiGeNT	0.41	0.13	0.092	0.083	0.106	0.095

for device fabrication. From Table 7 it is evident that the effective mass of electrons, generally increases in case of pristine systems on applying the tensile strain and compression w.r.t. the unstrained system, a result because of the change in curvature of the valence and conduction bands with strain. The effective mass of holes decreases for pristine systems on the application of compression. Under no strain the effective mass of electrons is generally found to be larger than holes in hetero systems, while it is reverse in pristine systems. In case of unstrained systems, we generally observed that the more the effective mass of electron, the more is the band gap in the corresponding system (Tables 2 and 7). Thus, it is concluded that the mechanical strains offer tunability to carrier effective masses which may lead to mobility tuned electronic devices based on the studied pristine and heteronanotubes.

Strain dependent band structure: The strain is defined as ($e=\Delta a/a_0$) [64] and the strained unit cell is modelled by applying tensile as well as compression strains by varying the lattice value 'a' with strain 'e'. Here a_0 is an equilibrium lattice constant and Δa is the change in lattice constant simulating the strain. As strain

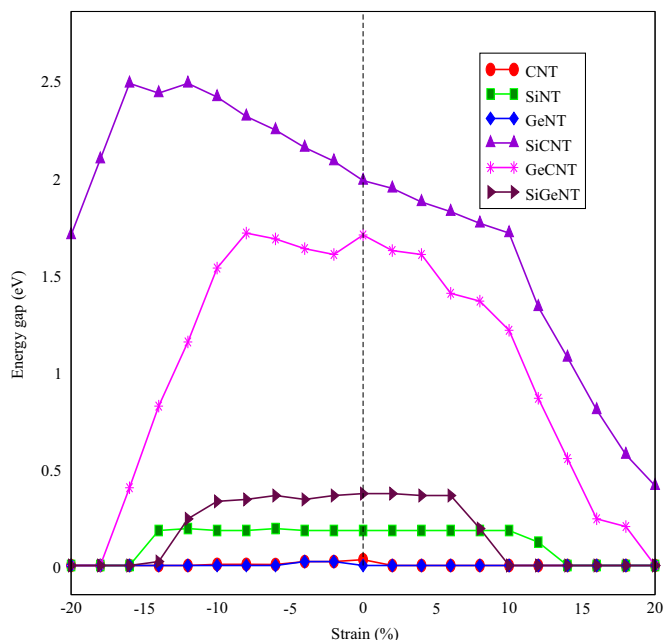


Fig. 6. Variation of electronic band gap as a function of applied strain (compression and expansion) on nanostructures under study.

offers tunability in band structure, therefore, we have applied uniaxial tensile and compression strain to the considered nanotubes. The tensile strain was applied as uniaxial expansion along the axis of tube. Similarly, compression strain was applied by uniaxial compression along the axis of the tube. In case of compression and expansion strains we studied the variation of electronic band structure, where we varied the strain from 2% to 20% and studied its impact on electronic band structure of nanotubes. The variation of the electronic band gap along with corresponding applied compression and tensile strain has been shown in Fig. 6. Here, we observed a significant opening of band gap under applied compression in the case of SiCNT up to a certain value in comparison to other systems. Our results are in good agreement with Wang et al. [65], though, they studied (9,9) armchair SiCNT. The band gap increases from 2.05 to a maximum of 2.49 eV as the nanotube is compressed and then decreases to 1.70 eV with further compression. However, the band gap closure does not occur in either case of compression or expansion in SiCNT. In comparison the band gap is found to close in all other cases under both expansion and compression. So far, as variation under tensile strain is concerned, the band gap has been found to decrease in all the cases as reported in Fig. 6. In case of CNT, SiNT, GeNT and SiGeNT there is negligible variation in the band gap as can be seen in the figure.

4. Conclusions

We have carried out a systematic study of pristine and heterotubes of group IV elements namely C, Si and Ge. The interatomic distance in the optimized structures is found to be largest in GeNT in comparison to other pristine systems, while among the hetero nanotubes SiGeNT system is found to have a highest bond length of 2.38 Å. GeNT and SiGeNT appear to be more puckered in comparison to the other pristine and heteronanotubes respectively. All the pristine and hetero nanotubes under study are found to be semiconducting in nature except GeNT which is found to be metallic in nature with a conductance of $2G_0$. GeNT, therefore, can be an ideal material for ballistic transport, while wide band gap

spectrum of hetero nanotubes opens up an arena for band gap selective engineered devices. Cohesive energy calculations reveal that SiCNT is more stable compared to other heterotubes. Mulliken charge population analysis shows that there is a net transfer of charge from Ge atoms towards Si and C atoms, which is supported by the charge density analysis. Our results show that band gap for SiCNT and GeCNT lie in the visible region (1.6531–3.2627 eV), while the band gap for other systems lie in the infrared region. The tuning of electronic band structure by means of intrinsic, extrinsic strain and external electric field indicates that the band gap can be altered considerably, it is found to close in all cases under both expansion and compression except SiCNT. The ultimate tensile strain of considered structures lies between 1.48 and 10.56 GPa, and the strain at which the slope of strain–stress curve becomes zero is nearly 20% for all types of systems under study. The effective masses are also found to show tunability with heterostructuring and applied strain. Therefore, such heteronanotubes are likely to have applications in nanoelectronic devices.

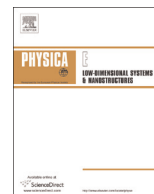
Acknowledgements

We gratefully acknowledge, SIESTA team for code and fruitful discussions with Dr. Ashok Kumar, D.S. Kothari Fellow, Panjab University Chandigarh and Munish Sharma, Inspire Fellow, Physics Department Himachal Pradesh University Shimla.

References

- [1] S. Iijima, *Nature (London)* 354 (1991) 56.
- [2] P. Avouris, M. Freitag, V. Perebeinos, *Nat. Photon.* 2 (2008) 341.
- [3] J. Bai, X.C. Zeng, H. Tanaka, J.Y. Zeng, *J. Proc. Natl. Acad. Sci. U.S.A.* 101 (2004) 2664.
- [4] P.R. Bandaru, C. Daraio, S. Jin, A.M. Rao, *Nat. Mater.* 4 (2005) 663.
- [5] J. Kong, N.R. Franklin, C. Zhou, M.G. Chapline, S. Peng, K. Cho, H. Dai, *Science* 287 (2007) 622.
- [6] J.H. Lan, D.J. Cheng, D.P. Cao, W.C. Wang, *J. Phys. Chem. C* 112 (2008) 5598.
- [7] C. Mu, Y.X. Yu, W. Liao, X.S. Zhao, D.S. Xu, X.H. Chen, D.P. Yu, *Appl. Phys. Lett.* 87 (2005) 113104.
- [8] Z. Liu, X. Sun, N. Nakayama, H. Dai, *ACS Nano* 1 (2007) 50.
- [9] Y.M. Niquet, A. Lherbier, N.H. Quang, M.V. Fernandez-Serra, X. Blase, C. Delerue, *Phys. Rev. B* 73 (2006) 165319.
- [10] B. Polyakov, B. Daly, J. Prikulis, V. Lissauskas, B. Vengalis, M.A. Morris, J. D. Holmes, D. Erts, *Adv. Mater.* 18 (2006) 1812–1816.
- [11] B.Q. Zeng, G.Y. Xiong, S. Chen, S.H. Jo, W.Z. Wang, D.Z. Wang, Z.F. Ren, *Appl. Phys. Lett.* 88 (2006) 213108.
- [12] B.Z. Tian, X.L. Zheng, T.J. Kempa, Y. Fang, N.F. Yu, G.H. Yu, J.L. Huang, C. M. Lieber, *Nature* 449 (2007) 885–890.
- [13] T. Song, H. Cheng, Heechae Choi, et al., *ACS Nano* 6 (2012) 30.
- [14] C.K. Chan, X.F. Zhang, Y. Cui, *Nano Lett.* 8 (2008) 307.
- [15] F. Rosei, *J. Phys. Condens. Matter* 16 (2004) S1373.
- [16] A. Polman, *Nat. Mater.* 1 (2002) 10.
- [17] X. Li, G. Meng, Q. Xu, M. Kong, X. Zhu, Z. Chu, A.P. Li, *Nano Lett.* 11 (2011) 1704.
- [18] B. Yu, X.H. Sun, G.A. Calebotta, G.R. Dholakia, M.J. Meyyappan, *Clust. Sci.* 17 (2006) 579.
- [19] H. Gerung, T.J. Boyle, L.J. Tribby, S.D. Bunge, C.J. Brinker, S.M. Han, *J. Am. Chem. Soc.* 128 (2006) 5244.
- [20] M.H. Park, Y. Cho, K. Kim, J. Kim, M. Liu, J. Cho, *Angew. Chem. Int. Ed.* 50 (2011) 9647.
- [21] A. Lahiri, A. Willert, S.Z.E. Abedin, F. Endres, *Electrochim. Acta* 121 (2014) 154.
- [22] C.C. Yang, J. Armellin, S. Li, *J. Phys. Chem. B* 112 (2008) 1482.
- [23] O.G. Schmidt, K. Eberl, *Nature* 410 (2001) 168.
- [24] Y. Miyamoto, B.D. Yu, *Appl. Phys. Lett.* 80 (2002) 586.
- [25] M. Zhao, Y. Xia, F. Li, R.Q. Zhang, S. Lee, *Phys. Rev. B* 71 (2005) 085312.
- [26] X.H. Sun, C.P. Li, W.K. Wong, N.B. Wong, C.S. Lee, S.T. Lee, B.T. Teo, *J. Am. Chem. Soc.* 124 (2002) 14464.
- [27] E.P. Borowiak, M.H. Ruemmel, T. Gemming, M. Knupfer, K. Biedermann, A. Leonhardt, T. Pihler, R.J. Kalenczuk, *J. Appl. Phys.* 97 (2005) 056102.
- [28] G. Mpourmpakis, G.E. Froudakis, G.P. Lithoxoos, J. Samios, *Nano Lett.* 6 (2006) 1581.
- [29] S.K.J. Rathi, A.K. Ray, *Nanotechnology* 19 (2008) 335706 (11 pp).
- [30] S. Reich, C. Thomson, P. Ordejon, *Phys. Rev. B* 65 (2002) 155411.
- [31] X.J. Du, Z. Chen, J. Zhang, C.S. Yao, C. Chen, X.L. Fan, *Phys. Status Solidi B* (2011) 1.
- [32] E. Durgun, S. Tongay, S. Ciraci, *Phys. Rev. B* 72 (2005) 075420.
- [33] P. Pradhan, A.K. Ray, *J. Comput. Theor. Nanosci.* 3 (2006) 128.

- [34] X. Yang, J. Ni, Phys. Rev. B 72 (2005) 195426.
- [35] A. Palaria, G. Klimech, A. Strachan, Phys. Rev. B 78 (2008) 205315.
- [36] J.E. Bunder, J.M. Hill, Phys. Rev. B 79 (2009) 233401.
- [37] S.K. Chandel, A. Kumar, P.K. Ahluwalia, R. Sharma, AIP conf. Proc. 1591 (2014) 531.
- [38] M. Zhang, Y.H. Kan, Q.J. Zang, Z.M. Su, R.S. Wang, Chem. Phys. Lett. 379 (2003) 81.
- [39] E. Durgun, S. Ciraci, Turk. J. Phys. 29 (2005) 307.
- [40] K.R. Byun, J.W. Kang, H.J. Hwang, J. Korean Phys. Soc. 42 (2003) 635.
- [41] N. Kumar, M. Sharma, J.D. Sharma, P.K. Ahluwalia, Indian J Phys. 89 (2) (2015) 143.
- [42] P. Jamdagni, A. Kumar, A. Thakur, R. Pandey, P.K. Ahluwalia, Mater. Res. Express 2 (1) (2015) 016301.
- [43] N. Troullier, José L. Martins, Phys. Rev. B 43 (1991) 1993.
- [44] N. Troullier, J.L. Martins, Phys. Rev. B 43 (1991) 8861.
- [45] J.P. Perdew, A. Ruzsinszky, G.I. Csonka, O.A. Vydrov, G.E. Scuseria, L. A. Constantin, X. Zhou, K. Burke, Phys. Rev. Lett. 100 (2008) 136406.
- [46] J. Moreno, J.M. Soler, Phys. Rev. B 45 (1992) 13891.
- [47] S.K. Chandel, A. Kumar, P.K. Ahluwalia, R. Sharma, Physica E 68 (2014).
- [48] M. Ge, K. Sattler, Appl. Phys. Lett. 65 (1994) 2284.
- [49] B.C. Wang, W.H. Chen, H.W. Wang, M. Hayashi, J. Phys. Chem. A 8 (2008) 112.
- [50] M. Menon, E. Richter, A. Mavrandonakis, G. Froudakis, A.N. Andriotis, Phys. Rev. B 69 (2004) 115322.
- [51] S. Jiuxu, Y. Yintang, L. Hongxia, G. Lixin, Z. Zhiyong, J. Semicond. 31 (11) (2010) 114003-1.
- [52] G. Mpourmpakis, G.E. Froudakis, G.P. Lithoxoos, J. Samios, Nano Lett. 6 (2006) 1581.
- [53] X. Liu, D. Cheng, D. Cao, Nanotechnology 20 (2009) 315705 (7 pp).
- [54] Z. Yao, C.C. Zhu, M. Cheng, J. Liu, Comput. Mater. Sci. 22 (2001) 180.
- [55] W. Wie, T. Jacob, Beilstein J. Nanotechnol. 5 (2014) 19–25.
- [56] B.K. Agrawal, V. Singh, R. Srivastava, S. Agrawal, Phys. Rev. B 74 (2006) 245405.
- [57] Y. Ma, Y. Dai, Y.B. Lu, B. Huag, J. Mater. Chem. C 2 (2014) 1125.
- [58] T.P. Kaloni, U. Schwingenschlogl, Chem. Phys. Lett. 583 (2013) 137.
- [59] M. Sharma, A. Kumar, P.K. Ahluwalia, R. Pandey, J. Appl. Phys. 116 (2014) 63711.
- [60] F. Li, H.M. Cheng, S. Bai, G. Su, M.S. Dresselhaus, Appl. Phys. Lett. 77 (2000) 3161.
- [61] G. Zhou, W. Duan, B. Gu, Chem. Phys. Lett. 333 (2001) 344.
- [62] A. Kumar, P.K. Ahluwalia, Physica B 419 (2013) 66.
- [63] S. Bhattacharya, A.K. Singh, Phys. Rev. B 86 (2012) 075454.
- [64] B. Mohan, A. Kumar, P.K. Ahluwalia, Physica E 61 (2014) 40.
- [65] Z. Wang, X. Zu, H. Xiao, F. Gao, W.J. Webe, Appl. Phys. Lett. 92 (2008) 183116.



A first principle study of encapsulated and functionalized silicon nanotube of chirality (6,6) with monoatomically thin metal wires of Ag, Au and Cu



Surjeet Kumar Chandel^{a,*}, Arun Kumar^b, P.K. Ahluwalia^a, Raman Sharma^a

^a Department of Physics, Himachal Pradesh University, Shimla, Himachal Pradesh 171005, India

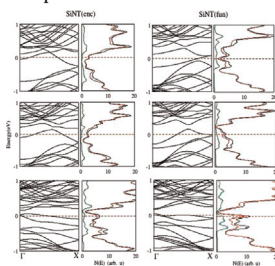
^b Department of Physics, Govt. College Banjar, Distt. Kullu, Himachal Pradesh 175123, India

HIGHLIGHTS

- We studied electronic and optical properties of encapsulated and functionalized SiNT.
- All encapsulated and functionalized systems are found to be metallic in nature.
- The conductance for functionalized Cu@SiNT system is found to be largest.
- There is a net transfer of charge from SiNT atoms to metal atoms of nanowires.
- All the systems under study show reflectivity in the IR region.

GRAPHICAL ABSTRACT

We present electronic band structure of the encapsulated and functionalized systems under study.



ARTICLE INFO

Article history:

Received 28 September 2014

Received in revised form

21 November 2014

Accepted 1 December 2014

Available online 4 December 2014

Keywords:

Silicon nanotubes

Encapsulation

Functionalization

Electronic and optical properties

ABSTRACT

First principle calculations have been performed to study the influence of interaction of monoatomically thin metal nanowires of Ag, Au and Cu placed inside (encapsulation) and outside (functionalization) the silicon nanotube having armchair conformation with chirality (6,6). The cohesive energy for all the encapsulated and functionalized systems under study was found to be almost same. In comparison to the pristine silicon nanotube (SiNT) which is found to be semiconducting in nature, all the encapsulated and functionalized systems of SiNT are found to be metallic in nature. The calculated electronic band structures show that the conductance in case of Ag, Au and Cu nanowires encapsulation is $2G_0$. However, its value for functionalized Ag, Au and Cu nanowires is found to be $1G_0$, $2G_0$ and $4G_0$ for the outside positioning of nanowires respectively. Optical properties of all the encapsulated and functionalized SiNTs have been studied. All the systems under study show reflectivity in the infrared (IR) region and behave as non-absorbing transparent conductors in the visible region.

© 2014 Elsevier B.V. All rights reserved.

1. Introduction

Over the last couple of decades miniaturization has been one of

the most important goals in device fabrication technology. It is an important area to look for new and exciting properties due to quantum confinement effects. By reducing dimensionality to nano level, the properties of the material, like geometrical structure, electronic band structure, magnetism, transport, and optical and hardness are generally found to be different from the corresponding macroscopic material [1]. The discovery of carbon nanotubes (CNT) by Iijima [2] in the early nineties inspired the

* Corresponding author.

E-mail addresses: skchandel2@yahoo.in (S. Kumar Chandel), arun242493@yahoo.com (A. Kumar), pk_ahluwalia7@yahoo.com (P.K. Ahluwalia), bramans70@yahoo.co.in (R. Sharma).

researchers to have a deep insight into nanoscale materials. However, beyond CNTs nano forms of Si may prove to be more conventional and economical instead of nanoforms of carbon, because Si is a key player of the existing integrated electronic circuits. Substantial efforts have been done to investigate the nanoscale forms of silicon, both for the purpose of further miniaturizing the current microelectronic devices and in the hope of unveiling new properties that often arise at the nanoscale [3,4]. Therefore, silicon based nanowires and nanotubes have been the subject of intense experimental and theoretical analyses [6,7,8,9,10,11,12]. Kang et al. [13] studied the structures and thermal behavior of SiNTs by using classical molecular dynamics simulations based on the Tersoff potential and found that the Si–Si bond length, cohesive energy per atom, diameter and elastic energy to bend the sheet into a tube of hypothetical SiNTs, based on the Tersoff potential, were in good agreement with those obtained from the density functional theory (DFT) [14]. Because of quantum confinement effects, SiNTs have a great potential for photoemission applications [15]. SiNTs have better electrochemical performances and hence can be used as anodes in the form of sealed SiNTs for lithium rechargeable batteries [5,16,17]. Motohike Ezawa [18] studied the buckled structure of SiNTs and found that the buckling along the application of electric field leads to tuning of band structure. Prachi Pradhan and Ray [19] examined the stability of silicon and germanium nanotubes and found that SiNTs appeared more stable in comparison to germanium nanotubes. Also out of (3,3), (4,4), (5,5) and (6,6) armchair silicon nanotubes, (6,6) armchair nanotube was found to have maximum cohesive energy per atom. Andriotis et al. [20] found that the encapsulation of metals (M=Ni and V) could stabilize SiNTs. They found that these metal encapsulated SiNTs were metallic in nature. Fagan et al. [14] showed that the production of graphite like sheets of silicon is a costly affair, but once they are formed the extra cost to produce the tubes is lower than it is for carbon. Theory based calculations show that metal encapsulation turns SiNTs to be a metal or a semiconductor with a very small band gap using density functional theory [21]. Singh et al. [22] found that the band structure of the Mn-doped ferromagnetic single walled hexagonal silicon nanotube showed a gap just above the Fermi energy for the one spin component, hence there could be possibilities of making half metallic nanotubes by including a small shift in the Fermi energy. Functionalization of NT's has also attracted a considerable interest in the fields of physics, chemistry, material science and biology, showing improved properties enabling two dimensional fabrication of novel materials and nanodevices [23]. The functionalization of SWNTs with biological molecules is a relatively new direction in exploring the chemistry of SWNTs for biosensor applications [24].

In this study our aim is to look at, the differences in structures and bonding arrangement of encapsulated and functionalized tubular nanostructures of silicon and their relative stabilities in terms of their characteristic electronic structures on interaction with monoatomically thin metal wires of Ag, Au and Cu from within (encapsulated) and outside (functionalized). Many attempts have been made to explore the ground state geometric and electronic properties of SiNTs [25–28]. But a systematic study of these properties by encapsulation and functionalization is desirable. In the present work we wish to study the structural, electronic (density of states and band structure) and optical properties of armchair (6,6) encapsulated and functionalized silicon nanotube. As Compared to other nanotubes, armchair nanotubes are the more stable structures due to their sufficient overlap of p_z orbitals and delocalization of π bonds [29]. Moreover SiNT (6,6) was found to be more stable in comparison to (4,0) and (5,5) configuration [30,31]. Due to this reason we have chosen (6,6) chirality in the present study. For simplicity, the combined system is denoted by M@SiNT (where M=Ag, Au, and Cu). We have used SiNT(enc)

and SiNT(func) for the encapsulated and functionalized SiNT respectively throughout the paper. The paper is organized as follows. In Section 2, brief computational details are presented. In Section 3, we present the calculated results and discuss these in the light of available data and the work is concluded in Section 4.

2. Computational details

In our study we have used well tested [32,33] Troullier Martin, norm-conserving, relativistic pseudopotentials [34,35] with valence atomic configuration $3s^2 3p^2$, $3d^{10} 4s^1$, $4d^{10} 5s^1$ and $5d^{10} 6s^1$ for Si, Cu, Ag and Au respectively. The (6,6) chirality has been chosen for modeling the nanotube because of its stability as compared to nanotubes of other chiralities. The exchange and correlation energies were treated within the generalized gradient approximation (GGA) according to the PBEsol [36] parametrization. Throughout geometry optimization we have used numerical atomic orbitals with double zeta polarization (DZP) basis sets with confinement energy of 20 meV. For Brillouin zone integration, $1 \times 1 \times 30$ Monkhorst-Pack [37] mesh for pristine SiNT, encapsulated SiNT and functionalized SiNT has been chosen. The convergence tolerance for the energy was chosen as 10^{-6} eV between two consecutive self-consistent field (SCF) steps. Minimization of the energy was carried out using the standard conjugate-gradients (CG) technique. Structures were relaxed until the forces on each atom were less than 0.01 eV/Å. The mesh cut-off energy used to calculate the Hartree, exchange and correlation contribution to the total energy and Hamiltonian was chosen to be 300 Ry. Also, a vacuum of 30 Å along x- and y-axes has been taken to ensure no interaction between neighboring nanotubes. The stable structures (i.e. minimum energy configuration) for all the encapsulated and functionalized systems viz Ag@SiNT, Au@SiNT and Cu@SiNT were obtained by simultaneously relaxing both lattice vectors and atomic positions in unit cell. In order to minimize the mismatch, Ag@SiNT and Au@SiNT systems were modeled by taking 51 atoms per unit cell whereas Cu@SiNT system was modeled by taking 77 atoms per unit cell; of these, three atoms are associated with each Ag and Au nanowires whereas in case of Cu@SiNT system five atoms are associated with Cu nanowire.

3. Results and discussions

3.1. Structural properties

Fig. 1 shows a generic tube structure composed of a core atomic wire and an outer wall in different views for the systems under study. The shape of the wire appears to be puckered due to a sufficient interaction between the wire and the nanotube. The deformed shape is almost same in all the cases.

To find the stability of the encapsulated systems, we have calculated the cohesive energy per atom (E_c), for each system as per the following formula [19]:

$$E_c = \frac{E_{Si_m W_n} - (mE_{Si} + nE_W)}{(m + n)} \quad (1)$$

where m is the number of silicon atoms and n is the number of atoms in the nanowire, and E_{Si} and E_W are the ground state energies of silicon and corresponding noble metal atoms respectively. $E_{Si_m W_n}$ is the total energy of the optimized encapsulated/functionalized system. Table 1 shows percentage lattice mismatch between nanowire and SiNT, their distance of separation, energy per atom and the for the encapsulated and functionalized systems under study. Here $R_{NT-wire}$ refers to the distance of wire from the

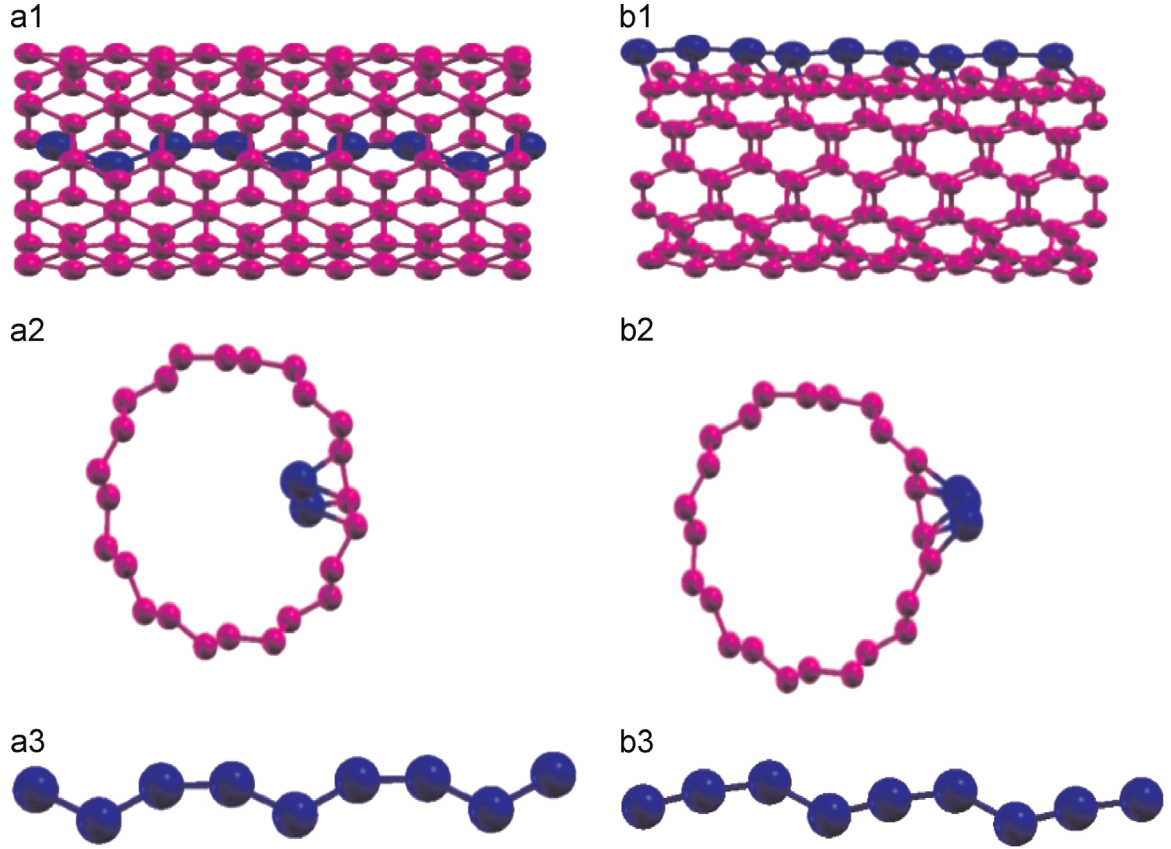


Fig. 1. Structural views of optimized encapsulated and functionalized SiNTs; (a.1) side view, (a.2) cross-sectional view, (a.3) core view of M@SiNT(enc); (b.1) side view, (b.2) cross-sectional view, (b.3) outer view of M@SiNT(func) systems respectively, where M=Ag, Au and Cu.

Table 1

Lattice mismatch (%), distance of separation between nanowire and SiNT ($R_{NT-wire}$ (Å)) cohesive energy per atom for the systems under study.

System	Lattice mismatch between (%) nanowire and SiNT enc/func	$(R_{NT-wire}$ (Å) enc (fun)	E_c (eV/atom) enc (fun)	Interatomic distance in nanowire enc (fun) Å
Ag@SiNT	2.7	2.16 (2.99)	−4.00 (−4.00)	2.79 (2.77) 2.65 ^a
Au@SiNT	0.7	2.02 (2.92)	−4.04 (−4.04)	2.72 (2.68) 2.60 ^a
Cu@SiNT	1.0	1.89 (2.78)	−4.03 (−4.03)	2.56 (2.32) 2.30 ^a

^a Ref. [33].

center of the nanotube. The wire was moved towards the surface of nanotube from its center in small steps to check its stability. Fig. 2 shows cohesive energy per atom versus position curve. It is found that the cohesive energy for encapsulated system (represented by left edge in each figure) is higher than that for corresponding functionalized system (represented by right edge in each figure). Zero on x-axis corresponds to the surface of nanotube in Fig. 2.

From Table 1 it follows that the cohesive energy per atom is same for all the systems under study. Also the interatomic distance of nanowires in the optimized structures of encapsulated and functionalized systems was found to be different. However, the interatomic distance is found to be more in nanowires of encapsulated/functionalized structures as compared to pristine nanowires [33]. This is attributed to the lattice mismatch between nanotube and nanowire. The interatomic distance in case of optimized encapsulated and functionalized SiNT is 2.30 Å in comparison to 2.36 Å for pristine SiNT [32], which is on account of the interaction between nanotube and nanowire.

In order to gain insight into nanowire interaction with SiNT, we have calculated the Mulliken charge associated with nanotube and the corresponding nanowire. From Table 2 it is clear that all the nanowires have been found to take partial charge from the SiNT which may be attributed to the electronegativity difference between the corresponding nanowire atoms and the SiNT atoms (Si= 1.90). In case of Cu there is a remarkable gain in the partial charge because according to the valence bond theory it will tend to complete its half filled 4s¹ orbital. Moreover, the screening effect is less pronounced in case of copper since it lies at the top of group. This effect lessens the attractive electrostatic charge as we move down the group. As a result of its effective nuclear charge, Cu has more tendency to gain the electrons as compared to other noble metals. It is pertinent to mention here that Cu nanowire in the functionalization configuration attains a maximum of −1.112 e partial charge in comparison to other chosen systems. In general, the charge transfer is more in functionalized systems as compared to encapsulated systems.

3.2. Charge density analysis

Furthermore we have also calculated the charge density difference to investigate the interaction of nanowire with SiNT as shown in Fig. 3. It is calculated by taking the difference between the total charge density of the combined system ($\rho_{SiNT+nanowire}$) and two isolated systems (ρ_{SiNT} , $\rho_{nanowire}$). i.e.

$$\Delta\rho = \rho_{SiNT+nanowire} - (\rho_{SiNT} + \rho_{nanowire}) \quad (2)$$

The red regions show charge accumulation, while the green regions represent charge depletion. The increased accumulation of charge between the two systems indicates strong interactions between the systems that results into decrease in energy gap of encapsulated systems. Accumulation of charge on the nanowire

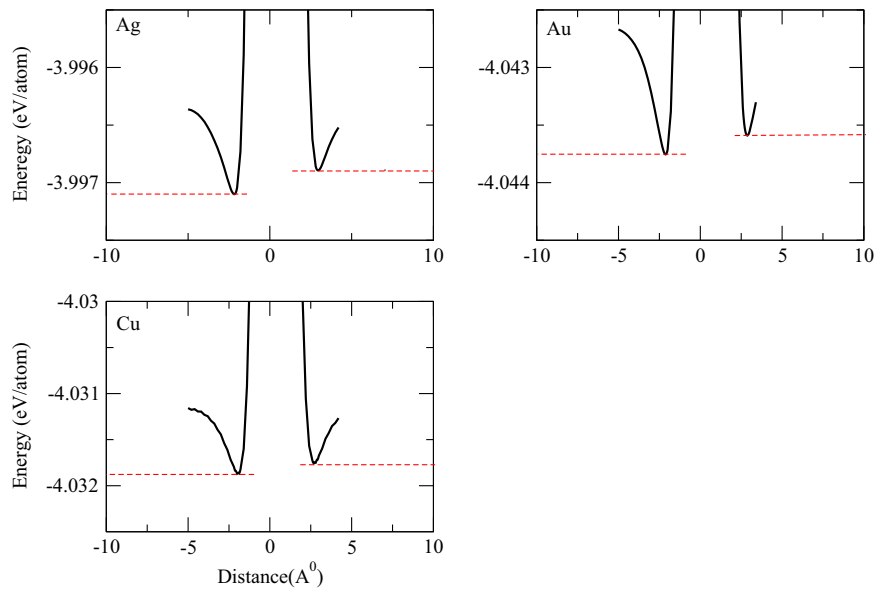


Fig. 2. Plot for cohesive energy per atom as a function of the position of nanowire for encapsulated and functionalized systems of M@SiNT systems, where M=Ag, Au and Cu. Zero on the X-axis represents the surface of nanotube.

Table 2

The calculated Mulliken charge at the wire and SiNT has been shown. The +ive (–ive) sign in Mulliken charge indicate the deficiency (excess) of electrons.

System	Mulliken charge associated with nanowire enc(fun)	Mulliken charge associated with SiNT enc(fun)	Electronegativity (Pauling scale)
Ag ($5s^1 4d^{10}$)	–0.14 (–0.28)	+0.14 (+0.28)	1.93
Au ($6s^1 5d^{10}$)	–0.03 (–0.14)	+0.03 (+0.14)	2.54
Cu ($4s^1 3d^{10}$)	–0.78 (–1.11)	+0.78 (+1.11)	1.90

atoms is due to greater electronegativity of these atoms as compared to the atoms of the nanotube, which results in charge transfer within the interacting atoms of SiNT and wire leading the change in band gap.

3.3. Electronic properties

To understand the electronic properties in encapsulated and functionalized SiNTs with noble metal nanowires, electronic band structure and corresponding PDOS and total DOS as a function of energy have been plotted and are shown in Fig. 4. The electronic band structures for various systems under study have been calculated along the Γ –X direction of the Brillouin zone. Fig. 4 represents the electronic band structure along with corresponding total as well as partial DOS of encapsulated and functionalized SiNTs respectively. The Fermi energy (E_f) has been set at 0 eV. On analyzing the electronic band structure and corresponding DOS at the Fermi energy ($N(E_f)$), we find that all the encapsulated/functionalized systems of SiNT are metallic in nature. DOS figures show that the states in the vicinity of Fermi energy are contributed mainly by the SiNT atoms which is supported by the electronegativity difference between the nanowire

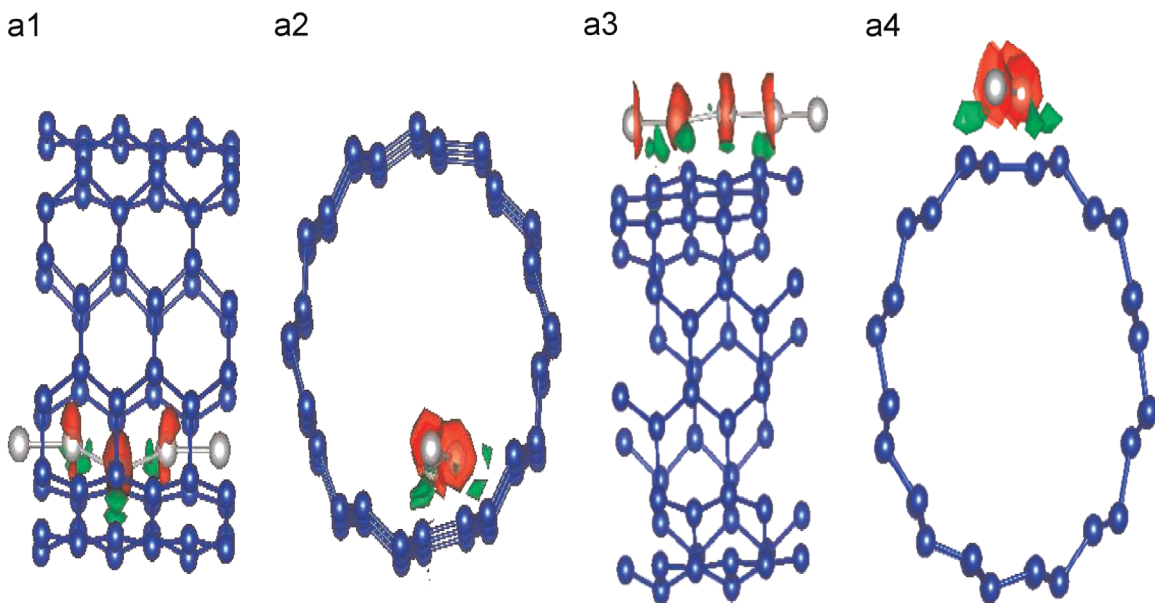


Fig. 3. Charge density analysis for encapsulated and functionalized systems of M@SiNT systems; (a.1) side view, (a.2) cross-sectional view of M@SiNT(enc), (a.3) side view and (a.4) cross-sectional view of M@SiNT(func) systems respectively, where M=Ag, Au and Cu. Here red regions show charge accumulation, while the green regions represent charge depletion. (For interpretation of the references to color in this figure caption, the reader is referred to the web version of this article.)

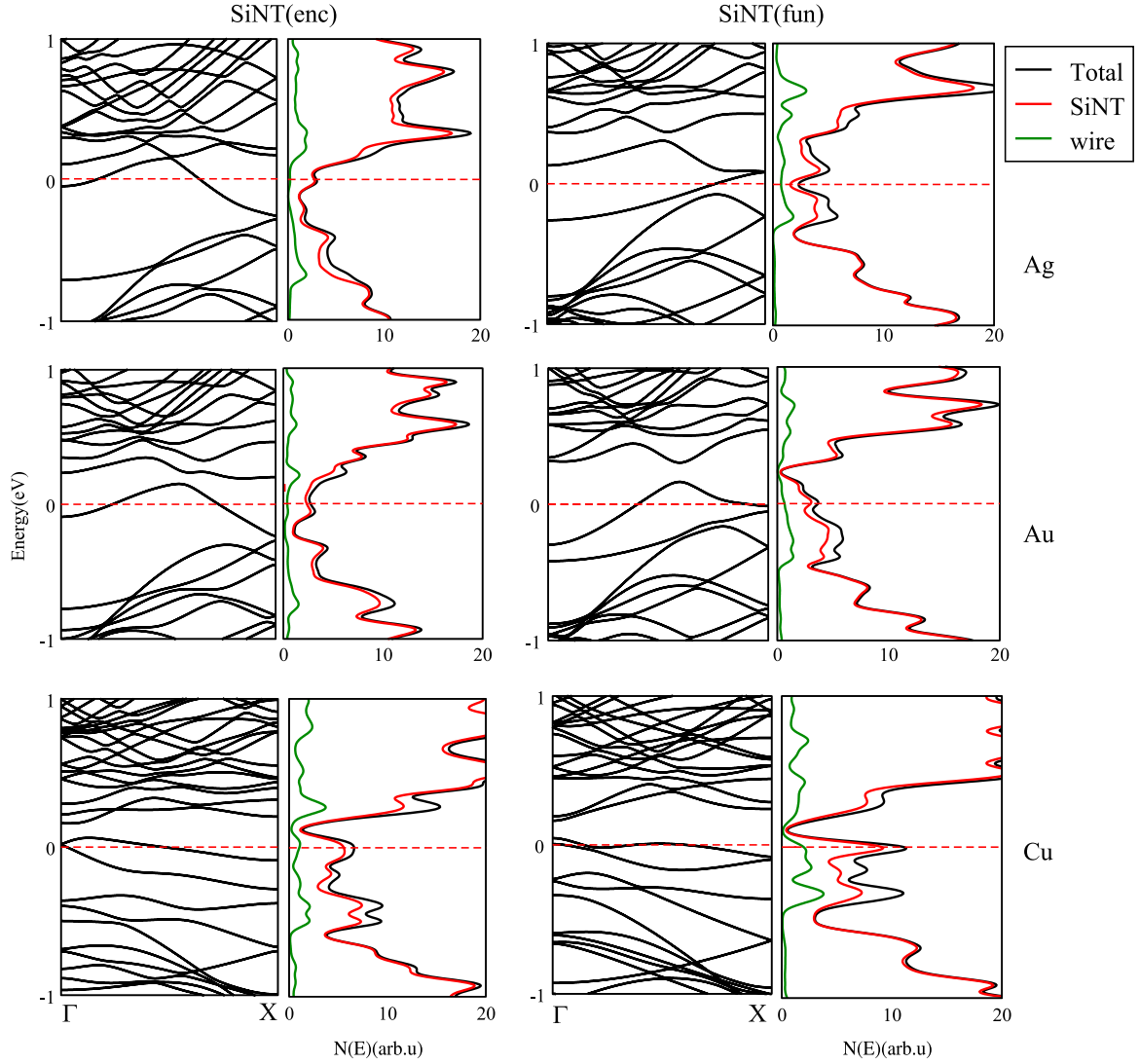


Fig. 4. Electronic band structure and corresponding total and partial DOS for encapsulated and functionalized SiNTs.

and SiNT atoms. Electronic DOS shows no band gap, which implies good conductivity. In comparison to the encapsulated/functionalized systems under study, the pristine SiNT has been found to be direct band semiconductor with a band gap of 0.18 eV [32].

Conductance. The quantum ballistic conductance of a system under ideal situation can be determined by the number of bands crossing the fermi energy (E_f) [38]. For each band crossing the E_f , the ballistic conductance is G_0 which results into a conductance of nG_0 for n number of bands crossing the E_f . Therefore, on counting the number of bands (Fig. 4) crossing the E_f in the electronic band structure of the different nanosystems we find that the conductance is $2G_0$ for Ag@SiNT, Au@SiNT and Cu@SiNT encapsulated systems. It is $1G_0$ and $2G_0$ for Ag@SiNT(func) and Au@SiNT(func) respectively (Table 3). In comparison to encapsulated and functionalized systems under study the pristine SiNT is found to be semiconducting in nature with no band crossing [32] *i.e.* having conductance $0G_0$, while all pristine nanowires of Ag, Au and Cu have conductance $1G_0$ [39]. Thus, on account of functionalization/encapsulation SiNT atoms create their atomic states around Fermi energy, which enhance the electric conductivity of the nanotube. The maximum value of conductance is $4G_0$ for Cu@SiNT(func) system, which is supported by larger value of Mulliken charge associated with this system.

Table 3

A list of number of channels crossing the Fermi energy ($N(E_f)$) and the value of band gap for the systems under study.

System	$N(E_f)$ (enc)	$N(E_f)$ (func)
Ag@SiNT	2	1
Au@SiNT	2	2
Cu@SiNT	2	4

3.4. Optical properties

The dielectric functions (ϵ_1 and ϵ_2), electron energy loss spectra (EELS) and reflectance spectra for the systems under study have been shown in Fig. 5. Here, we intend to discuss the results related to the dielectric function (real (ϵ_1) and imaginary part (ϵ_2)), EELS and reflectance spectra (R) for encapsulated and functionalized SiNT with nanowires of Ag, Au and Cu metals and a comparison with the corresponding pristine nanowire and pristine nanotube has been made. When ϵ_1 approaches to zero, we observe a sharp resonance peak in EELS. The plasmon frequency corresponding to these resonance peaks has been listed in Table 4. The plasmon frequency for Ag@SiNT, Au@SiNT and Cu@SiNT(func) systems lies between 0.16 and 0.46 eV an infrared region (0.00124–1.6531 eV) whereas it is 1.75 eV for Cu@SiNT(enc) systems, which lies in the

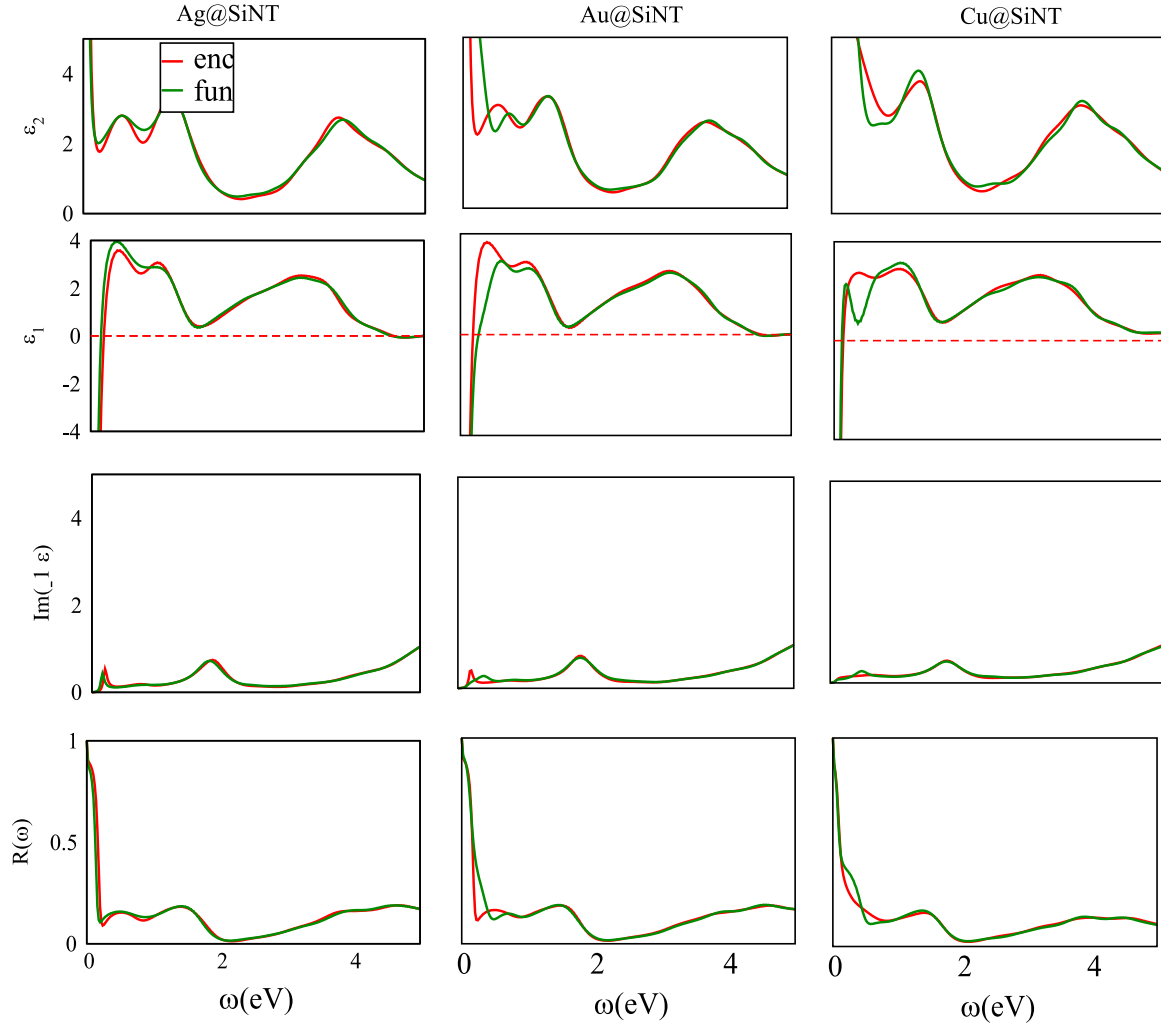


Fig. 5. Real part of the dielectric function (ϵ_1), imaginary part of the dielectric function (ϵ_2), EELS spectra and reflectance spectra for encapsulated and functional SiNT with nanowires of the metals under study have been shown.

Table 4

A comparison of position of the peak (ϵ_2) and ω_p (eV) for the systems under study and corresponding pristine nanowires. Here NW refers to nanowire.

System	Position of the peak (ϵ_2)	ω_p (eV)
Ag@SiNT(enc)	0.60, 1.32, 3.72	0.20, 1.83
Ag@SiNT(func)	0.60, 1.32, 3.74	0.16, 1.81
Au@SiNT(enc)	0.57, 1.31, 3.78	0.22, 1.88
Au@SiNT(func)	0.68, 1.31, 3.78	0.38, 1.88
Cu@SiNT(enc)	1.33, 3.78	1.75
Cu@SiNT(func)	1.32, 3.78	0.46, 1.75
SiNT(pristine)	0.21 ^b , 1.33 ^b , 3.85 ^b	0.50 ^b , 1.82 ^b
Ag NW(pristine)	3.27 ^a , 5.39 ^a	0.71 ^a
Au NW(pristine)	1.83 ^a , 5.13 ^a	0.69 ^a , 2.12 ^a
Cu NW(pristine)	1.34 ^a , 3.20 ^a	0.68 ^a

^a Ref. [33].

^b Ref. [32].

visible part of the spectrum (1.6531–3.2627 eV). It is worth mentioning here that pristine SiNT has 0.50 eV of plasmon frequency which belongs to infrared region (0.00124–1.6531 eV) [32]. The structural peaks associated with ϵ_2 are on account of interband transitions across E_f in the corresponding electronic band structure. Both encapsulated and functionalized systems of Ag@SiNT and Au@SiNT were observed to have three peaks associated with (ϵ_2), whereas the encapsulated and functionalized systems of Cu@SiNT were found to have two peaks each. In comparison the

pristine SiNT and pristine nanowires under study have been found to possess three peaks each [32,33]. These peaks indicate the interband transitions in the corresponding electronic band structure.

Electron Energy Loss Spectra (EELS). EELS show sharp resonance peaks for the encapsulated and functionalized systems under study. The encapsulated and functionalized systems of Ag@SiNT and Au@SiNT are found to have two peaks each in comparison to one peak for Cu@SiNT system. These peaks correspond to the loss of electron energy due to the probability of inelastic scattering of light with the electrons. From Fig. 5 it follows that real part of the dielectric function ϵ_1 has zero value at the EELS peaks positions. Thus these peaks represent the collective excitation of electrons (plasmons) at these energies. The plasmon frequencies (in eV) for the systems under study and the corresponding pristine counterpart are listed in the Table 4. The value of plasmon frequency increases for copper nanowire encapsulation and functionalization only, which lies in the visible region in comparison to the corresponding pristine nanowire an infrared region [33].

Reflectance spectra. The reflectance spectra for the systems under study have been shown in Fig. 5. It is found that reflectance spectra show sharp dip corresponding to the point at which ϵ_1 cuts the zero axis and EELS shows resonance peak. This strong minima in the reflectance spectra corresponds to the collective excitation of electrons and this sudden change reveals reflectance edge. The reflectance edge for all the systems is found to be in infrared region (0.00124 eV–1.6532 eV). The decrease in the

Table 5

A comparison of the position of observed reflectance edges (in eV) for encapsulated and functionalized systems under study with corresponding pristine nanowires. The percentage decrease in position of reflectance edges w.r.t. pristine nanowire is shown in brackets.

System	Ag	Au	Cu
SiNT(enc)	0.11 (85)	0.17 (75)	0.13 (81)
SiNT(func)	0.10 (86)	0.17 (75)	0.13 (81)
NW(pristine)	0.71 ^a	0.69 ^a	0.68 ^a

^a Ref. [33].

position of reflectance edge of the systems under study w.r.t. pristine nanowire has been shown in Table 5. The decreasing order for reflectance is Au@SiNT > Cu@SiNT > Ag@SiNT and pristine SiNT. It is concluded that all the encapsulated systems show reflectivity in the IR region and behave as a non-absorbing transparent conductor in the visible region. In comparison the pristine SiNT shows semiconducting nature and due to this reason do not show reflecting properties [32]. The band gap lies in the infrared region and this semiconducting system absorbs all the radiations larger than the band gap and hence appears to be blackish in color.

It has been found that Ag@SiNT(func) system shows largest decrease (86%), whereas smallest decrease is observed for Au@SiNT(enc) and Au@SiNT(enc) systems, *i.e.* 75%.

4. Conclusions

In comparison to pristine SiNT all the encapsulated and functionalized systems in our study are found to be metallic in nature. It is concluded that the conductance can be enhanced through functionalization of Cu@SiNTs. On account of their enhanced conductance in comparison to pristine SiNT all the encapsulated/functionalized SiNTs can also be anticipated as a material for nanoscale electronic devices, an ideal material for ballistic transport. Mulliken population and charge density analysis show that there is a net transfer of charge from SiNT atoms to metal atoms of nanowires with more charge transfer in case of SiNT(func) as compared to SiNT(enc). It is also concluded that all the encapsulated and functionalized systems show reflectivity in the IR region and behave as a non-absorbing transparent conductor in the visible region. The decreasing order for reflectance is Au@SiNT > Cu@SiNT > Ag@SiNT for both encapsulated and functionalized SiNT.

Acknowledgments

We gratefully acknowledge, SIESTA team for code.

References

- [1] A.G. Fuente, V.M.G. Saurez, J. Ferrer, A. Vega, J. Phys. Condens. Matter 23 (2011) 265302.
- [2] S. Iijima, T. Ichihashi, Nature (London) 363 (1993) 603.
- [3] F. Rosei, J. Phys. Condens. Matter 16 (2004) S1373.
- [4] A. Polman, Nat. Mater. 1 (2002) 10.
- [5] T. Song, J. Xia, J. Lee, D. Lee, M. Kwon, J. Choi, J. Wu, S.K. Doo, H. Chang, W. I. Park, D.S. Zang, H. Kim, Y. Huang, K. Hwang, J.A. Rogers, U. Paik, Nano Lett. 10 (2010) 1710.
- [6] J. Shah, J. Niu, X. Ma, J. Xu, X. Zhang, Q. Yang, D. Yang, Adv. Mater. 14 (2002) 1219.
- [7] M.D. Crescenzi, et al., Appl. Phys. Lett. 86 (2005) 23190.
- [8] J.W.G. Wildoer, L.C. Venema, A.G. Rinzler, R.E. Smalley, C. Dekker, Nature 391 (1998) 59.
- [9] T.M. Odom, J.L. Huang, P. Kim, C.M. Lieber, Nature 391 (1998) 62.
- [10] J.C. Charlier, Ph. Lambin, Phys. Rev. B 57 (1998) R15037.
- [11] G. Zhou, W.H. Duan, B.L. Gu, Chem. Phys. Lett. 333 (2001) 344.
- [12] S.Y. Jeong, J.Y. Kim, H.D. Yang, B.N. Yoon, S.H. Choi, S.J. Eum, C.W. Yang, Y.H. Lee, Adv. Mater. 15 (2003) 1172.
- [13] J.W. Kang, J.J. Seo, H.J. Hwang, J. Nanosci. Nanotechnol. 2 (2002) 687.
- [14] S.B. Fagon, R.J. Baierie, R. Mota, A.J. da Silva, A. Fazzio, Phys. Rev. B 61 (2000) 9994.
- [15] M. Taghinejad, H. Taghinejad, M. Abdolhad, S. Mohajerzadeh, Nano Lett. 13 (2013) 899.
- [16] M.H. Park, M.G. Kim, J. Joo, K. Kim, J. Kim, S. Ahn, Y. Cui, J. Cho, Nano Lett. 9 (2009) 3844.
- [17] H. Wu, G. Chan, J.W. Choi, Ill. Ryu, Y. Yao, M.T. McDowell, S.W. Lee, A. Jackson, Y. Yang, L. Hu, Y. Cui, Nat. Nanotechnol. 7 (2012) 310.
- [18] Motohiko Ezawa, Europhys. Lett. 98 (2012) 67001.
- [19] P. Pradhan, A.K. Ray, J. Comput. Theor. Nanosci. 3 (2006) 128.
- [20] A.N. Andriotis, G. Mpourmpakis, G.E. Froudakis, M. Menon, New J. Phys. 4 (2002) 78.
- [21] L. Guo, X. Zheng, Z. Zeng, Phys. Lett. A 375 (2011) 4209.
- [22] A.K. Singh, T.M. Briere, V. Kumar, Y. Kawazoe, Phys. Rev. Lett. 91 (2003) 146802.
- [23] L. Meng, C. Fu, Q. Lu, Progr. Nat. Sci. 19 (2009) 801.
- [24] E. Bekyarova, B. Zhao, Rv Sen, M.E. Itkis, R.C. Haddon, Am. Chem. Soc. Div. Fuel Chem. 49 (2) (2004) 936.
- [25] E. Durgun, S. Tongay, S. Ciraci, S. Phys. Rev. B 72 (2005) 075420.
- [26] X. Yang, J. Ni, Phys. Rev. B 72 (2005) 195426.
- [27] A. Palaria, G. Klimech, A. Strachan, Phys. Rev. B 78 (2008) 205315.
- [28] J.E. Bunder, J.M. Hill, Phys. Rev. B 79 (2009) 233401.
- [29] M. Zhang, Y.H. Kan, Q.J. Zang, Z.M. Su, R.S. Wang, Chem. Phys. Lett. 379 (2003) 81.
- [30] E. Durgun, S. Ciraci, Turk. J. Phys. 29 307 (2005).
- [31] K.R. Byun, J.W. Kang, H.J. Hwang, J. Kor. Phys. Soc. 42 (2003) 635.
- [32] S.K. Chandel, A. Kumar, P.K. Ahluwalia, R. Sharma, AIP Conf. Proc. 1591 (2014) 531.
- [33] A. Kumar, A. Kumar, P.K. Ahluwalia, Phys. E 46 (2012) 259.
- [34] N. Troullier, José L. Martins, Phys. Rev. B 43 (1991) 1993.
- [35] N. Troullier, J.L. Martins, Phys. Rev. B 43 (1991) 8861.
- [36] J.P. Perdew, A. Ruzsinszky, G.I. Csonka, O.A. Vydrov, G.E. Scuseria, L. A. Constantin, X. Zhou, K. Burke, Phys. Rev. Lett. 100 (2008) 136406.
- [37] J. Moreno, J.M. Soler, Phys. Rev. B 45 (1992) 13891.
- [38] B.K. Agrawal, V. Singh, R. Srivastava, S. Agrawal, Phys. Rev. B 74 (2006) 245405.
- [39] A. Kumar, P.K. Ahluwalia, J. Alloys Compds. 615 (2014) 194.

Electronic, Mechanical, and Dielectric Properties of Two-Dimensional Atomic Layers of Noble Metals

POOJA KAPOOR,^{1,5} JAGDISH KUMAR,² ARUN KUMAR,³
ASHOK KUMAR,⁴ and P.K. AHLUWALIA^{1,6}

1.—Physics Department, Himachal Pradesh University, Shimla, Himachal Pradesh 171005, India. 2.—Physics Department, Central University of Himachal Pradesh, Dharamshala, Himachal Pradesh, India. 3.—Physics Department, Govt. College Banjar, Kullu, Himachal Pradesh, India. 4.—Centre for Physical Sciences, School of Basic and Applied Sciences, Central University of Punjab, Bathinda 151001, India. 5.—e-mail: pupooja16@gmail.com. 6.—e-mail: pk_ahluwalia7@yahoo.com

We present density functional theory-based electronic, mechanical, and dielectric properties of monolayers and bilayers of noble metals (Au, Ag, Cu, and Pt) taken with graphene-like hexagonal structure. The Au, Ag, and Pt bilayers stabilize in AA-stacked configuration, while the Cu bilayer favors the AB stacking pattern. The quantum ballistic conductance of the noble-metal mono- and bilayers is remarkably increased compared with their bulk counterparts. Among the studied systems, the tensile strength is found to be highest for the Pt monolayer and bilayer. The noble metals in mono- and bilayer form show distinctly different electron energy loss spectra and reflectance spectra due to the quantum confinement effect on going from bulk to the monolayer limit. Such tunability of the electronic and dielectric properties of noble metals by reducing the degrees of freedom of electrons offers promise for their use in nanoelectronics and optoelectronics applications.

Key words: Density functional theory (DFT), electronic properties, mechanical properties, dielectric properties, noble-metal atomic layers

INTRODUCTION

Noble metals in the form of nanoparticles,¹ nanowires, nanorods, nanoclusters,² and nanosheets have attracted immense interest due to their encouraging applications in the fields of electronics,² catalysis, photonics, and sensing.^{3,4} In the past, special attention has been paid to shape- and size-controlled synthesis of noble-metal nanoparticles due to their wide range of tunable properties^{5–8} for application in nano-biosensing,⁹ surface-enhanced Raman spectroscopy (SERS),^{10,11} diagnostics,¹² photothermal and therapeutic applications,¹³ generation of nanophotonic devices,¹⁴ and related biological and medical fields.^{15,16} The optical

properties of metallic (Ag, Cu) nanoparticles (NPs) embedded in glass matrices have received huge attention from the viewpoints of basic research and their applications.^{17,18}

Noble metals in two-dimensional (2D) form with thickness ranging from 10 nm to 500 nm possess unusual physical¹⁹ and chemical properties²⁰ due to strong quantum confinement and surface effects. Two-dimensional layers of noble metals have numerous technological applications, e.g., in catalysis,^{21,22} microelectromechanical and nanoelectromechanical systems, as interconnects in molecular circuits, sensors,²³ plasmonics,²⁴ devices for surface-enhanced Raman spectroscopy (SERS),²⁵ and the biomedical area.²⁶ Furthermore, it is expected that various new materials in the form of nanoclusters, nanorods, nanoflakes, nanoribbons, and nanocages can be derived by using these nanolayers as building blocks.²⁷

COMPUTATIONAL METHODS

Recently, experiments using gold nanolayers were carried out, revealing promising applications in next-generation electronic devices.^{28–33} Au multilayers have been used as stretchable electrodes for organic-based electronic devices,³⁴ displays,³⁵ field-effect transistors (FETs),³⁶ and energy-related devices.³⁷ Similarly, experimentally synthesized silver nanosheets³⁸ have been found to be useful for tuning surface-enhanced Raman spectroscopy (SERS), metal-enhanced fluorescence, and as scanning tunneling microscopy (STM) substrates.⁶ Additionally, layered Pt sheets show promise for electrochemical conversion and catalysis.³⁹ A 2D Cu nanosheet has also been used as a novel material for aqueous conductive ink in flexible electronics because of its low price and high conductivity.⁴⁰ Note that synthesis of Cu monolayers is challenging, with only a few techniques being available, because Cu readily converts to CuO or CuS layers.

Motivated by the above experimental results involving 2D noble-metal layers, we present herein a density functional theory (DFT)-based computational study of structural, electronic, mechanical, and dielectric properties of monolayers and bilayers of noble metals (Cu, Ag, Au, and Pt). Efforts were made to explore the structural and mechanical stability of the mono- and bilayer noble metals and the possible technological implications.

All calculations were performed using the *Spanish Initiative for Electronic Simulation with Thousands of Atoms* (SIESTA) code,⁴¹ which uses *ab initio* pseudopotential-based density functional theory (DFT). We used well-tested⁴² Troullier–Martins, norm-conserving relativistic pseudopotentials^{43,44} for the different noble metals in fully separable Kleinman–Bylander form. The exchange and correlation energies were treated within the generalized gradient approximation (GGA) according to the Perdew–Burke–Ernzerhof (PBE) parameterization.⁴⁵ Numerical atomic orbitals (NAOs) with a double zeta polarization (DZP) basis set with confinement energy of 0.01 Ry were used for geometry optimization. Energy minimization in each case was carried out using the standard conjugate-gradients (CG) technique. All structures were relaxed until the force on each atom was less than 0.01 eV/Å. A $40 \times 40 \times 1$ Monkhorst–Pack⁴⁶ \mathbf{k} -point grid was used for sampling the Brillouin zone. The mesh cutoff energy was taken as 200 Ry. We took two atoms in the unit cell for monolayers and four atoms in the unit cell for bilayers in our calculations. A vacuum region of about 16 Å was used to separate the two-dimensional layers along the c -axis to ensure that there was no interaction between periodic images. Dielectric properties were

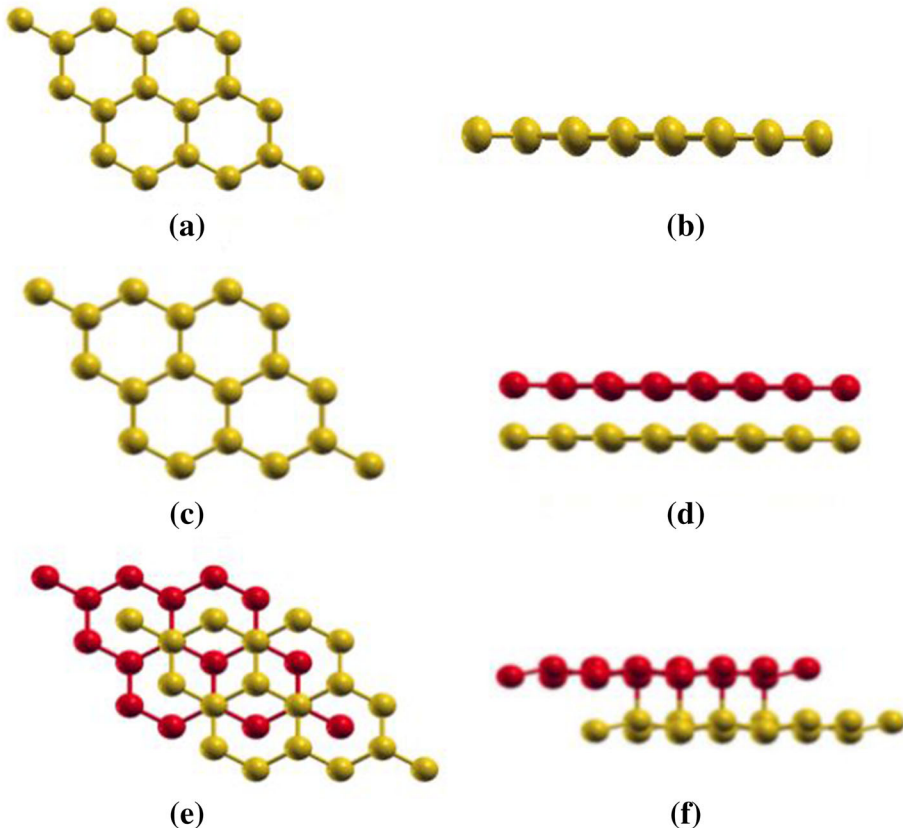


Fig. 1. (a) Top view of monolayer. (b) Side view of monolayer. (c) Top view of AA-stacked bilayer. (d) Side view of AA-stacked bilayer. (e) Top view of AB-stacked bilayer. (f) Side view of AB-stacked bilayer.

calculated using first-order time-dependent perturbation theory as implemented in the SIESTA package.^{47,48} A $60 \times 60 \times 3$ optical mesh and 0.2 eV optical broadening were used for calculations of dielectric properties. It is necessary to include a Drude term associated with intraband transitions in the case of metals, which is of the form

$$\varepsilon_{\text{Drude}}(\omega) = \omega_p^2 / \omega(\omega + i \times \gamma), \quad (1)$$

where ω_p^2 is calculated by the SIESTA code itself and γ is an empirical parameter, which is the

inverse of the relaxation time (τ). The values of γ for Cu, Ag, Au, and Pt were taken as 0.001 Ha (0.0272 eV), 0.0005 Ha (0.0136 eV), 0.003 Ha (0.0686 eV), and 0.001 Ha (0.0272 eV), respectively,⁴⁹ for bulk, monolayers, and bilayers.

RESULTS AND DISCUSSION

Since gold nanosheets (about 16 atomic layers thick) have been reported experimentally to be synthesized with hexagonal closed-packed (hcp) structure,⁴ the noble-metal mono- and bilayers

Table I. Calculated values of lattice parameter (a in Å), binding energy (ΔE_b in eV, all values negative but minus sign omitted) for bilayers, interlayer spacing (Δd in Å), and covalency metric (C_d in eV)

Property	System	Cu	Ag	Au	Pt
a (Å)	Bulk	3.69 (3.62) ^a	4.19 (4.09) ^a	4.20 (4.08) ^a	4.03 (3.93) ^a
	Monolayer	4.05	4.71	4.61	4.31
	Bilayer	4.17	4.73	4.69	4.43
ΔE_b (eV)	Bilayer	0.59	0.47	0.40	1.31
Δd (Å)	Bilayer	2.83	2.79	2.45	2.55
C_d (eV)	Monolayer	-1.90	-0.77	-2.00	-2.28
	Bilayer	-1.56	-0.75	-1.69	-1.56

^aRef. 42.

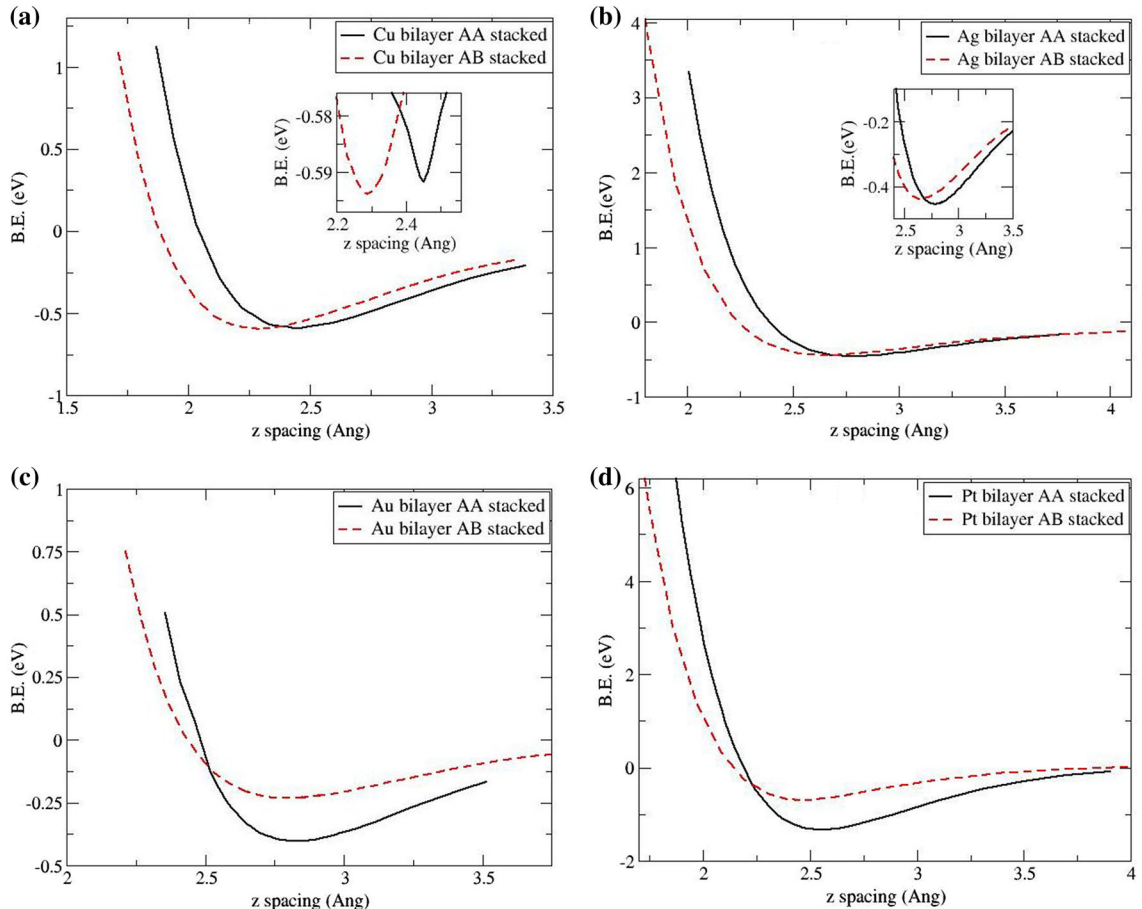


Fig. 2. Binding energy (eV) versus interlayer spacing (Å) curves for both AA- and AB-stacked bilayers of (a) Cu, (b) Ag, (c) Au, and (d) Pt.

considered here were taken with graphene-like hexagonal structure, as hcp is similar to a graphene-like structure in 2D (Fig. 1). The crystal structure taken for bulk phase was face-centered cubic (fcc), as the studied noble metals stabilize in fcc structure in bulk phase. Our calculated lattice parameters (Table I) for the bulk noble metals (Cu, Ag, Au, and Pt) (fcc structure) are consistent with values reported in literature.^{49,50} The lattice constants of the graphene-like hexagonal mono- and bilayers calculated at GGA-PBE level of theory were found to be almost constant (Table I).

Being similar to a graphene-like structure, the noble-metal bilayers can have two types of stacking pattern, namely AA and AB. In AA stacking, the metal atoms of the second layer lie exactly above the noble-metal atoms of the first layer, while in the case of AB stacking, the metal atoms of the second layer lie above interstitial sites of the first layer (Fig. 1). The relative stability of the bilayers in comparison with monolayers can be seen by calculating the binding energy of the bilayers according to the formula

$$\Delta E_b = E_{\text{bilayer}} - 2E_{\text{monolayer}}, \quad (2)$$

where E_{bilayer} and $E_{\text{monolayer}}$ are the minimum values of total energy of the bilayer and monolayer, respectively, obtained from total energy versus lattice constant plots. All values of ΔE_b are negative here, but we compare their magnitude only.

The curves of binding energy versus interlayer spacing suggest that Ag, Au, and Pt bilayers energetically favor AA stacking, while the Cu bilayer energetically prefers AB stacking (Fig. 2). The optimized vertical spacing between the layers was calculated to be 2.83 Å, 2.79 Å, 2.45 Å, and 2.55 Å for Cu, Ag, Au, and Pt, respectively (Table I). The calculated interlayer binding energies for the bilayers followed the order Pt > Cu > Ag > Au. The highest binding energy for the Pt bilayer is attributed to the partially filled both *s*- and *d*-orbitals.

To gain further insight into the interlayer interactions in the noble-metal bilayers, we calculated the charge density difference profiles (see Fig. S1 in the Supplementary Information; all charge density plots are at the same isosurface value of 0.0004 e/Å³). Note that the charge density difference is defined as $\Delta\rho = \rho_{\text{total}} - (\rho_{\text{layer1}} + \rho_{\text{layer2}})$. Red regions

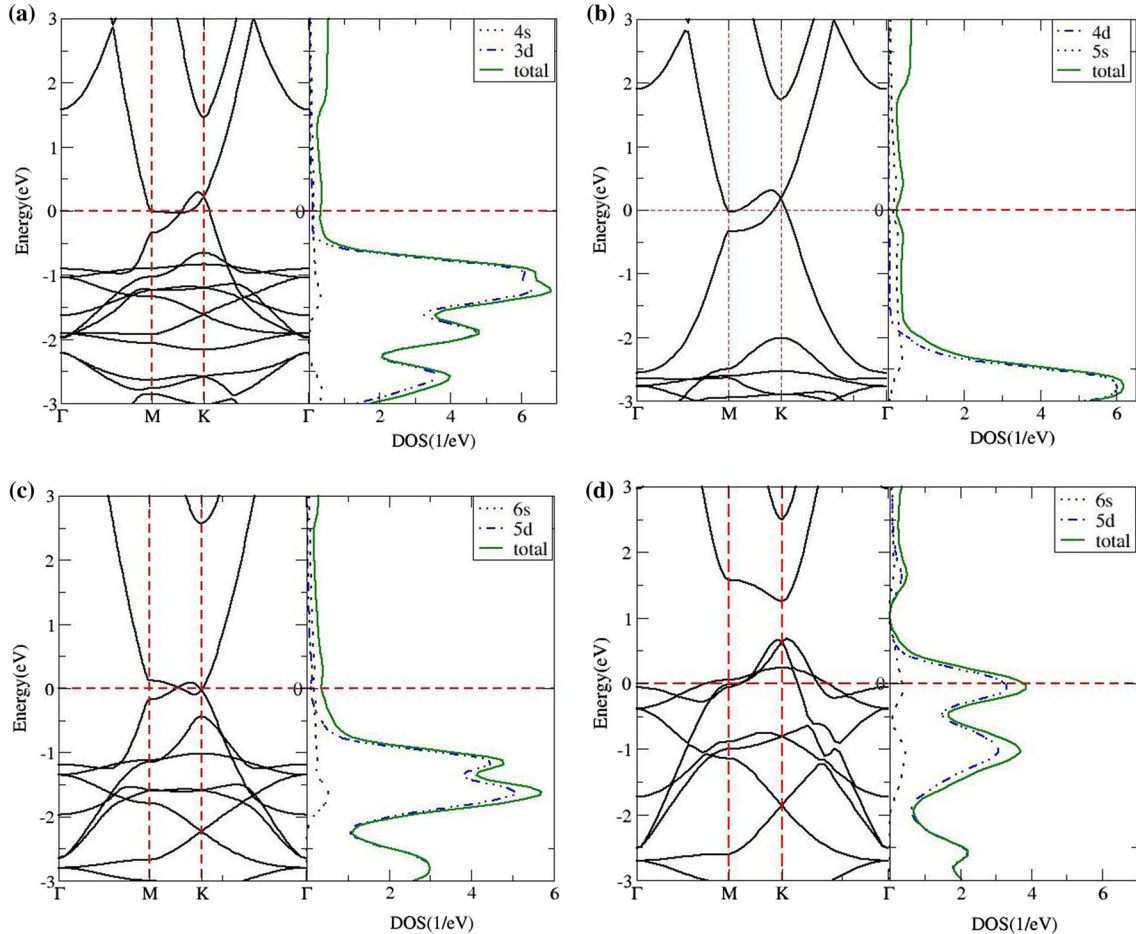


Fig. 3. Electronic band structure and corresponding density of states for monolayers of (a) Cu, (b) Ag, (c) Au, and (d) Pt. The Fermi level is set at 0 eV.

represent charge depletion, while green regions represent charge accumulation. The charge density difference plot indicates the redistribution of charge between the bonding regions of the two layers, which is more pronounced for Pt. The charge redistribution correlates well with the predicted order of interlayer binding energy, i.e., $Pt > Cu > Ag > Au$.

To further measure the covalent character of the bonds between atoms of the noble-metal layers, the covalency metric was calculated for all the systems and is given in Table I. The higher the value of the covalency metric, the more covalent the bond; for lower covalency, the charge distribution is enhanced. Further information and description of the concept of the covalency metric is given in the Supplementary Information and in Refs. 51 and 52. Density-of-states plots for all the systems, used to calculate the covalency, are also given in Fig. S2 in the Supplementary Information. The value of the covalency metric varied as follows: $Ag > Cu > Au > Pt$. This correlates well with our charge density difference plots, where charge redistribution was more pronounced for the Pt layers, which

are less covalent. Also, the Ag layers, which are more covalent, have less pronounced charge redistribution. It is inferred that the bilayers are more covalent in nature than the monolayers, except in the case of Ag.

Electronic Properties

The electronic band structure of the Cu, Ag, and Au mono- and bilayers showed similar behavior, while Pt was distinctly different (Figs. 3a–d and 4a–d). The graphene-like hexagonal monolayers of Cu, Ag, and Au showed increased quantum ballistic conductance (as obtained from the number of bands crossing the Fermi level) as compared with their bulk counterparts in fcc phase.

Note that the quantum ballistic conductance is calculated from the number of bands crossing the Fermi level.⁵³ The band structure of bulk Cu, Ag, and Au (see Fig. S4 in the Supplementary Information) shows two bands crossing the Fermi level, yielding conductance of $2G_0$, while in the corresponding monolayers, four bands cross the Fermi level, resulting in conductance of $4G_0$. The opposite

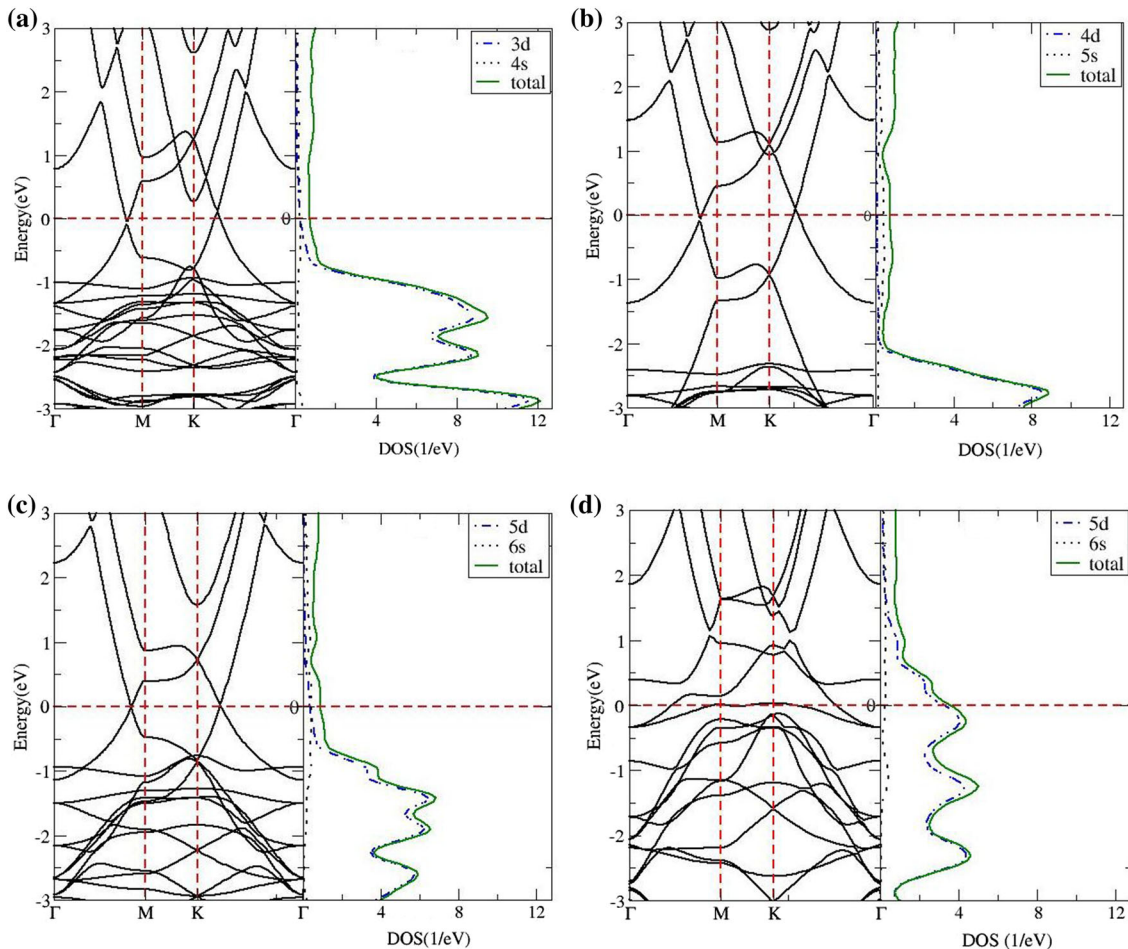


Fig. 4. Electronic band structure and corresponding density of states for bilayers of (a) Cu, (b) Ag, (c) Au, and (d) Pt. The Fermi level is set at 0 eV.

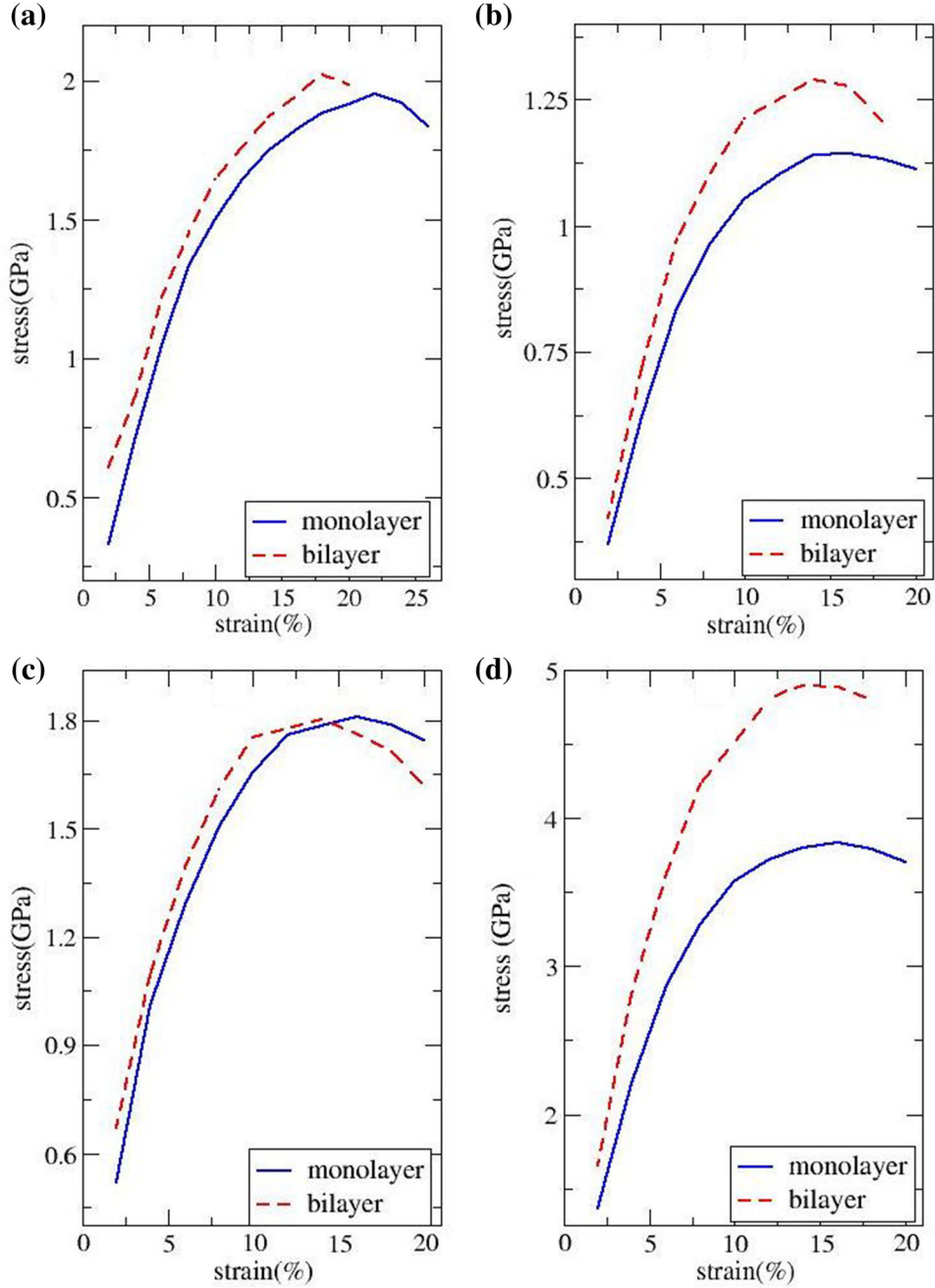


Fig. 5. Stress (GPa) versus tensile strain (%) (expansion) curve to determine the tensile strength of mono- and bilayers of (a) Cu, (b) Ag, (c) Au, and (d) Pt.

trend was observed for Pt, for which the quantum conductance decreases from $8G_0$ in bulk to $6G_0$ in the monolayer and bilayer. This is attributed to the different electronic arrangement of Pt. The value of G_0 , i.e., the quantized unit of conductance, is $2e^2/h = 7.748 \times 10^{-5}$ S.

Note that, in the case of Cu, Ag, and Au, the density of states in the valence band near the Fermi level is mainly contributed by d -orbitals, while the conduction band near the Fermi level is mainly contributed by s -orbital, showing Dirac-cone-like

behavior. In the case of the Pt layers, both s - and d -orbitals contribute near the Fermi level, and one observes a pronounced peak at the Fermi level, showing that the system is metallic in nature.

It is interesting to note that both the mono- and bilayers of Cu, Ag, and Au (Figs. 3 and 4) possess Dirac-cone-like (conical intersection) features. The monolayers show Dirac-cone-like behavior around the K high-symmetry point lying at the Fermi level (i.e., at 0 eV), while in the case of the bilayers, both the Γ and K high-symmetry points are found to

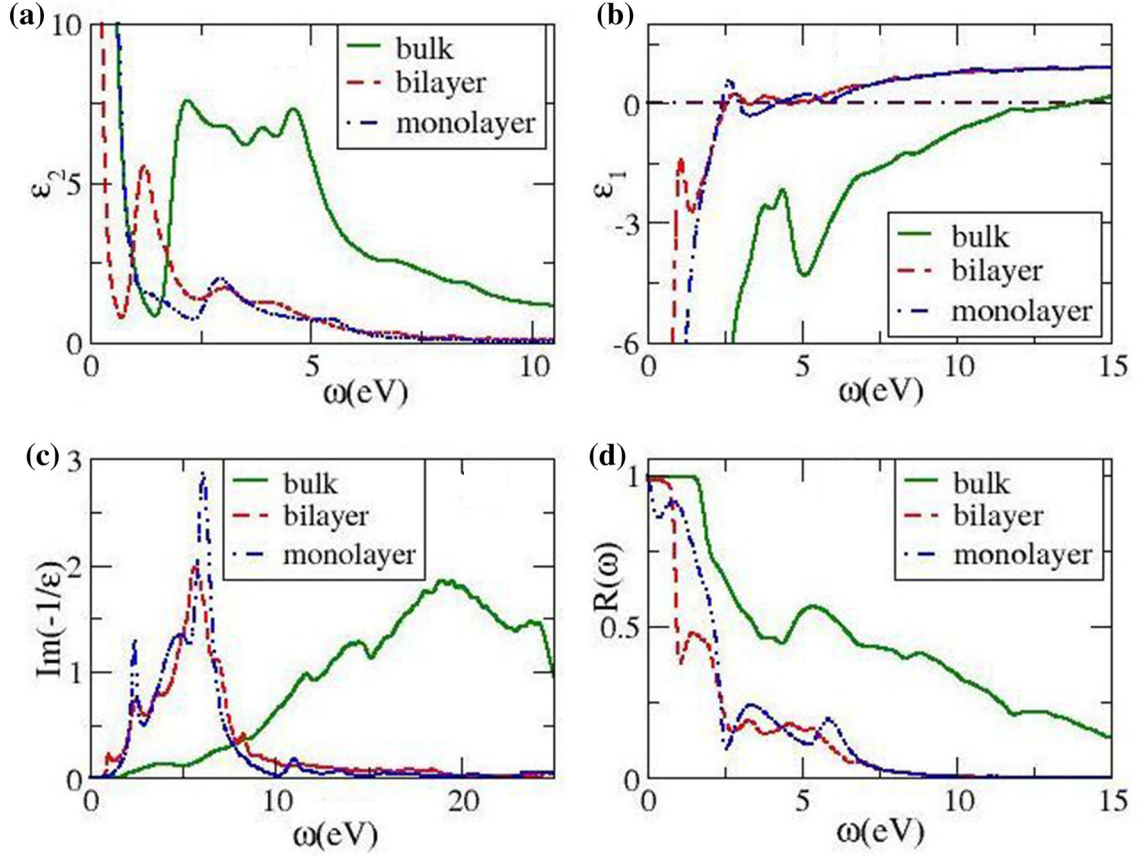


Fig. 6. (a) Imaginary part (ϵ_2) and (b) real part (ϵ_1) of dielectric function, (c) EELS spectrum, and (d) reflectance spectrum for Cu bulk, monolayer, and bilayer.

Table II. Calculated values of position of peak in ϵ_2 (S_0), plasmon frequency (ω_p), and reflectance edge [$R(\omega)$] for all studied noble-metal monolayers and bilayers and their bulk systems

Property	System	Cu	Ag	Au	Pt
S_0 (ϵ_2)	Bulk	2.23, 3.94, 4.65	3.52	2.85	6.56
	Monolayer	2.98	2.24	2.88, 4.99	1.18, 2.49, 4.403
	Bilayer	1.27	1.81	2.36, 4.98	1.072
ω_p (eV)	Bulk	11.71, 14.60, 19.02	3.09, 11.56, 22.61	2.41, 11.84, 22.42	5.90, 12.74, 23.57
	Monolayer	2.41, 6.21	3.02, 7.36	2.57, 7.53	2.16, 2.97, 5.09
	Bilayer	1.05, 2.61, 5.66	1.46, 3.36, 7.02	1.59, 2.00, 3.22, 7.45	3.38, 8.76, 10.38, 11.60
R (eV)	Bulk	1.71	2.83	1.89	5.53
	Monolayer	1.02	0.16	1.53	0.53
	Bilayer	0.73	1.32	0.75	0.11

possess the mentioned Dirac-cone-like feature, lying again at the Fermi level (i.e., at 0 eV). A recent investigation of Au/Ag multilayers using both angle-resolved photoemission spectroscopy (ARPES) and density functional theory (DFT) showed similar behavior,⁵⁴ where an anisotropic Dirac cone is observed between a particular pair of strongly spin-polarized deep d -orbital surface states. This interesting feature is likely to open up a new dimension for study and applications of these noble-metal mono- and bilayers.

Mechanical Properties

Mechanical strain has useful applications in nanoelectromechanical systems (NEMS) and nanooptomechanical systems (NOMS).⁵⁵ We calculated the stress that can be borne by the considered systems on application of biaxial strain. Biaxial strain was modeled by varying the lattice constant in both a and b directions. The stress varied directly with the strain up to some limit, then decreased (Fig. 5a–d). The region up to which it varied directly

is the elastic region, after which there is a plastic region, and ultimately the system deforms. The maximum value of strain up to which elasticity was retained provides the value of the ultimate tensile strain, and the corresponding stress value gives the ultimate tensile strength of the system.

The calculated ultimate tensile strength was 1.94 GPa, 1.14 GPa, 1.81 GPa, and 3.82 GPa for the Cu, Ag, Au, and Pt monolayers, respectively, while the bilayers showed slightly increased tensile strength values (Fig. 5). In the case of both monolayers and bilayers, Pt showed the highest tensile strength among the studied systems. The maximum tensile strain for the Cu mono- and bilayer was found to be 22% and 18%, respectively, while for the Ag, Au, and Pt monolayers it was 16%, and for their respective bilayers it was 14%.

The tensile strength of a material represents its capacity to withstand load or resist tension; the higher the tensile strength, the greater the capacity of a material to withstand tension. Hence, the Pt layers have higher load-withstanding capacity, followed by Cu, Au, and Ag; this trend is in agreement with the trend of tensile strength of these noble metals in bulk phase. This can be correlated with the interlayer binding energy, where greater binding energy of the system indicates stronger bonding and thus higher tensile strength.

Dielectric Properties

The calculated dielectric function for all the studied noble metal (Ag, Au, Cu, and Pt) bulks (fcc phase) agrees well with the dielectric function measured by Johnson et al.⁵⁶ and Yu et al.⁵⁷ Sharp peaks in the imaginary part of the dielectric function ϵ_2 for the studied noble metals suggest the possibility of interband transitions between bands in the band structure, corresponding to the energy values of these peaks. It was observed that peaks were red-shifted on moving from bulk in fcc phase to monolayers and bilayers taken with graphene-like hexagonal structure.

We observed sharp peaks in the imaginary part of the dielectric function ϵ_2 for bulk and bilayers of noble metals, but the monolayers showed low-valued broad peaks (except for Pt) (Figs. 6 and S5–S7 in the Supplementary Information). It was observed that the monolayer and bilayer of each of the noble metals exhibited very different ϵ_2 peak positions compared with the bulk counterparts (Table II), which may be attributed to the quantum confinement effect.⁵³

Plasmon Frequency

The plasmon frequency (ω_p) corresponds to the energy (eV) at the peak in the electronic energy loss spectrum (EELS) where the curve of the real part of the dielectric function (ϵ_1) crosses the zero axis. It was found that the plasmon frequency decreased (Table II) as one goes from the bulk to the 2D limit

of the noble metals Au, Ag, Cu, and Pt (Figs. 6 and S5–S7 in the Supplementary Information) due to the strong quantum confinement effect.⁵³

Reflectance Spectra

The reflectance spectrum for each of the studied noble-metal mono- and bilayers showed sharp minima corresponding to the point at which ϵ_1 cuts the zero axis and EELS shows a resonance peak. The value of the energy corresponding to this minimum point gives the value of the reflectance edge (Table II). For all the studied mono- and bilayers, the reflectance edge lay in the infrared (IR) region (0 eV to 1.65 eV). The reflectance edge for bulk Cu, Ag, and Au lies in the visible region (1.65 eV to 3.22 eV), whereas for bulk Pt, it lies in the ultraviolet (UV) region (3.22 eV to 12.4 eV) (Figs. 6 and S5–S7 in the Supplementary Information). Hence, the reflectance edge of the monolayers and bilayers of the studied noble metals is red-shifted towards the infrared (IR) region compared with the bulk counterparts. Such tunability of the reflectance spectrum and dielectric function of noble metals may find interesting applications in optoelectronics.

CONCLUSIONS

Electronic, mechanical, and dielectric properties of noble-metal (Au, Ag, Cu, and Pt) mono- and bilayers with graphene-like hexagonal structure were studied, revealing significant changes on going from bulk to monolayer, summarized as follows:

- The Au, Ag, and Pt bilayers stabilized in AA-stacked configuration, while the Cu bilayer preferred AB-stacked configuration.
- The value of the covalency metric varied as $\text{Ag} > \text{Cu} > \text{Au} > \text{Pt}$, consistent with our charge density plots. The bilayers are more covalent than the monolayers except for Ag.
- The quantum ballistic conductance increased as one moves from bulk in fcc phase to 2D graphene-like hexagonal noble-metal monolayers and bilayers (for Ag, Au, and Cu), which may be useful in the field of nanoelectronics.
- The monolayers and bilayers of Au, Ag, and Cu exhibited a Dirac-cone-like feature, while the Pt layers were metallic in nature. The Dirac-cone-like feature obtained for the Au, Ag, and Cu atomic layers will open up new scope for their study and applications. The realization of a Dirac cone shows promise for applications of the studied noble-metal mono- and bilayers in spintronic devices and nanodevices. Further investigation of the behavior of this Dirac-cone-like feature could include functionalization of these noble-metal layers.⁵⁸
- The Pt layers (both monolayer and bilayer) showed the highest tensile strength among the studied systems.
- The monolayers and bilayers of the studied noble metals showed distinctly different positions of

the structure peaks in ϵ_2 compared with the bulk counterparts, due to the quantum confinement effect.

- The plasmon frequency was red-shifted in energy on going from the bulk fcc structure to the graphene-like hexagonal monolayer for all the noble metals.
- The reflectance edges of the graphene-like noble-metal mono- and bilayers were found in the infrared (IR) region, in contrast to the visible-ultraviolet (UV) region for their bulk fcc counterparts, due to which they show reflectance in the infrared (IR) region and become transparent conductors in the visible region, and hence may find huge applications in optoelectronics.⁴⁹

These atomic layers of noble metals can be used as stretchable electrodes for organic-based electronic devices,³⁴ displays,³⁵ field-effect transistors (FETs),³⁶ and energy-related devices,³⁷ as well as being useful for tuning surface-enhanced Raman spectroscopy (SERS), metal-enhanced fluorescence, and as scanning tunneling microscopy (STM) substrates.⁶

ACKNOWLEDGEMENTS

P.K. wishes to acknowledge financial support from the University Grants Commission (UGC), New Delhi in the form of a University Grants Commission Basic Sciences Research (UGC-BSR) Junior Research Fellowship (JRF). The authors would like to acknowledge the SIESTA team for the code. All calculations were carried out on the High Performance Computing Cluster (HPCC) in the Physics Department at H.P. University, provided by the Department of Science & Technology, Government of India under the Funds for the Improvement of Science & Technology (FIST) programme.

ELECTRONIC SUPPLEMENTARY MATERIAL

The online version of this article (doi: [10.1007/s11664-016-4864-z](https://doi.org/10.1007/s11664-016-4864-z)) contains supplementary material, which is available to authorized users.

REFERENCES

1. C.H. Liu, W.W. Wu, and L.J. Chen, *J. Electron. Mater.* 35, 1 (2006).
2. D.B. Janes, T. Lee, J. Liu, M. Batistuta, N.-P. Chen, B.L. Walsh, R.P. Andres, E.-H. Chen, M.R. Melloch, J.M. Woodall, and R. Reifenger, *J. Electron. Mater.* 29, 565 (2000).
3. H.L. Liu, F. Nosheen, and X. Wang, *Chem. Soc. Rev.* 44, 3056 (2015).
4. X. Hong, C. Tan, J. Chen, Z. Xu, and H. Zhang, *Nano Res.* 8, 40 (2015).
5. D.L. Feldheim and C. Foss, *J. Am. Chem. Soc.* 124, 7874 (2002).
6. H. Chen, F. Simon, and A. Eychmuller, *J. Phys. Chem. C* 114, 4495 (2010).
7. C.J. Murphy, T.K. Sau, A.M. Gole, C.J. Orendorff, J. Gao, L. Gou, S.E. Hunyadi, and T. Li, *Phys. Chem. B* 109, 13857 (2005).
8. H.Y. Wu, H. Chu, T. Kuo, C. Kuo, and M.H. Huang, *Chem. Mater.* 17, 6447 (2005).
9. L. Lu, A. Kobayashi, K. Tawa, and Y. Ozaki, *Chem. Mater.* 18, 4894 (2006).
10. Y. Wang, X. Zou, W. Ren, W. Wang, and E. Wang, *J. Phys. Chem. C* 111, 3259 (2007).
11. A. Gentile, F. Ruffino, C. D'Andrea, P.G. Gucciardi, R. Reitano, and M.G. Grimaldi, *J. Electron. Mater.* 45, 2815 (2016).
12. L.M. Quynh, N.H. Nam, K. Kong, N.T. Nhung, I. Nottingher, M. Henini, and N.H. Luong, *J. Electron. Mater.* 45, 2563 (2016).
13. S. Eustis and M.A. El-Sayed, *Chem. Soc. Rev.* 35, 209 (2006).
14. E. Ozbay, *Science* 311, 189 (2006).
15. P.K. Jain, X. Huang, I.H. El-Sayed, and M.A. El-Sayed, *Acc. Chem. Res.* 41, 1578 (2008).
16. S.E. Skrabalak, J. Chen, Y. Sun, X. Lu, L. Au, C.M. Cobley, and Y. Xia, *Acc. Chem. Res.* 41, 1587 (2008).
17. Y. Ma, J. Lin, S. Qin, L. Zhu, B. Li, and S. Lei, *J. Electron. Mater.* 41, 646 (2012).
18. J.A. Jimenez, *J. Electron. Mater.* 44, 4418 (2015).
19. A.K. Geim and K.S. Novoselov, *Nat. Mater.* 6, 183 (2007).
20. F. Geng, R. Ma, A. Nakamura, K. Akatsuka, Y. Ebina, Y. Yamauchi, N. Miyamoto, Y. Tateyama, and T. Sasaki, *Nat. Commun.* 4, 1632:1 (2013).
21. L.M. Molina and B. Hammer, *Appl. Catal.* 291, 21 (2005).
22. C. Li, W. Cai, B. Cao, F. Sun, Y. Li, C. Kan, and L. Zhang, *Adv. Funct. Mater.* 16, 83 (2006).
23. N. Krasteva, I. Besnard, B. Guse, R.E. Bauer, K. Mullen, A. Yasuda, and T. Vossmeier, *Nano Lett.* 2, 551 (2002).
24. M.T. Do, Q.C. Tong, M.H. Luong, A. Lidiak, I.L. Rak, and N.D. Lai, *J. Electron. Mater.* 45, 2347 (2016).
25. S.-J. Hsu and I.J.B. Lin, *J. Chin. Chem. Soc.* 56, 98 (2009).
26. M.C. Daniel and D. Astruc, *Chem. Rev.* 104, 293 (2004).
27. J. Hu, Z. Wang, and J. Li, *Sensors* 7, 3299 (2007).
28. A. Sanyal and M. Sastry, *Chem. Commun.* 11, 1236 (2003).
29. S. Onoue, J. He, and T. Kunitake, *Chem. Lett.* 35, 214 (2006).
30. Z. Wang, J. Yuan, M. Zhou, L. Niu, and A. Ivaska, *Appl. Surf. Sci.* 254, 6289 (2008).
31. T.S. Selvam, C.M. Chiang, and M. Chi, *J. Nanopart. Res.* 13, 3275 (2011).
32. T. Soejima and N. Kimizuka, *Chem. Soc. Jpn.* 34, 1234 (2005).
33. X. Huang, S. Li, Y. Huang, S. Wu, X. Zhou, S. Li, C.L. Gan, F. Boey, C.A. Mirkin, and H. Zhang, *Nat. Commun.* 2, 292 (2011).
34. G.D. Moon, G.-H. Lim, J.H. Song, M. Shin, T. Yu, B. Lim, and U. Jeong, *Adv. Mater.* 25, 2707 (2013).
35. S.I. Park, Y. Xiong, R.-H. Kim, P. Elvikis, M. Meit, D.-H. Kim, J. Wu, J. Yoon, C.-J. Yu, Z. Liu, Y. Huang, K. Hwang, P. Ferreira, X. Li, K. Choquette, and J.A. Rogers, *Science* 325, 977 (2009).
36. D.-Y. Khang, H. Jiang, Y. Huang, and J.A. Rogers, *Science* 311, 208 (2006).
37. D.J. Lipomi, B.C. Tee, M. Vosgueritchian, and Z. Bao, *Adv. Mater.* 23, 1771 (2011).
38. S.H. Park, J.G. Son, T.G. Lee, H.M. Park, and J.Y. Song, *Nanoscale Res. Lett.* 8, 248 (2013).
39. A. Funatsu, H. Tateishi, K. Hatakeyama, Y. Fukunaga, T. Taniguchi, M. Koinuma, H. Matsuura, and Y. Matsumoto, *Chem. Commun.* 50, 8503 (2014).
40. R. Dang, L. Song, W. Dong, C. Li, X. Zhang, and G. Wang, *ACS Appl. Mater. Interfaces* 6, 622 (2014).
41. J.M. Soler, E. Artacho, J.D. Gale, A. Garcia, J. Junquera, P. Ordejon, and D.S. Portal, *J. Phys.: Condens. Matter* 14, 2745 (2002).
42. A. Kumar, D. Banyai, P.K. Ahluwalia, R. Pandey, and S.P. Karna, *Phys. Chem. Chem. Phys.* 16, 20157 (2014).

43. N. Troullier and J.L. Martins, *Phys. Rev. B* 43, 1993 (1991).
44. N. Troullier and J.L. Martins, *Phys. Rev. B* 43, 8861 (1991).
45. J.P. Perdew, K. Burke, and M. Ernzerhof, *Phys. Rev. Lett.* 77, 3865 (1996).
46. J. Moreno and J.M. Soler, *Phys. Rev. B* 45, 13891 (1992).
47. F. Knider, J. Hugel, and A.V. Postnikov, *J. Phys.: Condens. Matter* 19, 196105 (2007).
48. E.G. Maksimov, I.I. Mazin, S.N. Rashkeev, et al., *J. Phys. F. Met. Phys.* 18, 833 (1988).
49. A. Kumar, A. Kumar, and P.K. Ahluwalia, *Phys. E* 46, 259 (2012).
50. C. Kittel, *Introduction to Solid State Physics* (New York: Wiley Eastern Limited Reprint, 1988).
51. A. Cammarata and J.M. Rondinelli, *J. Chem. Phys.* 141, 114704 (2014).
52. A. Cammarata and T. Polcar, *Inorg. Chem.* 54, 5739 (2015).
53. B.K. Agrawal, V. Singh, R. Srivastava, and S. Agrawal, *Phys. Rev. B* 74, 245405(1) (2006).
54. R. Requist, P.M. Sheverdyeva, P. Moras, S.K. Mahatha, C. Carbone, and E. Tosatti, *Phys. Rev. B* 91, 045432-1 (2015).
55. A. Kumar and P.K. Ahluwalia, *Phys. B* 419, 66 (2013).
56. P.B. Johnson and R.W. Christy, *Phys. Rev. B* 6, 4370 (1972).
57. A.Y.-C. Yu and W.E. Spicer, *Phys. Rev.* 171, 834 (1968).
58. H. Pan and X.-S. Wang, *Nanoscale Res. Lett.* 10, 334 (2015).



Alloyed monolayers of Cu, Ag, Au and Pt in hexagonal phase: A comprehensive first principles study

Pooja Kapoor^{a,*}, Arun Kumar^b, Munish Sharma^a, Jagdish Kumar^c, Ashok Kumar^d, P.K. Ahluwalia^{a,*}

^a Department of Physics, Himachal Pradesh University, Shimla, Himachal Pradesh, India

^b Department of Physics, Swami Vivekananda Govt College, Ghumarwin, Bilaspur, Himachal Pradesh, India

^c Department of Physics and Astronomical Science, Central University of Himachal Pradesh, Dharamshala, Himachal Pradesh, India

^d Department of Physical Sciences, School of Basic and Applied Sciences, Central University of Punjab, Bathinda, Punjab, India,

ARTICLE INFO

Keywords:

DFT
Monolayers
Band structure
Mechanical properties
STM images
NDR region

ABSTRACT

We present density functional theory (DFT) based comprehensive study of two-dimensional (2D) alloyed monolayers of noble metals (AgCu, AgPt, AgAu, AuCu, AuPt and CuPt) in hexagonal phase within numerical atomic orbitals and plane wave basis sets methods. The monolayers considered exhibit positive phonon frequencies suggesting them to be dynamically stable. The Pt containing alloyed monolayers have superior structural stability (binding energy and tensile strength) and exhibit metallic and ferromagnetic character amongst all the alloyed monolayers. Interestingly, alloying of Au monolayer with Cu and Ag show semi-conducting behavior whereas alloyed AgCu monolayer possesses Dirac-cone like features at high symmetry points. These distinct features in electronic structures of alloyed 2D monolayers have been captured in STM like set up. An anisotropic behavior has been observed in dielectric spectra for all the considered structures. Tunneling characteristics show NDR region for Pt containing alloyed monolayers. The considered alloyed monolayers may potentially be useful as a building blocks for the applications in nano- and opto-electronics.

1. Introduction

Two-dimensional (2D) form of noble-metals with thickness in few nanometer range, possesses unique physical [1] and chemical properties [2]. These have numerous technological applications such as in catalysis, micro electromechanical and nano-electromechanical systems, as interconnects in molecular circuits, sensors, devices for surface enhanced Raman spectroscopy, as protective coatings and biomedical area [3–6]. Noble-metal nanostructures are reported to be synthesized in different polymorphs such as triangular, hexagonal and helical structures as compared to FCC structure in their bulk counterpart [7]. It is known that the properties of metal nanostructures are closely related to their crystal structure [8,9]. Noble metals exhibit various crystal structures in the bulk form, for example, Ag possesses two different polymorphs 9R- [10] and 4H-polytype [11]. The occurrence of hexagonal phase in one-dimensional (1D) hetero-nanostructures [12], thin films [13], nanorods [14–17], and nanowires of Silver has been reported in previous studies [18,19].

A crystallization pathway for metastable HCP phase in gold has recently been reported by Marshall et al. [20]. In last decade it has also

been possible to synthesize Gold in various nanostructures such as nanoparticles [21], nanowires [22], nanobelts or nanoribbons [23,24], nanoplates [6] nanosheets [25] and nanotubes [26] with HCP structure. This occurrence of nanostructures of Gold in HCP structure makes understanding of their properties interesting from basic research as well as technological point of view.

Despite wide applications of noble metal nanoplates and nanosheets, their use is limited due to their scarce reserves and high costs. Alloying of noble metals with earth abundant metals has enhanced their properties in a cost effective manner [27]. Alloyed nanomaterials in which d-band vacancies of a Group 8 and 10 (Fe, Pt) metal are progressively filled by a Group 11 (Au, Ag and Cu) metal have attracted wide interest for its application in the field of electronics [28–31]. Note that the heterogeneous Au–Pt [32,33], Au–Ag [34] and Au–Cu [35] nanostructures with much better properties than their pristine counterparts have been synthesized for applications in various fields like optics, electronics, protective coatings, bio-sensing, drug delivery and catalysis [6,30–35].

Though hexagonal structure is not an obvious choice for noble metal alloyed sheets, but motivated by the above mentioned recent reports,

* Corresponding authors.

E-mail addresses: pupooja16@gmail.com (P. Kapoor), pk_ahluwalia7@yahoo.com (P.K. Ahluwalia).

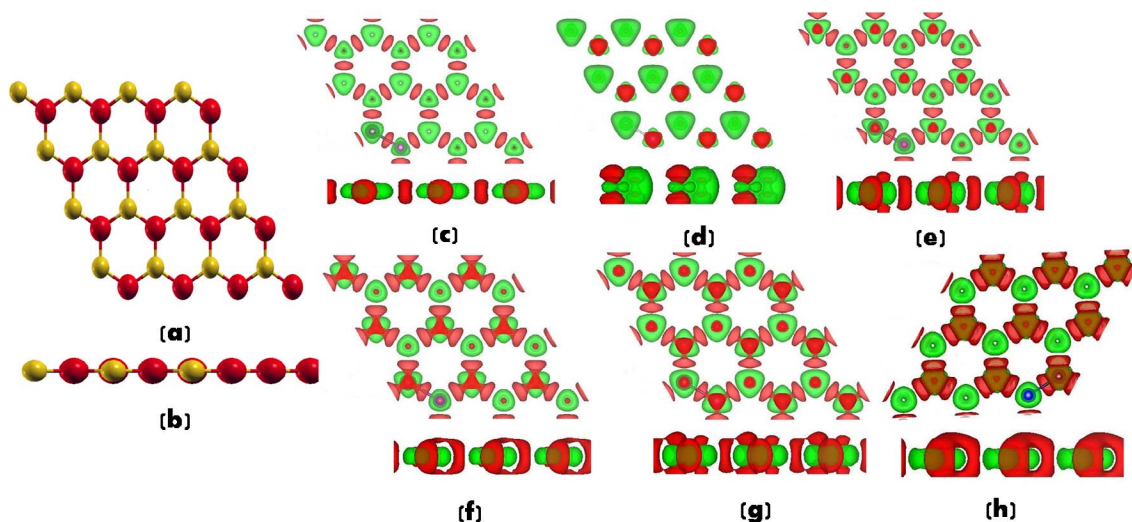


Fig. 1. (a) Top and (b) side view of Crystal structure of one of the studied alloyed monolayers and Top and side view of charge density profiles of all studied systems (c) AgCu, (d) AgPt, (e) CuPt, (f) AuCu, (g) AuPt and (h) AuAg respectively at an isosurface value of $0.004 \text{ e}/\text{\AA}^3$. Here red/green regions show charge accumulation/depletion. (For interpretation of the references to colour in this figure legend, the reader is referred to the web version of this article.)

and in search of new low cost materials with enhanced properties, we present a DFT-based computational study of alloyed monolayers in hexagonal phase. Our hexagonal monolayers are structurally similar to h-BN monolayer grown on Cu foil [36], where two adjacent edges of h-BN layer are boron terminated and other two are nitrogen terminated. Similarly in our case two adjacent edges are terminated by two different noble-metal, thereby, forming an alloyed noble-metal monolayer (Fig. 1). In order to have faith in our results, we have performed DFT based calculations using two different approaches i.e. localized orbital basis approach as implemented in *SIESTA* (Spanish Initiative for Electronic Simulation with Thousand of Atoms) and Plane wave basis approach in *VASP* (Vienna Ab initio Simulation Package). As a result, a comprehensive DFT based comparative study of structural, electronic, magnetic, mechanical and dielectric properties of noble-metal alloyed monolayers is presented. The phonon frequencies at high symmetry points are calculated to check the dynamical stability of the studied systems. To visualize the distinct electronic band structure features of alloyed monolayers, STM analysis is also presented. Here the word *alloy* is being used merely for ease of expression and not be taken in strict sense.

2. Computational details

The computational details for two DFT based first principle approaches, *SIESTA* [37] and *VASP* [38,39] for the study are as follows:

For *SIESTA*, we have used well tested [40,41] Troullier Martin, norm conserving relativistic pseudopotentials [42,43] in fully separable Kleinman and Bylander form. For *VASP*, pseudopotentials used were based on projected augmented wave (PAW) method [44]. The exchange and correlation energies were treated within the generalized gradient approximation (GGA) according to the Perdew-Burke-Ernzerhof (PBE) parameterization for both codes [45]. In *SIESTA*, numerical atomic orbitals (NAOs) with double zeta polarization (DZP) basis set with confinement energy of 30 meV have been used for geometry optimization. Minimization of energy has been carried out using standard conjugate-gradients (CG) technique for both codes until the forces on each atom were less than $0.01 \text{ eV}/\text{\AA}$. A Monkhorst-Pack [46] of $50 \times 50 \times 1 \text{ k}$ points has been used for sampling the Brillouin zone for both codes. The mesh cutoff energy has been taken equal to 350 Ry in *SIESTA* and corresponding plane wave cutoff energy in *VASP* was taken equal to 400 eV. A unit cell of two atoms, one atom each of the two noble-metals forming the alloy and a vacuum of 16 \AA along c axis to avoid interactions between periodic images, were taken for the

calculations.

The dielectric properties have been calculated by using first-order time-dependent perturbation theory as implemented in *SIESTA code* [47,48]. A $90 \times 90 \times 3$ optical mesh and 0.04 eV optical broadening are used for optical spectra. It is necessary to include a Drude term associated with intra-band transitions in case of metals, for which the values of τ for all studied systems is taken as 0.001 Ha [40,41]. The dielectric properties in *VASP* were calculated using perturbation theory with local field effects using random phase approximation.

We have also calculated the phonon frequencies using *VASP code*. In addition, tunneling characteristics are calculated within Tersoff and Hamann approximation [49] using STM-like setup. According to this approximation, tunneling current (I) is proportional to the local density of states (LDOS) of the sample. Local Density of states and atomic positions of monolayer samples are obtained from *VASP code*. For STM analysis, the STM tip was taken of silicon cluster and bias voltage of $\pm 0.5 \text{ V}$ is applied between the STM tip and the sample. STM images are obtained using *WsxM software* [50] which uses LDOS of *SIESTA* as input.

3. Results and discussion

3.1. Structural properties

Table 1 lists the calculated values of lattice constant, bond length and binding energies of the studied systems. Note that the structural properties of pristine noble metal monolayers are reported in our previous study [40].

The values of lattice constant for these studied alloyed monolayers

Table 1
The comparison of values of lattice constant, bond length and binding energies for alloyed monolayers. The values in bracket are obtained from *VASP code*.

Property	AgCu	AuCu	AuAg	AuPt	AgPt	CuPt
Lattice constant (\AA)	4.34 (4.27)	4.33 (4.21)	4.69 (4.58)	4.47 (4.35)	4.53 (4.41)	4.19 (4.08)
Bond length (\AA)	2.53 (2.45)	2.50 (2.42)	2.64 (2.64)	2.55 (2.50)	2.57 (2.54)	2.37 (2.35)
Binding energy (eV)	-2.38 (-2.24)	-2.57 (-2.68)	-2.22 (-2.29)	-3.17 (-3.13)	-2.86 (-2.68)	-3.36 (-3.24)

(Table 1) are lying within the range of their pristine counterparts [40]. The lattice constant varies in the following order AuAg > AgPt > AuPt > AgCu > AuCu > CuPt. The values of bond length (Table 1) are smaller than the average value of their pristine systems (Table S1) which favors the formation of these alloyed monolayers [41]. The value of lattice constant and bond lengths of the studied systems from both SIESTA and VASP calculations are found to be close to each other with a difference (Table 1) of about 2–3%.

The negative value of binding energy (Table 1) in each case suggests that all systems are energetically stable. The value of binding energies of alloyed systems is found to be more than the average value of their (Table S1) pristine counterparts, showing that the alloyed monolayer are more stable than their pristine counterparts and alloy formation is favored. The binding energies follow the trend CuPt > AuPt > AgPt > AuCu > AgCu > AuAg from both SIESTA and VASP calculations. Note that (Table 1) the values obtained from two codes differ by about 6%. It is noted here that amongst the studied alloyed monolayers, the Pt containing systems (e.g. CuPt monolayer) are energetically more stable.

In order to gain an insight into the inter-atomic interactions in noble metal alloyed monolayers, we have calculated the charge density difference profile (Fig. 1). The charge density difference is defined as $\Delta\rho = \rho_{total} - (\rho_{atom1} + \rho_{atom2})$. Charge density difference plot indicates the redistribution of charge between the atoms of different noble-metals. The redistribution is more pronounced for AuCu, CuPt and AuPt as compared to other systems. These results are in agreement with Mulliken charge transfer values given in Table S2 (Supplementary information). These charge transfer mechanisms between the atoms of different species can be explained on the basis of their electronegativities [51]. The higher electronegative atom gains charge while lesser electronegative atom loses charge. From Table S2 it is clear that amongst the chosen systems, AuPt monolayer has the highest charge transfer and AgPt monolayer has the least charge transfer.

3.2. Phonon dispersion spectra for alloyed monolayers

In order to check the dynamical stability of systems considered, we have calculated the phonon frequencies at high symmetry points Γ , 'M' and 'K', using VASP code. Two atoms in the unit cell of given systems results in six phonon frequencies, out of which three correspond to acoustic (A) modes and three are optical (O) modes. These modes are associated with out-of-plane (Z), in-plane longitudinal (L), and in-plane transverse (T) symmetries. The lower phonon frequencies correspond to the acoustic mode and higher to the optical mode. The phonon frequencies are given in Table 2 and are found to be positive for all modes at all high symmetry points, which suggests all studied alloyed monolayers to be dynamically stable.

3.3. Mechanical properties

Strain plays an important role when a crystal is compressed or stretched from its equilibrium position. It can affect the device performance and can be applied intentionally to improve device's applications

Table 2

The value of phonon frequencies at Γ , M and K high symmetry points for all studied alloyed monolayers.

System	Phonon Frequencies (in cm^{-1})		
	at Γ	at M	at K
AgCu	219.576, 219.07, 52.675, 7.85, 1.02, 0.87	217.465, 167.32, 117.675, 63.94, 6.32, 2.836	182.49, 180.764, 158.067, 9.888, 4.944, 4.065
AgPt	172.16, 166.48, 75.95, 8.466, 0.494, 0.0054	229.123, 223.125, 94.193, 16.022, 8.271, 0.025	150.14, 109.32, 87.167, 8.964, 0.594, 0.35
CuPt	174.136, 148.75, 28.304, 9.85, 1.86, 0.606	257.464, 109.97, 108.61, 106.85, 10.315, 4.356	217.84, 93.47, 19.58, 18.71, 5.54, 5.20
AuPt	108.63, 92.403, 88.15, 10.52, 2.96, 0.446	283.88, 213.594, 87.267, 51.77, 27.145, 0.0425	270.063, 265.207, 153.60, 6.07, 3.87, 3.157
AuCu	239.25, 238.84, 50.661, 24.167, 1.0012, 0.901	242.41, 222.766, 115.97, 50.12, 11.22, 0.1515	166.50, 89.08, 85.214, 17.027, 10.204, 8.337
AuAg	164.03, 164.0, 55.43, 9.164, 0.172, 0.099,	84.64, 83.75, 113.704, 9.664, 2.19, 1.702	176.044, 116.493, 84.3, 11.34, 9.20, 0.512,

in NEMS (nano electro-mechanical systems) and NOMS (nano opto-mechanical systems). We have applied the biaxial tensile strain which can be modeled by varying the lattice constant in both 'a' and 'b' directions simultaneously, and the corresponding stress tensor values can be obtained. Stress varies directly with strain up to some limit and then decreases [(Fig. 2) for AgCu, AuAg and AuPt systems and Fig. S1 of Supplementary information for AuCu, CuPt and AgPt systems].

The maximum value of strain up to which stress varies directly with strain, gives the value of ultimate tensile strain and corresponding value of stress gives the ultimate tensile strength of the system. The tensile strength of a system is simply the ability of a system to withstand load. The values of ultimate tensile strain and strength for all studied systems as obtained from both codes SIESTA and VASP are given in Table 3 for the comparison.

It is noted that the values of tensile strength of alloyed monolayer lies within the range of its pristine counterparts [40]. In case of Pt containing systems, the tensile strength is less than pristine Pt monolayer and more than other constituent atom of alloyed monolayer. Amongst the studied systems, CuPt has the highest tensile strength that varies as CuPt > AuPt > AuCu > AgPt > AgCu > AuAg. This trends is attributed to the stronger bonding as reflected by binding energies of the studied systems.

3.4. Electronic and magnetic properties

To understand the electronic properties of alloyed monolayers, electronic band structure and corresponding spin polarized total and partial density of states as a function of energy have been plotted and are shown in Fig. 3 for AgCu, AuAg, AuCu and CuPt monolayer and Fig. S2 (Supplementary information) for AuPt and CuPt monolayer. The band structures obtained from SIESTA and VASP calculations are found to be similar [(Fig. S3) of Supplementary information]. The electronic band structures for various systems under study have been calculated along the Γ -M-K- Γ direction of the Brillouin zone. From the electronic band structure, it is observed that all Pt containing alloyed monolayers (AuPt, AgPt and CuPt) are metallic in nature and their features are quite similar to the electronic band structure of pristine Pt monolayer reported in previous study [40].

The Au containing alloyed monolayers (AuCu and AuAg) are semiconducting in nature. An indirect band gap of 0.46 eV is calculated for AuCu monolayer which lies between M and K high symmetry point of Brillouin zone. AuAg monolayer, shows a direct band gap of 0.88 eV at M high symmetry point. The values of band-gaps from VASP and SIESTA calculations differ by a small amount of less than 2% [(Table S3) of Supplementary information]. A similar behavior is also observed for the alloyed nanowires of these noble metals in previous studies [41]. In AgCu monolayer, two conical intersections (Dirac-cone like behavior) crossing the Fermi-level, one from the conduction band at high symmetry point M and other from the valence band at high symmetry point K are observed. AgCu monolayer shows similar behavior as seen in band structures of pristine Ag and Cu monolayers [40].

In order to have a deeper insight into the contribution of different orbitals of an atom in the band formation, we have analyzed the partial

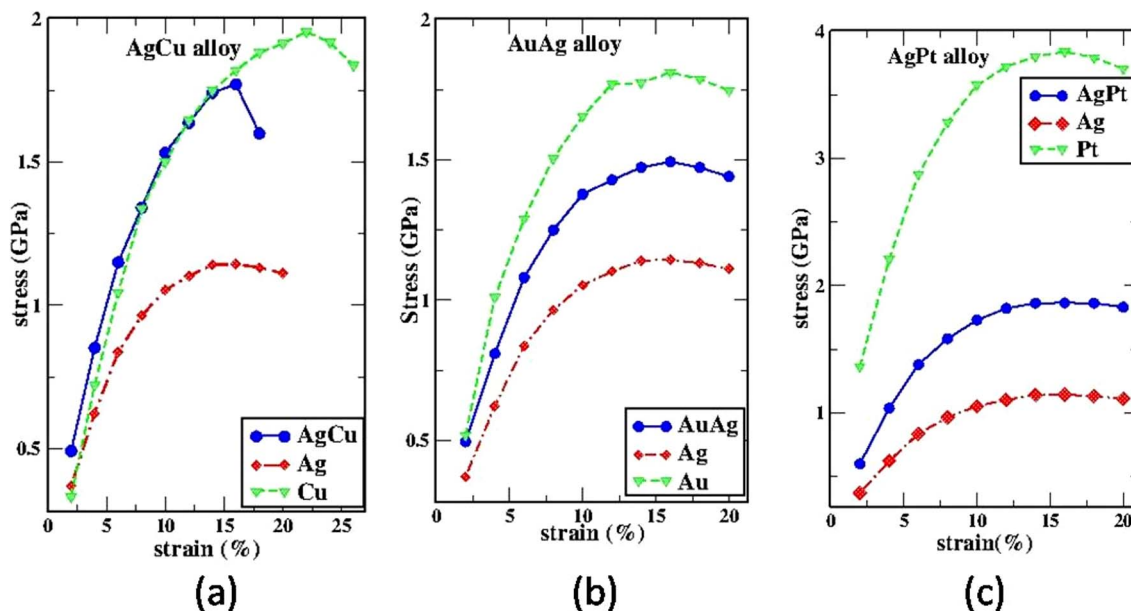


Fig. 2. Stress-strain curves to determine the ultimate tensile strength for the alloyed monolayers (a) AgCu, (b) AuAg and (c) AgPt respectively where strain is in (%) and stress is in (GPa).

Table 3

The values of magnetic moment (μ_b), tensile strength, and tensile strain in case alloyed monolayers. The values given in bracket are the values obtained from VASP calculations for comparison.

Property	AgCu	AuCu	AuAg	AuPt	AgPt	CuPt
Magnetic moment (μ_b)	0.00 (0.0)	0.00 (0.0)	0.00 (0.0)	0.58 (0.57)	0.41 (0.36)	0.45 (0.51)
Tensile strength (GPa)	1.77 (1.46)	1.97 (2.32)	1.49 (1.35)	2.49 (2.52)	1.86 (1.81)	2.64 (2.62)
Tensile strain (%)	16 (14)	16 (14)	16 (14)	14 (14)	16 (14)	20 (14)

density of state plots (Figs. 3 and S2) of the studied systems. In the density of states plots of all Pt containing alloyed monolayers (AuPt, AgPt and CuPt), a major contribution to the density of states is due to Pt 5d orbitals near the Fermi-level. In case of Cu containing alloyed monolayers (AuCu and AgCu), Cu 3d orbitals show a major contribution to the density of states at the Fermi-level. In AuAg system, 5d orbitals of Au give a major contribution to the density of states near the Fermi-level.

The quantum ballistic conductance of a system under ideal situation can be determined by the number of bands crossing the Fermi-level (E_f) [52]. For each band crossing the Fermi-level (E_f), the ballistic conductance is G_0 which results into a conductance of nG_0 for n number of bands crossing the Fermi-level. The calculated quantum ballistic conductance is $4G_0$ for AgPt, CuPt and AgCu systems while $6G_0$ for AuPt monolayer. The conductance is zero for AuAg and AuCu as these systems are found to be semiconducting in nature with no band crossing the Fermi-level.

The alloyed monolayers containing Pt (AgPt, AuPt and CuPt) are found to be magnetic in nature as is clear from their density of states plots [(Fig. 3(d)) for CuPt and Fig. S2 of Supplementary information for AuPt and AgPt]. The spin up and spin down states are different in magnitude, with spin up states showing a major contribution, that favors ferromagnetism. The major contribution to ferromagnetism comes from the d-orbitals and particularly from the Pt 5d orbitals. All other studied systems are non-magnetic, with both spin up and spin down density of states having equal magnitude resulting in no net magnetic moment. The **Stoner criterion** is a condition to be fulfilled for the ferromagnetic order to arise in a solid. According to Stoner criterion,

ferromagnetism can arise in a system if:

$$I \times N_{E_f} \geq 1$$

which is getting fulfilled for our Pt containing systems. Here I is the stoner parameter whose value is 0.63 eV for Pt [53] and N_{E_f} is the non-magnetic density of states of major contributing orbital (Pt 5d orbitals here) at the Fermi-level. The values of Stoner criterion (IN_{E_f}) are given in Table S4.

We have also calculated the magnetic moment as given in Table 3 ($\mu_b = Q_{\uparrow} - Q_{\downarrow}$), where Q_{\uparrow} is the Mulliken charge population for the spin up and Q_{\downarrow} is the Mulliken charge population for the spin down states) showing clearly the presence of ferromagnetism. The magnetic moments have also been calculated with VASP code and show a similar trend with a difference of about 2% in case of AuPt and 12% in case of AgPt and CuPt.

3.5. STM analysis

The distinct features in electronic band structure of alloyed monolayers (i.e. semi-conducting or metallic behavior) offer a suitable platform for the simulated STM calculations. STM topographical images are an important tool for providing significant structural and electronic information. The distinct electronic band structure features (semi-conducting or metallic) are clearly visible in their STM images (Fig. 4) and may act as electronic fingerprints for comparison with experimental STM. The difference in the brightness of STM images is directly proportional to the magnitude of tunneling current passing through the sample when forward biased. The semi-conducting alloyed monolayers show faded spots showing very small tunneling current which is due to absence of channels near Fermi-level. The STM images for Pt containing alloyed monolayers have very bright spots showing larger magnitude of tunneling current which is due to presence of available channels near Fermi-level.

The tunneling characteristics are given in Fig. S4 (Supplementary information) and are in good agreement with obtained STM images of studied systems. These characteristics clearly show distinct features for semiconducting (AuCu and AuAg) and metallic (AgCu, CuPt, AgPt and AuPt) systems. The magnitude of current is low for semiconducting systems and high for metallic systems. In case of semiconducting systems, tunneling current is zero within the band gap range while the metallic systems (CuPt, AgPt and AuPt) show negative differential

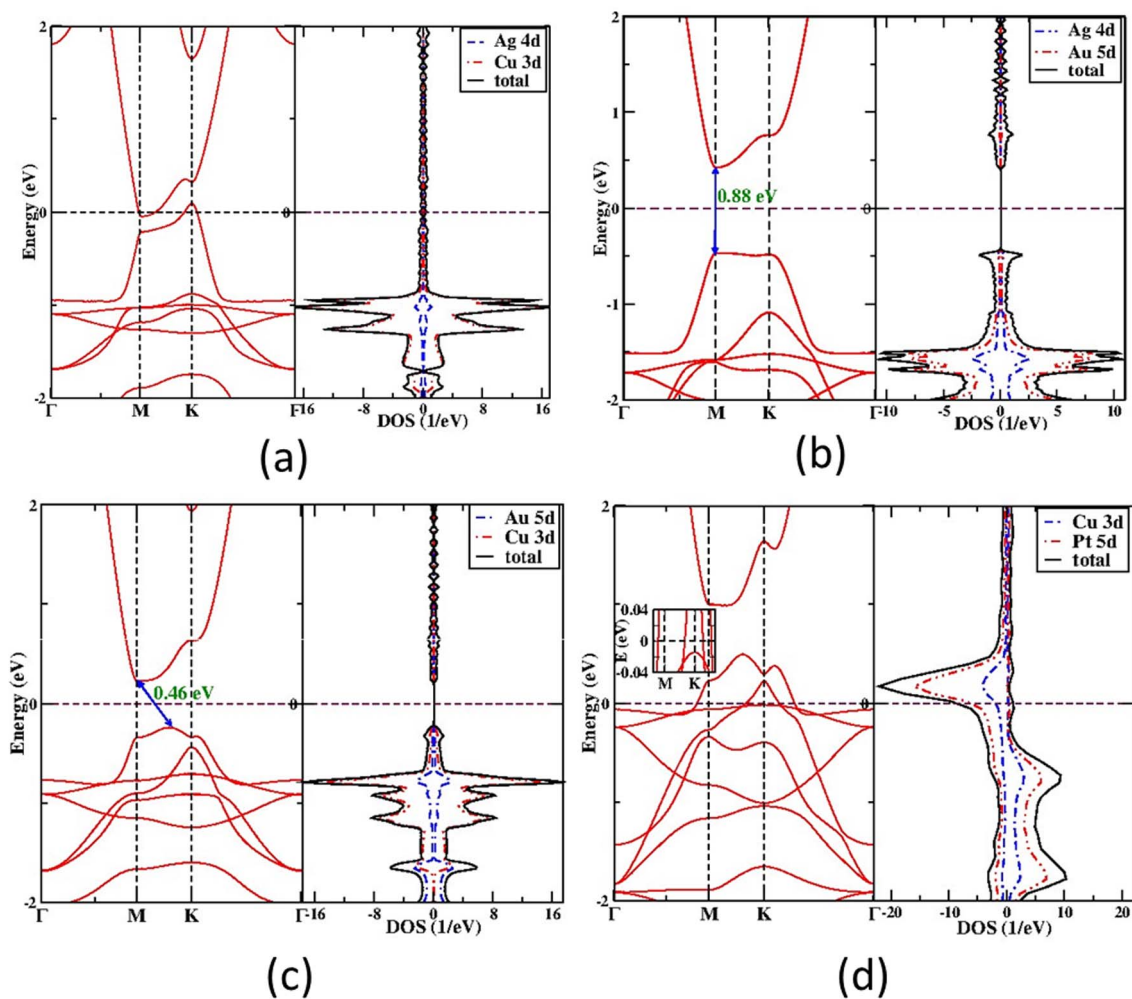


Fig. 3. Electronic band structure and density of state for the alloyed monolayers (a) AgCu, (b) AuAg and (c) AuCu and CuPt respectively. The Fermi-level is set at 0 eV. The values of band-gap for AuAg have been given in figure and the number of bands crossing the Fermi-level in CuPt has been shown in inset. The contribution from s orbitals in the density of states was very less, so they have not been shown here.

resistance (NDR). NDR is a unique property occurring rarely in some electronic circuits and devices where a decrease in current is observed with increase in voltage across the terminal, resulting in negative resistance [54,55]. NDR is of great significance in device applications such as electronic oscillators, amplifiers, switching and memory devices [56,57].

3.6. Dielectric properties

Furthermore, real and imaginary parts of dielectric function ϵ_1 and ϵ_2 , electron energy loss spectra (EELS), reflectance and absorption spectra for the systems under study have been shown in Figs. 5 and S5 of Supplementary information. The real and imaginary part of dielectric function as obtained from SIESTA and VASP calculation are plotted together in Fig. S6 and trends are found to be similar. When ϵ_1

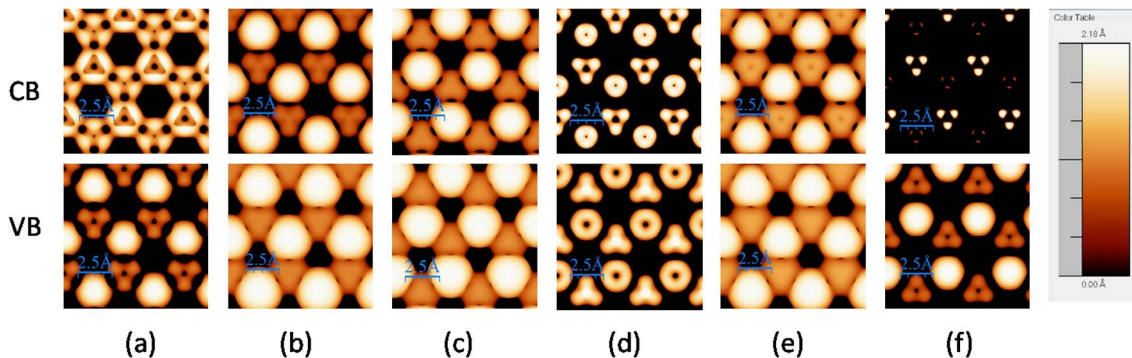


Fig. 4. Simulated STM topographical images of a $11 \text{ \AA} \times 11 \text{ \AA}$ area of (a) AgCu, (b) AgPt, (c) CuPt, (d) AuCu, (e) AuPt and (f) AuAg alloyed monolayers respectively at $\pm 0.5 \text{ V}$ bias voltage and an isosurface value of 0.00125 eV/\AA^3 where dark black areas show absence of tunneling current due to filled orbitals and bright spots indicate presence of tunneling current due to unfilled orbitals.

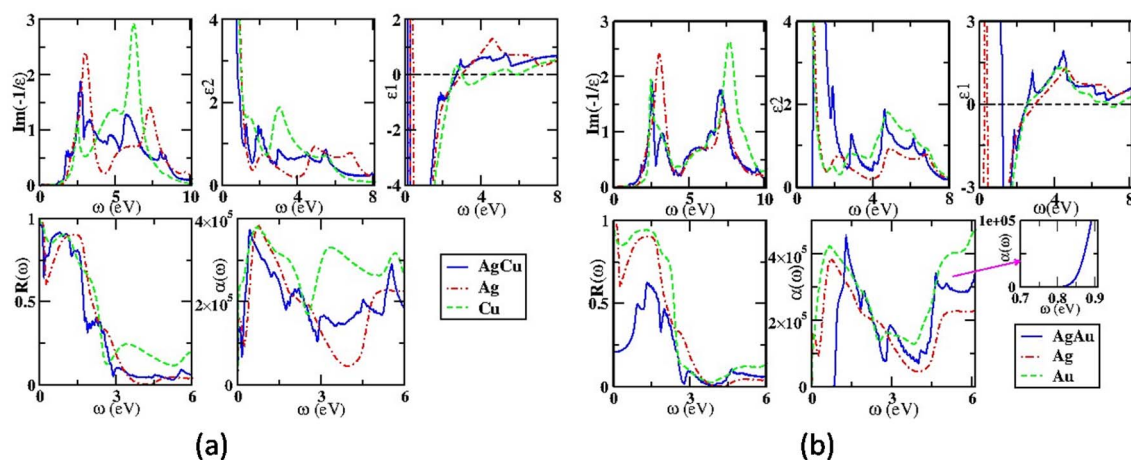


Fig. 5. The figure shows the plots of real (ϵ_1) and imaginary parts (ϵ_2) of dielectric function (ϵ), EELS spectra, absorption spectra (α) and the reflectance spectra (R) for alloyed monolayers (a) AgCu and (b) AuAg respectively and its comparison with their pristine counterparts. The rising edge of absorption peak for AuAg is shown in the inset.

approaches zero, we observe a sharp resonance peak in EELS, which gives the value of plasmon frequency (ω_p). The structural peaks associated with ϵ_2 are on account of inter-band transitions across E_f in the corresponding electronic band structure. From the Table S5, it was found that the structural peaks in ϵ_2 for alloyed monolayers systems are generally found to lie in between the values of pristine monolayers [40].

EELS show sharp resonance peaks giving the value of plasmon frequency (ω_p) for the various systems under study (Table S5). These peaks represent the collective excitation of electrons (plasmons) at these energies. From Table S5 it follows that value of plasmon frequencies of alloyed monolayers are similar to the values of pristine monolayers and lies in between the values for pristine counterparts [40]. It is found that reflectance spectra for metallic systems shows sharp dip that corresponds to the collective excitation of electrons and this sudden change reveals reflectance edge. The reflectance edge for the studied metallic alloyed monolayers (except AgCu) lies in infrared region (0 eV–1.65 eV) while for AgCu it lies in visible region (1.65 eV–3.2 eV) (Table S5). Hence, they are found to be transparent to the visible radiations.

Note that AuCu and AuAg monolayers show semiconducting nature, and hence have no reflecting properties, so we study absorption spectra in their case. The AuCu and AuAg monolayers have band gap in IR region and hence will absorb the radiations higher than their corresponding band gaps and appear blackish. The rising edge in the absorption spectra indicates that the systems absorb the radiations higher than their band gaps. The corresponding values of the absorption edge are similar to their band gaps as given in Table S5 (Supplementary information).

4. Conclusions

In summary, a comparative density functional theory (DFT) based comprehensive study has been reported to investigate structural, electronic, magnetic, mechanical, dielectric, vibrational and transport properties of ultrathin alloyed nanostructures (AuCu, AuAg, AuPt, AgCu, AgPt and CuPt) in hexagonal structure.

- The lattice constant values for alloyed monolayers lie close to their pristine counterparts.
- The value of binding energy for these alloyed structures is more than the average binding energy of their pristine counterparts showing the alloyed structure to be energetically more stable.
- Pt-containing alloyed monolayers possess higher binding energy.
- The phonon frequencies for all studied alloyed monolayers are positive for all modes at all high-symmetry points suggesting the systems to be dynamically stable.

- The Pt-containing alloyed monolayers are metallic and ferromagnetic in nature with higher tensile strengths.
- The Au containing alloyed monolayers (AuCu and AuAg) are semiconducting with a band-gap of about 0.46 eV and 0.88 eV, respectively.
- The reflectance edge and absorption edge for the alloyed monolayers lies in the infrared region.
- The distinct features in electronic band structures of alloyed monolayers are clearly visible in their tunneling characteristics and STM images.
- The considered alloyed monolayers may be useful for the applications in nanoelectronic, optoelectronic, magnetoelectronics and spintronics.

Acknowledgements

Pooja Kapoor wishes to acknowledge the financial support from University Grants Commission (UGC), New Delhi in the form of University Grants Commission Basic Sciences Research (UGC-BSR) Senior Research Fellowship (SRF). All the calculations have been carried on High Performance Computing Cluster (HPCC) in Physics Department at H.P. University, provided by Department of Science & Technology, Government of India under Funds for the Improvement of Science & Technology (FIST) programme. This research did not receive any specific grant from funding agencies in the public, commercial, or not-for-profit sectors.

Appendix A. Supplementary data

Supplementary data associated with this article can be found, in the online version, at <http://dx.doi.org/10.1016/j.mseb.2017.11.011>.

References

- [1] A.K. Geim, K.S. Novoselov, The rise of graphene, *Nat. Mater.* 6 (2007) 183–191.
- [2] F. Geng, R. Ma, A. Nakamura, K. Akatsuka, Y. Ebina, Y. Yamauchi, N. Miyamoto, Y. Tateyama, T. Sasaki, Unusually stable ~100-fold reversible and instantaneous swelling of inorganic layered materials, *Nat. Commun.* 4 (2013) 1632–1638.
- [3] C.C. Li, W.P. Cai, B.Q. Cao, F.Q. Sun, Y. Li, C.X. Kan, L.D. Zhang, Mass synthesis of large single-crystal Au nanosheets based on a polyol process, *Adv. Funct. Mater.* 16 (1) (2006) 83–90.
- [4] N. Krasteva, I. Besnard, B. Guse, R.E. Bauer, K. Mullen, A. Yasuda, T. Vossmeier, Self-assembled gold nanoparticle/dendrimer composite films for vapor sensing applications, *Nano Lett.* 2 (5) (2002) 551–555.
- [5] S.-J. Hsu, I.J.B. Lin, Synthesis of gold nanosheets through thermolysis of mixtures of long chain 1-alkylimidazole and hydrogen tetrachloroaurate(III), *J. Chin. Chem. Soc.* 56 (1) (2009) 98–106.
- [6] S. Rodriguez-Barrero, J. Fernandez-Larrinoa, I. Azkona, L.N. Lopez de Lacalle, R. Polvorosa, Enhanced performance of nanostructured coatings for drilling by

- droplet elimination, *Mater. Manuf. Process.* 31 (2016) 593–602.
- [7] X. Hong, C. Tan, J. Chen, Z. Xu, H. Zhang, Synthesis, properties and applications of one- and two-dimensional gold nanostructures, *Nano Res.* 8 (1) (2015) 40–55.
- [8] J. Kim, Y. Lee, S. Sun, Structurally ordered FePt nanoparticles and their enhanced catalysis for oxygen reduction reaction, *J. Am. Chem. Soc.* 132 (14) (2010) 4996–4997.
- [9] K. Kusada, et al., Discovery of face-centered-cubic ruthenium nanoparticles: facile size-controlled synthesis using the chemical reduction method, *J. Am. Chem. Soc.* 135 (15) (2013) 5493–5496.
- [10] F. Ernst, M.W. Finnis, D. Hofmann, T. Muschik, U. Schönberger, U. Wolf, M. Methfessel, Theoretical prediction and direct observation of the 9R structure in Ag, *Phys. Rev. Lett.* 69 (4) (1992) 620–623.
- [11] D. Novgorodova, A.I. Gorshkov, A.V. Mokhov, Native silver and its new structural modifications, *Zap. Vses. Mineral. Obshch.* 108 (1979) 552–563.
- [12] X.S. Shen, G.Z. Wang, X. Hong, X. Xie, W. Zhu, D.P. Li, Anisotropic growth of one-dimensional silver rod–needle and plate–belt heterostructures induced by twins and hcp phase, *J. Am. Chem. Soc.* 131 (31) (2009) 10812–10813.
- [13] P. Taneja, R. Banerjee, P. Ayyub, R. Chandra, G.K. Dey, Observation of a hexagonal (4H) phase in nanocrystalline silver, *Phys. Rev. B* 64 (3) (2001) 033405.
- [14] X.H. Liu, J. Luo, J. Zhu, Size effect on the crystal structure of silver nanowires, *Nano Lett.* 6 (3) (2006) 408–412.
- [15] A. Singh, A. Ghosh, Stabilizing high-energy crystal structure in silver nanowires with underpotential electrochemistry, *J. Phys. Chem. C* 112 (10) (2008) 3460–3463.
- [16] B. Wang, G.T. Fei, Y. Zhou, B. Wu, X. Zhu, L. Zhang, Controlled growth and phase transition of silver nanowires with dense lengthwise twins and stacking faults, *Cryst. Growth Des.* 28 (8) (2008) 3073–3076.
- [17] C. Liang, K. Terabe, T. Hasegawa, M. Aono, Formation of metastable silver nanowires of hexagonal structure and their structural transformation under electron beam irradiation, *Jpn. J. Appl. Phys.* 45 (7) (2006) 6046.
- [18] I. Chakraborty, D. Carvalho, S.N. Shirodkar, S. Lahiri, S. Bhattacharyya, R. Banerjee, U. Waghmare, P. Ayyub, Novel hexagonal polytypes of silver: growth, characterization and first-principles calculations, *J. Phys.: Condens. Matter* 23 (2011) 1–12 325401.
- [19] I. Chakraborty, S.N. Shirodkar, S. Gohil, U.V. Waghmare, P. Ayyub, A stable, quasi-2D modification of silver: optical, electronic, vibrational and mechanical properties, and first principles calculations, *J. Phys.: Condens. Matter* 26 (2014) 1–10 025402.
- [20] A.F. Marshall, S.V. Thombare, P.C. McIntyre, Crystallization pathway for metastable hexagonal close-packed gold in germanium nanowire catalysts, *Cryst. Growth Des.* 15 (2015) 3734–3739.
- [21] A.F. Marshall, I.A. Goldthorpe, H. Adhikari, M. Koto, Y.-C. Wang, L. Fu, E. Olsson, P.C. McIntyre, Hexagonal close-packed structure of Au nanocatalysts solidified after Ge nanowire vapor–liquid–solid growth, *Nano Lett.* 10 (9) (2010) 3302–3306.
- [22] X. Huang, S. Li, S. Wu, Y. Huang, F. Boey, C.L. Gan, H. Zhang, Graphene oxide-templated synthesis of ultrathin or tadpole-shaped Au nanowires with alternating hcp and fcc domains, *Adv. Mater.* 24 (2012) 979–983.
- [23] C.M. Payne, D.E. Tsentelovich, D.N. Benoit, W. Guo, L.J.E. Anderson, V.L. Colvin, M. Pasquali, J.H. Hafner, Synthesis and crystal structure of gold nanobelts, *Chem. Mater.* 26 (6) (2014) 1999–2004.
- [24] Z. Fan, M. Bosman, X. Huang, D. Huang, Y. Yu, K.P. Ong, Y.A. Akimov, L. Wu, B. Li, J. Wu, Y. Huang, Q. Liu, C.E. Png, C.L. Gan, P. Yang, H. Zhang, Stabilization of 4H hexagonal phase in gold nanoribbons, *Nat. Commun.* 6 (2015) 7684.
- [25] X. Huang, S. Li, Y. Huang, S. Wu, X. Zhuo, S. Li, C.L. Gan, F. Boey, C.A. Mirkin, H. Zhang, Synthesis of hexagonal close-packed gold nanostructures, *Nat. Commun.* 2 (2011) 292.
- [26] Y. Oshima, A. Onga, K. Takayanagi, Helical gold nanotube synthesized at 150 K, *Phys. Rev. Lett.* 91 (20) (2003) 205503-1–205503-4.
- [27] J. Wu, P. Li, Y.-T. Pan, S. Warren, X. Yin, H. Yang, Surface lattice-engineered bimetallic nanoparticles and their catalytic properties, *Chem. Soc. Rev.* 41 (2012) 8066–8074.
- [28] X. Teng, M. Feyngenson, Q. Wang, J. He, W. Du, A.I. Frenkel, W. Han, M. Aronson, Electronic and magnetic properties of ultrathin Au/Pt nanowires, *Nano Lett.* 9 (9) (2009) 3177–3184.
- [29] M.F. Luo, C.C. Wang, G.R. Hu, W.R. Lin, C.Y. Ho, Y.C. Lin, Y.J. Hsu, Active alloying of Au with Pt in nanoclusters supported on a thin film of Al₂O₃/NiAl(1 0 0), *J. Phys. Chem. C* 113 (2009) 21054–21062.
- [30] G. Selvarani, S.V. Selvaganesh, S. Krishnamurthy, G.V.M. Kiruthika, P. Sridhar, S. Pitchumani, A.K. Shukla, A methanol-tolerant carbon-supported Pt–Au alloy cathode catalyst for direct methanol fuel cells and its evaluation by DFT, *J. Phys. Chem. C* 113 (17) (2009) 7461–7468.
- [31] R.M. Ormerod, C.J. Baddeley, R.M. Lambert, Active alloying of Au with Pt in nanoclusters supported on a thin film of Al₂O₃/NiAl(1 0 0), *Surf. Sci.* 259 (1–2) (1991) 709–713.
- [32] J.B. Jia, L.Y. Cao, Z.H. Wang, Platinum-coated gold nanoporous film surface: electrodeposition and enhanced electrocatalytic activity for methanol oxidation, *Langmuir* 24 (11) (2008) 5932–5936.
- [33] P. Hernandez-Fernandez, S. Rojas, P. Ocon, J.L. Gomez de la Fuente, J. San Fabian, J. Sanza, M.A. Peña, F.J. García-García, P. Terreros, J.L.G. Fierro, Influence of the preparation route of bimetallic Pt–Au nanoparticle electrocatalysts for the oxygen reduction reaction, *J. Phys. Chem. C* 111 (7) (2007) 2913–2923.
- [34] X. Ye, H. Shi, X. He, Y. Yu, D. He, J. Tang, Y. Lei, K. Wang, Cu–Au alloy nanostructures coated with aptamers: a simple, stable and highly effective platform for *in vivo* cancer theranostics, *Nanoscale* 8 (2016) 2260–2267.
- [35] D.X. Li, C.F. Li, A.H. Wang, Q. He, J.B. Li, Hierarchical gold/copolymer nanostructures as hydrophobic nanotanks for drug encapsulation, *J. Mater. Chem.* 20 (2010) 7782–7787.
- [36] K.K. Kim, A. Hsu, X. Jia, S.M. Kim, Y. Shi, M. Hofmann, D. Nezhich, J.F. Rodriguez-Nieva, M. Dresselhaus, T. Palacios, J. Kong, Synthesis of monolayer hexagonal boron nitride on Cu foil using chemical vapor deposition, *Nano Lett.* 12 (2012) 161–166.
- [37] J.M. Soler, E. Artacho, J.D. Gale, A. Garcia, J. Junquera, P. Ordejon, D.S. Portal, The SIESTA method for ab initio order-N materials simulation, *J. Phys. Condens. Matter.* 14 (2002) 2745–2779.
- [38] G. Kresse, J. Hafner, Ab initio molecular dynamics for liquid metals, *Phys. Rev. B* 47 (1) (1993) 558–561.
- [39] G. Kresse, J. Furthmüller, Efficient iterative schemes for ab initio total-energy calculations using a plane-wave basis set, *Phys. Rev. B* 54 (16) (1996) 11169–11186.
- [40] P. Kapoor, J. Kumar, A. Kumar, P.K. Ahluwalia, Electronic mechanical, and dielectric properties of two-dimensional atomic layers of noble metals, *J. Electron. Mater.* 46 (1) (2017) 650–659.
- [41] A. Kumar, A. Kumar, P.K. Ahluwalia, Topology dependent electronic and dielectric properties of free standing alloyed ultrathin nanowires of noble metals, *Physica E* 62 (2014) 136–146.
- [42] N. Troullier, J.L. Martins, Efficient pseudopotentials for plane-wave calculations, *Phys. Rev. B* 43 (3) (1991) 1993–2006.
- [43] N. Troullier, J.L. Martins, Efficient pseudopotentials for plane-wave calculations. II. Operators for fast iterative diagonalization, *Phys. Rev. B* 43 (1991) 8861–8869.
- [44] G. Kresse, D. Joubert, From ultrasoft pseudopotentials to the projector augmented-wave method, *Phys. Rev. B* 59 (3) (1999) 1758–1775.
- [45] J.P. Perdew, K. Burke, M. Ernzerhof, Generalized gradient approximation made simple, *Phys. Rev. Lett.* 77 (18) (1996) 3865–3868.
- [46] J. Moreno, J.M. Soler, Optimal meshes for integrals in real- and reciprocal-space unit cells, *Phys. Rev. B* 45 (24) (1992) 13891–13898.
- [47] F. Knider, J. Hugel, A.V. Postnikov, Ab initio calculation of dc resistivity in liquid Al, Na and Pb, *J. Phys. Condens. Matter* 19 (2007) 196105.
- [48] E.G. Maksimov, I.I. Mazin, S.N. Rashkeev, Yu.A. Uspenski, First-principles calculations of the optical properties of metals, *J. Phys. F: Met. Phys.* 18 (1988) 833–849.
- [49] J. Tersoff, D.R. Hamann, Theory of the scanning tunneling microscope, *Phys. Rev. B* 31 (2) (1985) 805–813.
- [50] I. Horcas, R. Fernandez, J.M. Gomez-Rodriguez, J. Colchero, J. Gomez-Herrero, A.M. Baro, WSXM: A software for scanning probe microscopy and a tool for nanotechnology, *Rev. Sci. Instrum.* 78 (2007) 013705.
- [51] S.K. Chandel, A. Kumar, P.K. Ahluwalia, R. Sharma, A first principle study of encapsulated and functionalized silicon nanotube of chirality (6,6) with mono-atomically thin metal wires of Ag Au and Cu, *Physica E* 68 (2015) 1–7.
- [52] B.K. Agrawal, V. Singh, R. Srivastava, S. Agrawal, Ab initio study of the structural, electronic, and optical properties of ultrathin lead nanowires, *Phys. Rev. B* 74 (2006) 1–12 245405.
- [53] O. Gunnarsson, Band model for magnetism of transition metals in the spin-density-functional formalism, *J. Phys. F: Met. Phys.* 6 (4) (1976) 587–606.
- [54] Rudolf F. Graf, *Modern Dictionary of Electronics*, seventh ed., Newnes, 1999, p. 499 ISBN 0750698667.
- [55] A. Kumar, P.K. Ahluwalia, Transport properties of pristine and alloyed free standing ultrathin nanowires of noble metals, *J. Alloys Compd.* 615 (2014) 194–203.
- [56] Mohsen Shahinpoor, Hans-Jörg Schneider, *Intelligent Materials*, Royal Society of Chemistry, London, 2008, p. 209 ISBN 0854043357.
- [57] H. Beneking, ISBN 0412562200, *High Speed Semiconductor Devices: Circuit Aspects and Fundamental Behaviour*, Springer, 1994, pp. 114–117.